Doctoral Thesis

Study on Si / organic hetero-interfaces for photovoltaic applications

Sung Bum Kang

Department of Materials Science and Engineering

Graduate School of UNIST

2020

Study on Si / organic hetero-interfaces for photovoltaic applications

Sung Bum Kang

Department of Materials Science and Engineering

Graduate School of UNIST

Study on Si / organic hetero-interfaces for photovoltaic applications

A thesis/dissertation
submitted to the Graduate School of UNIST
in partial fulfillment of the
requirements for the degree of
Doctor of Philosophy

Sung Bum Kang

12. 13. 2019

Approved by

Choi

Advisor

Kyoung Jin Choi

Study on Si / organic hetero-interfaces for photovoltaic applications

Sung Bum Kang

This certifies that the thesis/dissertation of Sung Bum Kang is approved.

12. 13. 2019

signature

Choi

Advisor: Kyoung Jin Choi

signature

Sang Il Seok: Thesis Committee Member #1

signature

Hyesung Park: Thesis Committee Member #2

signature

Jeong Min Baik: Thesis Committee Member #3

signature

Shin

Jae Cheol Shin: Thesis Committee Member #4;

Abstract

The state-of-the-art Si photovoltaics have been improved over 25 % of photovoltaic conversion efficiency (PCE). It developed with n-type Si (n-Si) including PERC, HIT or IBC structures. However, the complicated and expensive processes are required for fabricating those cells. Therefore, alternatively, a hybrid combination of n-Si and PEDOT:PSS which can be processable at low-temperature in an inexpensive way has also been studied. In a recent study, the PEDOT:PSS / n-Si solar cells (PSC) exhibit ≈ high PCE of 17%. However, the high PCE is achieved by adopting oxide layers using the vacuum or high-temperature processes with costly and high thermal budgets, which is very contradictory to the motivation of PEDOT:PSS / Si solar cells. In this work, we achieved over 18% of PCE by developing highly crystalline ferroelectric P(VDF-TrFE) thin films and applying to PSC as a passivated back surface field layer, To the best of my knowledge, we demonstrated the highest efficiency among organic / Si hybrid photovoltaic devices.

The interface between PEDOT:PSS and Si is the key to determine the performances. At the interface, the high work function of PEDOT:PSS forms Schottky junction with n-Si, separating the photogenerated electrons and holes and creating a photocurrent. Previously, we demonstrated inorganic aluminium-oxide interlayers to the interface between PEDOT:PSS and Si, demonstrating a flexible, color-neutral, and high-efficiency transparent solar cells. The deposited aluminium-oxide layer provides high density of negative charges with very low density of interface defects and dangling bonds can be effectively passivated. As a result, the devices demonstrates 8 % efficiency at the visible transparency of 10 % with flexibility. This efficiency is the highest among Si based TSCs and comparable with state-of-the-art neutral-color transparent solar cells.

The polymeric material can also be used for the interlayer due to its facile processability. In particular, the organic P(VDF-TrFE) interlayer can effectively improve the photovoltaic performance of solar cells, inducing an electric field to promote the dissociation of electron-hole pairs, with the thus generated charges collected from open pores. Since such performance enhancement requires materials with a unique porous structure, I presented a novel route to highly crystalline and porous P(VDF-TrFE)) thin films based on spin coating on previous paper. Spontaneous polarization of ferroelectric P(VDF-TrFE) increases the built-in electric field of

the Schottky junction between n-Si and PEDOT:PSS and reduces the reverse leakage current of the Schottky diode

To date, the PSC exhibited more than 16% of PCE via interfacial engineering on the top side of the device, which is a hetero-interface between PEDOT: PSS and Si. However, on the bottom-side of Si, the expensive doping process or deposition of an a-Si:H at high temperature are usually accompanied, these ignore the original motivation of fabricating the Si-based photovoltaics in a simple and inexpensive way. Additionally, typical Si solar cells have been surpassed more than the PCE of 22% using the same process. Therefore, the PCE of 16% is not enough with the utilization of the vacuum and expensive processes.

We utilized the organics to both junction at the top and passivation layer at the bottom for the first time. The ferroelectric thin films provide excellent passivation effects for both p- and n-Si, enabling the large open-circuit voltage (V_{oc}) of the device. Due to its ferroelectric properties, polarization-induced-passivation is enhanced by the electric field and can be manipulated in a direction to maximize τ_{eff} at both p- and n-Si. The ambipolar P(VDF-TrFE) thin films are utilized to the rear-side of n-Si / PEDOT:PSS solar cells and such devices demonstrate record-breaking photovoltaic conversion efficiency of 18.1% with passivation and back-surface field effect. The simulation reveals that the electric field of the ferroelectric layer penetrates the rear-side and causes band bending of Si, reducing the surface recombinations of the devices. In addition, when applied to the p-Si solar cell, the cell exhibited better performance than p-Si solar cells based on Al-BSF. Moreover, the photovoltaic parameters were maintained, passing a standard 1000 hour damp heat test with > 95% of initial performance.

Contents

LIST OF FIGURES

Figure 4. Optical diffraction pattern produced by transmitted light (λ = 532 nm), demonstrating the long-range order of the wires.

Figure 5. SEM images of Si microwire arrays; pitch of (a) 4 μm pitch, (b) 5 μm, (c) 6 μm and (d) 7 μm.

Figure 6. Photovoltaic performances of TSCs based on flat SiMPFs (a) J-V characteristics and (b) EQE of the transparent solar cells with controlled pitches.

Figure 7. Box plots (minimum–maximum, 25–75%, mean: open square symbol, median: solid line) of photovoltaic parameters: (a) short circuit current, (b) open circuit voltage and (c) efficiency of flat-tip of SiMPF-based solar cells.

Figure 8. (a) The experimental and calculated reflectance spectra of planar Si (black square and 24 % of planar Si (black circle, calculated). (b) J-V characteristic of the TSC based on the 4 μm-pitched SiMW array with (black line) and without SiNx (red line).

Figure 9. Enhancing the light absorption of SiMPF by etching. (a) SEM image of flat SiMPF without etching (scale bar: 10 μm). (b) Slanted SiMPF with etching by HNAD solution having a HF: HNO_3: CH_3COOH: DMF volume ratio of 3:6:0.3:0.7 (scale bar: 5 μm). (c) Simulated reflectance of SiMPF with difference angle of etched surface. The electric field intensity in the (d) flat and (e) slanted SiMPF. (f) The total amount of electromagnetic energy in a single flat SiMPF (black solid line) and slanted SiMPF (red solid line). (g) Transmittance spectra of the slatned SiMPF of different center-to-center distance between microwires. (h) Reflectance spectra of the flat (circle dot) and slanted SiMPF (square dot) as a function of wavelength (i) The total amount of absorption in slanted SiMPF : 4 μm (green line), 5 μm (blue line), 6 μm (yellow line) and 7 μm (red line) .

Figure 10. SEM images showing (a) the dislodged Si microwire from the PDMS due to aggressive HF:HNO_3 (3:7) etching, (b) Etched Si microwire by the 3:6:1 (HF:HNO_3:CH_3COOH) solution and (c) by 3:6:1 (HF:HNO_3:DMF) solution. (d) Slanted Si microwire by the solution of having a HF: HNO_3: CH_3COOH: DMF volume ratio of 3:6:0.3:0.7.

Figure 11. Time resolved light-tracing simulation with wavelength of 550 nm at (a) flat and (b) slanted Si microwire.

Figure 12. Time resolved light-tracing simulation with wavelength of 900 nm at (a) flat and (b) slanted Si microwire.

Figure 13. The configurations to measure the haze ratio.

Figure 14. (a) The haze of the SiMPF with flat (circle dot) and slanted (square dot) tip as a function of wavelength: 4 µm (green line), 5 µm (blue line), 6 µm (yellow line) and 7 µm (red line). (a) Schematic illustration of refracted and reflected light at the slanted microwire

Figure 15. Performance of Transparent solar cells based on the slanted SiMPF (a) Optical images of freestadning slanted SiMPF. (b) The representation of the color coordinates of slanted SiMPF (★, This work), halide perovskites (◆,■, and ◈) and dyes (◀,▶▲, and ●) with AM1.5G illumination on the CIE chromaticity diagram. (c) J-V characteristics and (d) EQE of slanted SiMPF based the transparent solar cells: 4 µm (green line), 5 µm (blue line), 6 µm (yellow line) and 7 µm (red line). (e) The comparisons with previous reported neutral color transparent solar cells based on halide perovskite, dye, a- Si, and organics.

Figure 16. (a) Optical images of perovskite filters: i) $MAPb(I_{0.41}Br_{0.59})_3$, ii) $MAPb(I_{0.28}Br_{0.72})_3$ and iii) $MAPb(I_{0.05}Br_{0.95})_3$ (b) absorbance and (c) transmittance spectra of various perovskite filters

Figure 17. Box plots (minimum–maximum, 25–75%, mean: open square symbol, median: solid line) of photovoltaic parameters: (a) short circuit current, (b) open circuit voltage and (c) efficiency of slanted-tip of SiMPF-based solar cells.

Figure 18. The averaged EQE enhancement of slanted SiMPF based devices as function of wavelength.

Figure 19. **Flexibility of transparent solar cell and Large scalability of free-standing SiMPF** (a) Light J-V curves and (b) normalized photovoltaic parameters of transparent solar cells under the bending state with the different bending radius. (c) Normalized efficiency of the transparent solar cells after cyclic bending test. Photographic images of (d) Si Mw arrays on 2-inch wafer, and (e) Free-standing SiMPF peeled from the (d).

Figure 20 Stretchablity of free-standing SiMPF. (a) Optical diffraction pattern of the SiMPF at ε = 0 % and 50 %. (b) The changes in resistances at each strain values as the 5 % strain interval during stretching (0 → 50 %) and releasing state (50 → 0 %) at 1 cycle and 15 cycles. (c) Changes in conductivity when the applied strain is 0 % and 50 % under repetition of stretching and releasing cycles.

Figure 21. The transmittance spectra of the sample with 5 um pitch without (red line) and with strain (black line).

Figure 32. 10 × 10 μm^2 three-dimensional topological AFM image of a porous P(VDF-TrFE) thin film.

Figure 33. (a) Schematic illustration of a PEDOT:PSS/P(VDF-TrFE)/Si solar cell and photovoltaic performance variation upon insertion of a porous P(VDF-TrFE) thin film between PEDOT:PSS and Si. (b) J–V curves for 1-sun-illuminated devices poled under different conditions. (c) Open circuit voltage as a function of poling voltage. (d) Dark J–V curves of devices subjected to positive poling (red line), no poling (black line), and negative poling (blue line). Band diagram and working principles of the porous ferroelectric P(VDF-TrFE) interlayer for hybrid solar cells under positive (e) and (f) negative poling conditions.

Figure 34. J–V curves of 1-sun-illuminated devices containing P(VDF-TrFE) films with porosities of (a) 0%, (b) 5%, (c) 40%, (d) 65%, and (e) 100% before (black lines) and after positive poling (red lines, +20V). (f) Post-poling efficiency enhancement as a function of film porosity.

Figure 35. Reversible behaviors of the poling effect (a) J-V characteristics of PEDOT:PSS/P(VDF-TrFE)/n-Si hybrid solar cell. (b) The efficiency of PEDOT:PSS/P(VDF-TrFE)/n-Si hybrid solar cell are switched from positive poling state to negative poling state repeatedly.

Figure 36. (a) The open circuit voltage of PEDOT:PSS/n-Si solar cell without ferroelectric interlayer (green line), non-poled (black line), and positively poled (blue line) PEDOT:PSS/P(VDF-TrFE)/n-Si solar cell as a function of elapsed time after device fabrication (b) The changes of the open circuit voltage between positively poled and non poled devices as a function of elapsed time after device fabrication.

Figure 37. FDTD electrostatic potential simulation for (a) PEDOT:PSS/n-type Si solar cell and (b) PEDOT:PSS/n-type Si solar cell with a ferroelectric layer; (c) line scans along paths A, B, and C.

Figure 38. SEM images of (a) smooth and (b) porous PVDF-TrFE thin films on textured Si substrates thermally annealed at 135 °C for 4 hours. 2D GIXD patterns of (c) smooth and (d) porous PVDF-TrFE thin films. The crystalline nature of the PVDF-TrFE films exhibited 2D diffraction patterns where a reflection intensified at the meridian regions on the patterns corresponding to either (110) or (200).

Figure 39. SEM images of diffrent porous p(VDF-TrFE) thin films prepared by solution of P(VDF-TrFE) in (a,b) DMF and (c,d) DMSO with addition of deionized water.

Figure 40. SEM images of diffrent porous P(VDF-TrFE) thin films prepared on the various substrate.

Figure 41. Equatorial azimuthal intensity profiles of (a) pristine and (b) porous and crystalline P(VDF-TrFE) thin films.

Figure 42. (a) SEM image of the Si nano structure arrays in black Si. (b) Optical images of black and planar Si. (c) Total reflectance spectra of planar Si (gray sold line) and black Si (blue solid line) (d) Spectral distribution of absorbed photons of planar Si (gray), black Si (blue), and AM 1.5G spectrum (red).

Figure 43. (a) Changes of Si 2p XPS spectra of crystalline P(VDF-TrFE)/Si during etching. The Si 2p and C 1s XPS spectra at the interface of (b) continuous P(VDF-TrFE)/Si and (c) Crystalline P(VDF-TrFE) /Si. Schematic representation of the interfaces of (d) continuous P(VDF-TrFE)/Si and (e) crystalline P(VDF-TrFE)/Si. the violet arrows indicate the magnitude and direction of polarization (Each colored ball represented each atom; black: Silicon, red: Oxygen, Yellow: carbon, green: fluorine and blue: Hydrogen).

Figure 44. (a) Topography and (b) surface potential distribution of the porous P(VDF-TrFE) coated Si substrate. (c) line scan of (b). The effective lifetime as function of injection level were measured on (d) p-type (Doping concentration of 7.8×10^{14} cm^{-3}) and (e) n-type (Doping concentration of 8.5×10^{15} cm^{-3}) c-Si wafers passivated by the P(VDF-TrFE). SiN_x and SiO_2 (f) The ambipolar property of P(VDF-TrFE) thin films; Dependence of the effective lifetime of n- and p-type Si wafer (@ injection level of 1×10^{15} cm^{-3}) on corona voltages

Figure 45. (a) SEM image of the Si nano structure arrays in black Si. (b) Optical images of black and planar Si. (c) Total reflectance spectra of planar Si (gray sold line) and black Si (blue solid line) (d) Spectral distribution of absorbed photons of planar Si (gray), black Si (blue), and AM 1.5G spectrum (red).

Figure 46. (a) PEDOT:PSS coated on black Si without Al_2O_3, The PEDOT:PSS is partially coated on the Si. (b) The contact angle measurement of the black Si and (b) Al_2O_3 coated on black Si by using IPA-diluted PEDOT:PSS, exhibiting the angle of 54.773^o and 13.776^o,

respectively. SEM micrograph of conformally coated PEDOT:PSS on Al_2O_3/black Si: (c) cross section (d) high and (e) low magnitude.

Figure 47. (a) High resolution TEM image and (b) electron image. (c) EDS layered image and element mapping (d-f) images of Al_2O_3 coated Si nanowire.

Figure 48. J-V characteristics of the PEDOT:PSS / black Si devices (a) under dark and (b) 1 sun illumination with and without a Al_2O_3 interfacial layer.

Figure 49. (a) Schematic illustration of a PSC with P(VDF-TrFE). (b) Light J−V curves of devices without a porous P(VDF-TrFE) layer (green), with porous P(VDF-TrFE) layer (red) and after [+] poling (green). (c) Measured EQE spectra of the solar cell with and without porous P(VDF-TrFE). (d) FDTD electric potential simulation for device (not to scale) and (e) line scans along red arrow. (f) Schematic of the energy band diagram of a contact with P(VDF-TrFE) thin film.

Figure 50. Statistical Distribution of the Photovoltaic Parameters for PSC without P(VDF-TrFE), with P(VDF-TrFE), and with P(VDF-TrFE) after poling. (a–d) Dependence of (a) Voc, (b) Jsc, (C) FF, and (D) efficiency

Figure 51. (a) Schematic illustration of HSC with P(VDF-TrFE). (b) Light J−V curves of devices without a porous P(VDF-TrFE) layer (green), with porous P(VDF-TrFE) layer (red) and after [-] poling (green). (c) Thermal and humidly stability of the HSP solar cells. The relative change in efficiencies (with P(VDF-TrFE), with P(VDF-TrFE) after poling) are plotted as function of damp heat test time.

Figure 52. Statistical Distribution of the Photovoltaic Parameters for HSC without P(VDF-TrFE), with P(VDF-TrFE), and with P(VDF-TrFE) after poling. (a–d) Dependence of (a) Voc, (b) Jsc, (C) FF, and (D) efficiency

Figure 53. (a) the schematic of HSC with Al _BSF. (b) Light J-V characteristics of the device.

Table 1. Average photovoltaic performance of flat SiMPF based transparent solar cells[a] and champion device with controlled spacing between microwires. [a]Average performance for 8 devices.

Table 2. Optical properties (reflectance, transmittance) of flat SiMPF.

CHAPTER 1. Interfaces

1.1 Definition of interface

First, we need to know the concept of the surface before defining the interface. The surface is very important. Whatever we see, we can only see the surface of the material, not the inside. Whatever we touch, we can only touch the surface, not the inside. The reaction between materials reacts between the surfaces and surfaces, not inside. Generally, the surface of substances has very different physical and chemical properties from their inside. What we call surfaces are parts that remain solid or liquid, and are exposed, forming boundaries with other phases. Theoretically, the surface is the outermost layer of an atom in the system. It is only correct if the substance is a pure metal of a single element. However, most of the substances are compounds. Therefore, if the basic constituent of a substance is a molecular compound, the molecular layer should be called the surface, and it is difficult to say that only one atom is the surface of the substance. For example, surface treatment on substances can affect not only the outermost atoms but also several to tens of atomic layers. Similarly, in the formation of the native oxidation in Si, oxygen in the air react with the Si and form oxide films. Oxygen penetrates inside and forms oxides with a few nm-thickness. This also makes it hard to say that only one outermost layer is a surface. So the surface is theoretically the outermost layer atom but it is also the minimum thickness (solid) or portions (liquid, gas). In this point of view, we can define what the interface is. When the two different surfaces which involving the interactions, we call those points as “interface”.

1.2 Types of interfaces

There are five types of interfaces: liquid / gas(vapor), liquid/liquid, liquid/solid, gas / solid, and solid/solid. They plays an essential role in wide fields and help to understand the physical phenomena and structural background of the interface including catalysis, crystal growth, electrochemistry, colloidal system, and various applications [1-6]. The liquid / gas interface provides a heterogeneous environmental conditions. Therefore, molecules on the surface and at the bulk behaves in a different way. Due to these broken symmetry, the molecules at the interface show different spatial correlations with the molecules in the bulk liquid. The molecular structure at the interface thus has a significant impact on how solute molecules are adsorbed or evaporated in the liquid [7]. Moreover, liquid and vapor interface can be the platform for chemical reactions. when the reaction occurs at this interface, the solution phase or gas phase or both are utilized as the path of the reactants, resulting in the formation of the product at the interface and allowing the volatile compounds to escape so that they are not trapped inside. Liquid/liquid interface is particularly essential in synthesis of various materials. This method generally proceeds in a single step to form nanocrystalline membranes at the interface of two immiscible liquids, one liquid is water and the other is an organic liquid. The interface is heterogeneous, usually several nanometers thick, and provides an excellent route for self-assembly and chemical manipulation of nanocrystals [1, 5, 8, 9]. In this method, the metal precursor is taken from the organic layer and forms an ultrathin nanofilm at the interface by a self-assembly process by reaction with a suitable reagent containing an aqueous layer [10].

The interfaces at liquids and solids are simply defined as the word of wetting [11]. Liquid can spread on solid surfaces, penetrate into porous materials, or displaced into another. This phenomenon can help to characterize the surface and determine the interaction between the solid and the liquid. One way to quantify the surface wetting properties of liquids is to measure the contact angle of liquid droplets placed on the surface of an object [10, 12, 13]. The contact angle is the angle formed by the solid / liquid interface, measured from the liquid side. When the contact angle is less than 90 °, the liquid wets the surface. For the penetration material to be effective, the contact angle must be as small as possible. In fact, the contact angle for most liquid penetrants is very close to 0 °. This is closely related to the surface energy which is across an interface or surface tension, estimated by the following expression [13].

$$\gamma_L\cdot(1 + \cos\theta) = 2(\gamma^p{}_s\cdot\gamma^p{}_L)^{1/2} + 2(\gamma^d{}_S\cdot\gamma^d{}_L)^{1/2} \qquad (1)$$

where the total surface energy of the film, γ_s (= $\gamma_s{}^p$+$\gamma_s{}^d$), is the sum of the polar ($\gamma_s{}^p$) and dispersion ($\gamma_s{}^d$) components, and the surface tension of the liquids, γ_L (= $\gamma_L{}^p$+$\gamma_L{}^d$), is the sum of the polar ($\gamma_L{}^p$) and dispersion ($\gamma_l{}^d$) components. These two values can be estimated from the contact angles of different test liquids by solving two simultaneous equations. The representative polar solvent H_2O and nonpolar solvent CH_2I_2 are used to measure the contact angles. the Intermolecular bonds or cohesion between liquid molecules cause surface tension.

When a liquid meets another substance, there is usually an attraction between the two substances. The adhesion between the liquid and the second material will compete with the cohesion of the liquid. Liquids with weak cohesion and a strong incentive to other materials or the desire to create an adhesive bond tend to spread over the material. Liquids with high adhesion and liquids with low adhesion tend to bead up or form water droplets when in contact with other substances [3, 14-16].

More importantly, solid / solid interfaces are key to determine the properties of materials. For examples, The solid-solid interface resulting from the difference in orientation or the transformation between two crystals of the same phase across the interface is called the homo phase interface [17, 18]. Examples of solid / solid interfaces related with those things include grain boundaries, tween boundaries, and stack faults [19-21]. On the other hand, the interfaces involving the semiconductor is very fascinating topics, including chemical, physical and electronic aspects. In the recent past, the field has experienced dramatic developments both in experimental and theoretical terms. New experimental tools and approaches well as advanced theoretical way, have led to a deeper understanding of semiconductor interface characteristics. My dissertation focuses specifically on these interfaces. It will attempt to systematically introduce the interface of Si solar cells, while reviewing my works on Si / organic hetero-interfaces for photovoltaic applications.

1.3 Solid / Solid interfaces

The interfaces between semiconductor and metal is one of the representative solid / solid interfaces, widely utilized for the electronic devices, manipulating the transport of electron and holes [22-24]. when the metal and n-type semiconductor are joined when the work function of the metal is larger than the work function of the n-type semiconductor, the biggest change expected when joining metal and semiconductor is the change of fermi level in equilibrium. Metals and semiconductors have different Fermi levels, and it does not matter if they are different systems, but if they are joined together to form a single system, the Fermi levels of the two materials must be merged into one. As you can see from the figure above, the Fermi level of the metal is lower than the Fermi level of the semiconductor, so the electrons of the semiconductor will diffuse into the metal with lower energy due to the difference in Fermi level. If the electrons of the semiconductor are diffused into the metal, the fixed donor cations of the n-type semiconductor will be revealed, and the electrons and cations transferred to the metal form a depletion region. In the end, this phenomenon will continue until the Fermi levels match, and this phenomenon will continue, an electric field will be formed in the depletion region that prevents electrons from diffusing into the metal. The barrier that prevents the diffusion of n-type semiconductors is as large as the difference between the work function of the metal and the semiconductor. The barrier formed to prevent the transition from metal to the semiconductor is called the Schottky barrier [25], and the difference between the work function of the metal and the electron affinity of the semiconductor, defined as the p-type semiconductor can be thought of as the opposite of the n-type semiconductor [26]. When the depletion region is formed, the biggest feature is that it behaves like a diode. That is, the current flows well to only one side. The reason for this is the Schottky barrier that prevents the movement of electrons from the metal to the semiconductor. Therefore, the junction between the metal and the semiconductor is also called Schottky diode. However, the most important situation so far is that the work function of metal is larger than that of n-type semiconductor. Then, the depletion region is formed by this condition and if forward-bias is applied, current flows from the semiconductor to the metal, and if reverse-bias is applied. Therefore, the work function of the metal is larger than the work function of the n-type semiconductor, so that a depletion region is formed, which acts like a diode, called rectifying contacts. Conversely, when the work function of the n-type semiconductor is larger than the work function of the metal, it has an ohmic I-V characteristic that flows current in both directions. the work function of the n-type semiconductor, so that a depletion region is formed, which acts like a diode, called rectifying contacts. Conversely, when the work function of the n-type semiconductor is larger than the work function of the metal, it has an ohmic I-V characteristic that flows current in both directions. the work function of the n-type semiconductor, so that a depletion region is formed, which acts like a diode, called rectifying contacts. Conversely, when the work function of the n-type semiconductor is larger than the work function of the metal, it has an ohmic I-V characteristic that flows current in both directions. the work function of the n-type semiconductor, so that a depletion region is formed, which acts like a diode, called rectifying contacts. Conversely, when the work function of the n-type semiconductor is larger than the work function of the metal, it has an ohmic I-V characteristic that flows current in both directions.

On the other hand, the interfaces between two semiconductors which have mobility, exciton binding energy and band gap is also one of the examples of solid / solid interfaces, utilized as electronic, photonic and optoelectronic devices. When two different materials met each other, band lineups occur at the interface in suitable combinations. Therefore, the carriers or electrons are transported or trapped. Moreover. its characteristic is a sharp change in the energy gap at the interface, resulting in discontinuities or offsets in conduction and valence band edges. The magnitude of these offsets is assumed to be a characteristic of the semiconductor pair involved. It is also independent of the doping level and hence Fermi level considerations, but may depend on the crystallographic orientation and other factors affecting the precise arrangement of atoms near the interface.

If two solids are in contact and no mixing occurs, the electronic structure will be locally disturbed at the interface because the bonding structure is different from the bulk of the two materials. The lineup of the electronic band structure at the semiconductor interface can be described as if it looks different. Specifically, they formed “diode”. It will be discussed on the Chapter 2 more detailed.

1.4 Solid / Solid interfaces for electronic applications

Using a rugged interface, these electronics have established a wide range of applications due to their reliability, miniaturization and low cost. These are the individual components used in power devices, small optical sensors, light emitters, transistors, and solar cells. It has a wide range of current and voltage handling capabilities. On the other hand, they can harvest energies from the solar light. More importantly, semiconductor devices are integrated into complex but easily built microelectronic circuits. They anticipate the future, a key element of most electronic systems, including communication with data processing. Semiconductor devices are just electronic components that take advantage of the electronic properties of organic semiconductors, as well as semiconductor materials such as silicon, germanium, and gallium arsenide. They use electron conduction in the solid-state as opposed to thermal ion release in a high vacuum. Semiconductor devices are fabricated for both individual devices and integrated circuits made up of billions to billions of devices interconnected and manufactured on a single semiconductor substrate or wafer. From now on, **I will introduce one of the interface-based electronic devices, which is the Si Solar cell.**

1.5 Reference

1. Dang, L. X., et al. Molecular dynamics study of water clusters, liquid, and liquid-vapor interface of water with many-body potentials. *Journal of Chemical Physics* **106**, 8149-8159 (1997).
2. Shan, X. W., et al. SIMULATION OF NONIDEAL GASES AND LIQUID-GAS PHASE-TRANSITIONS BY THE LATTICE BOLTZMANN-EQUATION. *Physical Review E* **49**, 2941-2948 (1994).
3. Song, H., et al. Reactions in droplets in microflulidic channels. *Angewandte Chemie-International Edition* **45**, 7336-7356 (2006).
4. Woll, C. The chemistry and physics of zinc oxide surfaces. *Progress in Surface Science* **82**, 55-120 (2007).
5. Zhang, Q. F., et al. Nanomaterials for energy conversion and storage. *Chemical Society Reviews* **42**, 3127-3171 (2013).
6. Zhao, B., et al. Surface-directed liquid flow inside microchannels. *Science* **291**, 1023-1026 (2001).
7. Hoffman, R. L. STUDY OF ADVANCING INTERFACE .1. INTERFACE SHAPE IN LIQUID-GAS SYSTEMS. *Journal of Colloid and Interface Science* **50**, 228-241 (1975).
8. Haruta, M., et al. Advances in the catalysis of Au nanoparticles. *Applied Catalysis a-General* **222**, 427-437 (2001).
9. Yin, Y., et al. Colloidal nanocrystal synthesis and the organic-inorganic interface. *Nature* **437**, 664-670 (2005).
10. Aveyard, R., et al. Emulsions stabilised solely by colloidal particles. *Advances in Colloid and Interface Science* **100**, 503-546 (2003).
11. Bonn, D., et al. Wetting and spreading. *Reviews of Modern Physics* **81**, 739-805 (2009).
12. Lu, Y. F., et al. Continuous formation of supported cubic and hexagonal mesoporous films by sol gel dip-coating. *Nature* **389**, 364-368 (1997).
13. Voinova, M. V., et al. Viscoelastic acoustic response of layered polymer films at fluid-solid interfaces: Continuum mechanics approach. *Physica Scripta* **59**, 391-396 (1999).
14. Oron, A., et al. Long-scale evolution of thin liquid films. *Reviews of Modern Physics* **69**, 931-980 (1997).
15. Wong, T. S., et al. Bioinspired self-repairing slippery surfaces with pressure-stable omniphobicity. *Nature* **477**, 443-447 (2011).

16. Xia, Y. N., et al. Soft lithography. *Angewandte Chemie-International Edition* **37**, 550-575 (1998).

17. Huo, Q. S., et al. GENERALIZED SYNTHESIS OF PERIODIC SURFACTANT INORGANIC COMPOSITE-MATERIALS. *Nature* **368**, 317-321 (1994).

18. Penn, R. L., et al. Imperfect oriented attachment: Dislocation generation in defect-free nanocrystals. *Science* **281**, 969-971 (1998).

19. Chen, L. Q. Phase-field models for microstructure evolution. *Annual Review of Materials Research* **32**, 113-140 (2002).

20. Erlebacher, J., et al. Evolution of nanoporosity in dealloying. *Nature* **410**, 450-453 (2001).

21. Xu, X. P., et al. NUMERICAL SIMULATIONS OF FAST CRACK-GROWTH IN BRITTLE SOLIDS. *Journal of the Mechanics and Physics of Solids* **42**, 1397-& (1994).

22. Gambino, J. P., et al. Silicides and ohmic contacts. *Materials Chemistry and Physics* **52**, 99-146 (1998).

23. Schmitsdorf, R. F., et al. Explanation of the linear correlation between barrier heights and ideality factors of real metal-semiconductor contacts by laterally nonuniform Schottky barriers. *Journal of Vacuum Science & Technology B* **15**, 1221-1226 (1997).

24. Tung, R. T. ELECTRON-TRANSPORT AT METAL-SEMICONDUCTOR INTERFACES - GENERAL-THEORY. *Physical Review B* **45**, 13509-13523 (1992).

25. Monch, W. Barrier heights of real Schottky contacts explained by metal-induced gap states and lateral inhomogeneities. *Journal of Vacuum Science & Technology B* **17**, 1867-1876 (1999).

26. Peacock, P. W., et al. Band offsets and Schottky barrier heights of high dielectric constant oxides. *Journal of Applied Physics* **92**, 4712-4721 (2002).

2. Interfaces in Si solar cells

2.1. Si / Si interfaces

In the Si solar cells, the Si / Si interfaces are used for the junctions which can separate electron and holes. Generally, n -type Si / p-Si interface is very representative. Then, we should understand what the doping is. Doping with other atoms can change the balance of electrons and holes in the silicon crystal lattice [1, 2]. If one more atom than silicon at the valance band, it can make an n-type semiconductor material with electrons added to the conduction band, where the atoms are group V elements. The five valence electrons of these elements can form covalent bonds with the four electrons of silicon, and since only four electrons are needed for each silicon atom, the two covalent bonds The remaining extra electrons take part in the conduction. Thus more electrons are added to the conduction band and thus the number of electrons present increases. If the Si is doped with one less atom of Group III element, it can make a p-type material. These elements combine three silicon atoms with silicon atoms, and holes are formed due to the lack of enough electrons to bond with the silicon atoms. In p-type materials, the number of electrons trapped in the bond is greater, which can effectively increase the number of holes. In doped materials there is always more of one type of carrier than the other, with higher concentrations of carriers called majority carriers and lower concentrations of carriers called minority carriers.

The number of carriers in the conduction band and valence band without external bias is called the equilibrium carrier concentration. For majority carriers, the equilibrium carrier concentration is the intrinsic carrier concentration plus the number of free carriers added by semiconductor doping. Under most conditions, the number of majority carriers is approximately equal to the doping because the semiconductor doping is orders of magnitude greater than the intrinsic carrier concentration. At equilibrium, the product of the majority carrier and the minority carrier is a constant, which is expressed mathematically as the mass action as followed [3].

$$n_0 p_0 = n_i{}^2 \quad (1)$$

Where n_i is the intrinsic carrier concentration and n_0 and p_0 are the equilibrium carrier concentrations of electrons and holes, respectively. Using the mass action law above, the majority and minority carrier concentrations are given by [4]

$$\text{For p-type : } p_0 = N_A n_0 = \frac{{n_i}^2}{N_A} \quad (2)$$

$$\text{For n-type : } n_0 = N_D p_0 = \frac{{n_i}^2}{N_D} \quad (3)$$

The above equations show that as the level of doping increases, the number of minority carriers decreases. For example in n-type materials some of the extra electrons added as doping will occupy empty space in the valence band, thus lowering the number of holes.

On the other hand, Photons incident on the surface of the semiconductor will either be reflected from the surface or absorbed into the material, or otherwise penetrate the material. In the case of photovoltaic devices, photons that are not absorbed do not generate power, so the reflected and transmitted portions become a loss mechanism. If the photons are absorbed, the photons raise the electrons from the valence band to the conduction band. The key factor in determining whether a photon is absorbed or transmitted is the energy of the photon. Photons falling on the semiconductor material can be divided into three groups compared to the bandgap of the semiconductor [5].

$E_{ph} < E_G$: Bandgap energy less than E_G, Photons of E_{ph} are very weak in interaction with the semiconductor and pass through the semiconductor as if it were transparent.

$E_{ph} = E_G$: Absorbed very efficiently with energy enough to produce one electron-hole pair.

$E_{ph} > E_G$: Photons of energy larger than the bandgap are absorbed very strongly.

When photons are absorbed, both majority and minority carriers are produced. In many solar cells, the number of carriers generated by light is several orders of magnitude smaller than the number of carriers already present in the solar cell by doping. Therefore, the number of majority carriers does not change greatly in the semiconductor under the light. However, the number of minority carriers varies greatly. The number of minority carriers generated by light greatly exceeds the number of minority carriers present in the solar cell in the dark state, and as a result, the number of minority carriers in the solar cell being illuminated is approximately generated by light. It will be similar to the number of carriers.

When two different types of semiconductor form junction, we can call it as diode which can manipulate movement of carriers by changing electric field. Forward bias is the voltage applied across the device to reduce the electric field at the junction. When a positive voltage is applied to the p-type material and a negative voltage to the n-type material, the electric field is applied to the entire device as opposed to the direction of the electric field in the depletion region. Since the specific resistance of the depletion region is much higher than the rest of the device (the number of carriers in the depletion region is limited), almost all applied electric fields drop across the depletion region. The net electric field is the difference between the existing electric field in the depletion region and the applied electric field (in a real device, the internal electric field is always larger than the applied electric field), thereby reducing the total electric field in the depletion region. As the electric field decreases, the equilibrium at the junction is disturbed, which lowers the barrier that prevents carriers from diffusing from one side of the junction to the other, increasing the diffusion current. While the diffusion current increases, the drift current remains essentially unchanged because it depends on the number of carriers created within the diffusion length range of the depletion region or within the depletion region. Since the depletion region is only slightly reduced in width, the number of minority carriers passing across the junction is essentially unchanged [3].

Increasing diffusion from one side of the junction to the other results in minority carrier injection at the edge of the depletion region. These carriers move away from the junction due to diffusion and finally recombine with one majority carrier. The majority carriers are supplied from external circuitry, so net current flows under forward bias. In the absence of recombination, minority carrier concentrations newly reach a higher concentration equilibrium, and diffusion of carriers from one side of the junction to the other stops, as if two gases were introduced. Initially, gas molecules exhibit net motion from the higher carrier concentration to the lower region, but have reached a homogeneous concentration [6].

In semiconductors, however, the injected minority carriers recombine, so that more carriers can diffuse across the junction. As a result, the diffusion current flowing in the forward direction is one recombination current. The faster the rate of recombination, the greater the current flowing across the junction. Dark saturation current (I_0) is an extremely important variable that determines the difference between diodes. I_0 is a measure of recombination in the device. Diodes with larger recombination have higher I_0 values. In reverse bias, a voltage is applied across the device in the direction of increasing electric field at the junction. Higher electric fields in the depletion region reduce the probability that carriers will diffuse from one side of the junction to the other, thus reducing the diffusion current. As with forward bias, the drift current is limited by the number of minority carriers on either side of the p-n junction and remains relatively unchanged as the electric field increases. The drift current increases slightly due to the slight increase in the width of the depletion region, but this is essentially a secondary effect in solar cells. In most thin film solar cells whose thickness of the depletion region is about 1/2 of the thickness of the solar cell, the change of the depletion region width according to the voltage greatly affects the operation of the solar cell [1].

Therefore, diode equation as described in equation (5) is very important in determining the quality of junction. I_0 is directly related to recombination and inversely related to the quality of the material. Non-ideal diodes contain an "n" term in the denominator of the exponent. n is an ideality factor in the range from 1 to 2, increasing as the current decreases.

$$\mathrm{I} = I_0\left(e^{\frac{qV}{kT}} - 1\right) \quad (4)$$

Where I = net current flowing through the diode, I_0 = dark saturation current, V = voltage applied across the diode, q = absolute value of charge, k = Boltzmann constant and T = absolute temperature (K).

There are electrons in the conduction band, they are in a meta-stable state and will eventually fall back to the lower energy level in the valence band. As the electrons fall back into the valence band, one hole is removed as a result. This process is called recombination. Within the bulk of a single crystal, there are three basic types of recombination: Radiative recombination, Shockley-Read-Hall recombination and Auger recombination. Radiative recombination is the dominant recombination mechanism in direct bandgap semiconductors. Si solar cells are usually made from direct transition semiconductors such as GaAs, where radiative recombination is dominant. Most of the solar cells, however, which is an indirect transition semiconductor and has very low radiative recombination, which is usually ignored. Recombination through a defect called Shockley-Read-Hall (SRH) recombination does not occur in a completely pure defect-free material. SRH recombination is a two-step process. One electron (or hole) is trapped in an energy state in the forbidden region introduced due to a defect in the crystal lattice. These defects were inadvertently created or added intentionally, such as by the doping. Recombination occurs when one hole (or one electron) moves to the same energy state before the electron is thermally re-emitted into the conduction zone. The speed at which one carrier moves to an energy level in the forbidden region depends on the distance from each band edge to the corresponding energy level. Therefore, if energy is introduced near the end of the band, the probability of recombination is low because electrons are more likely to re-radiate to the end of the conduction band rather than to recombine with holes traveling from the valence band to the same energy state. For this reason, energy levels in the middle of the bandgap are very effective for recombination. Three carriers participate in one Auger recombination. One electron and one hole recombine, but instead of radiating energy as heat or photons, energy is given to electrons in the conduction band, the third carrier. The electrons then later thermalize to the ends of the conduction band. Auger recombination is very important when the carrier concentration is very high, either by high concentration doping or by high concentration injection under condensing. Auger recombination in silicon-based solar cells limits the lifetime and efficiency. The higher the doping, the shorter the Auger recombination life. If the number of minority carriers increases above the equilibrium value by some instantaneous excitation from the outside, the excess minority carriers will be attenuated to the equilibrium carrier concentration by the recombination process. An important variable in solar cells is the recombination rate. The process known as 'recombination rate' depends on the number of excess minority carriers. For example, if there are no excess minority carriers, the recombination rate is zero. The minority carrier lifetime of the material, denoted τ_n or τ_p, is the average time spent in the excited state after electron-hole generation before the carrier recombines. The lifetime of a minority carrier is a measure of how long one carrier lasts before recombination.

2.2. Si / Metal hetero-interfaces

The metal in Si solar cells play a role for collecting the carriers from the junction[7-9]. To reduce contact resistance between the hetero-interfaces between Si and metal. Both shunt and series resistance losses reduce the charge rate and efficiency of the solar cell. Critically low parallel resistance is not a design variable but a process defect. The series resistance, which depends on the design of the top contact electrode and the emitter resistance, must be carefully designed for each solar cell type and structure to optimize the efficiency of the solar cell. The top metal contact electrode is needed to collect the current generated by the solar cell. Busbars are directly connected to the external leads, and the finger is a thin metal region that collects current, where the collected current is delivered to the busbar. The key to top contact design is how to make a trade-off between increased resistive losses due to wide spacing grids and increased reflections by increasing the proportion of metal electrodes on the top surface.

Based on the surface resistivity, the output loss due to the emitter resistance can be calculated as a function of finger spacing at the top contact. However, the distance that the current flows through the emitter is not constant. Since the current is collected from the base close to the finger, the distance to the finger becomes very short, instead if the current enters the emitter between the fingers, then the length of the resistance path the carrier must pass through is half the grid spacing as described in equation (5), It is well known that there is a relationship between the power loss (P_{loss}), the sheet resistance (R_s), and the distance (S) between finger grids in PV devices: [10]

$$p_{loss\%} = \frac{J_{mp}}{12V_{mp}} R_s \cdot S^2 \quad (5)$$

where J_{mp} and V_{mp} are the short-circuit current and open-circuit voltage at maximum power, respectively. For example, for a typical silicon solar cell with R_s = 100 Ω/sq, J_{mp} = 30 mA/cm^2, and V_{mp} = 450 mV, the finger spacing should be 2.65 mm for a 4% power loss. Contact resistance loss occurs at the interface between the silicon solar cell and the metal contact. In order to keep the contact resistance low, the top n + layer should be doped as high as possible. However, higher doping concentrations cause other problems. When a high concentration of phosphorus diffuses into the silicon, excess phosphorous is placed on the surface of the solar cell, which forms a "dead layer" where there is little chance for photogenerated carriers to be collected. Many commercial solar cells have very poor blue light response because of this dead layer. Therefore, the area under the contact should be heavily doped, while the doping of the emitter lowers the saturation current in the emitter and the diffusion length of the emitter.

2.3. Si / Oxide hetero-interfaces

The Si / oxide hetero-interfaces are firstly used for the antireflection layer for Si Solar cells [11-13]. Bare silicon has a high surface reflectance of 30% director. Reflectance can be reduced by texturing and can also be reduced by applying an anti-reflective coating to the surface [14]. Antireflective coatings formed on solar cells are similar to those used in other optical devices such as camera lenses. The coating consists of a thin layer of oxide materials, with a suitable choice of thickness so that the waves reflected at the antireflective surface layer are out of phase with the waves reflected at the semiconductor surface. Waves with different phases interfere with each other destructively, resulting in zero reflected net energy. In addition to the antireflective coatings, the interference effect is often encountered where a thin layer of oil on the water creates a rainbow-like band. Since the color of the oxide film is affected not only by the refractive index but also by the thickness, There are various ways in determining to maximize antireflection properties[13, 15].

As mentioned earlier, the field-effect passivation to reduce recombination has been widely used in Si photovoltaic technologies by taking advantage of oxide thin films with Al_2O_3, SiN_x, ZrO_x, and TaO_x [16-19]. In this case, the electric field is established by a fixed charge density from the dielectric film leading to the band bending of Si. Among them, Al_2O_3 is considered to be the most preferred way to generally adapt to the Si solar cells due to their excellent passivation effect. Thus, the state-art-of Si solar cells such as passivated emitter rear cell (PERC) [20, 21], heterojunction with an intrinsic thin layer (HIT) [22] or interdigitated back contacts (IBC) [23] with photovoltaic conversion efficiency (PCE) of 23 ~ 26 % have been developed, minimizing the recombinations at the surfaces. However, such passivation techniques generally require heavy and expensive vacuum processes, including plasma-enhanced chemical vapor deposition (CVD) and atomic layer deposition. Moreover, conventional thin-film based passivation is stable but accompanied by additional chemical, post-annealing at high temperature or under the forming gas to enhance the passivation quality.

2.4. Si / Organic hetero-interfaces

Organics that can be processed at low temperatures through solution processes have recently been reviewed in the field of Si-based photovoltaics [24-28]. In particular, the hetero-interface between Si and organics is very attractive for use as a junction or passivation layer. Si / organic hybrid solar cells with carrier selective functional layers such as crystalline silicon and poly (3,4-ethylenedioxyphene): Poly (styrene sulfonate) (PEDOT: PSS) is a promising device concept for low-cost Si photovoltaic cells [29]. This is possible not only by the Si substrate and charge transport layer but also by the electronic state associated with the non-passivated interface state [25]. n-Si / PEDOT: Interface engineering for splicing is important for performance enhancement because it optimizes carrier separation, minimizes interface recombination, and enhances reversal effects. Previous attempts at integrating texture-Si into hybrid solar cells have aimed to modify the shape of the surface texture to have a large opening area and shallow depth to facilitate the deposition of PEDOT: PSS with improved coverage[30]. Another strategy is to insert a small molecule layer between the textured Si and PEDOT: PSS to partially passivate the uncovered Si portion to inhibit some charge recombination[24]. However, despite these improvements, the efficiency of the structured device is still much lower than the planar device, mainly due to the significant recombination that occurs at passivated junctions. From these analyzes, it is assumed that the inefficiency of carrier collection cannot be overcome without full conformal and intimate contact between PEDOT: PSS and the textured Si surface. Therefore, new strategies and insights are needed to improve the quality and performance of texture-Si / PEDOT: PSS solar cells.

On the other hand, in terms of passivation, organic acetate, polystyrene sulfonate and nafion have recently been reported as superior passivation layers for Si than previous organics, resulting in low τ_{eff} and poor air exposure life [31-33]. In particular, Nafion films with dip- or spin-coating are effective for both p and n-type Si and provide Si surface passivation up to τ_{eff} = 9-12 ms [34]. However, their passivation mechanisms effective for both types of Si are not clearly understood and still require further investigation. In addition, there is little discussion of organic passivation layers for practical applications in Si-based photovoltaic devices.

2.5 References

1. Soref, R. A. SILICON-BASED OPTOELECTRONICS. *Proceedings of the Ieee* **81**, 1687-1706 (1993).
2. Yan, R. H., et al. SCALING THE SI MOSFET - FROM BULK TO SOI TO BULK. *Ieee Transactions on Electron Devices* **39**, 1704-1710 (1992).
3. Sze, S. M., et al. AVALANCHE BREAKDOWN VOLTAGES OF ABRUPT AND LINEARLY GRADED P-N JUNCTIONS IN GE SI GAAS AND GAP - (DOPANT EFFECTS IMPURITY EFFECTS T). *Appl Phys Lett* **8**, 111 (1966).
4. Crowell, C. R., et al. TEMPERATURE DEPENDENCE OF AVALANCHE MULTIPLICATION IN SEMICONDUCTORS. *Appl Phys Lett* **9**, 242 (1966).
5. Sze, S. M., et al. RESISTIVITY MOBILITY AND IMPURITY LEVELS IN GAAS GE AND SI AT 300 DEGREES K. *Solid-State Electronics* **11**, 599 (1968).

6. Sze, S. M., et al. EFFECT OF JUNCTION CURVATURE ON BREAKDOWN VOLTAGE IN SEMICONDUCTORS. *Solid-State Electronics* **9**, 831 (1966).

7. Cowley, A. M., et al. SURFACE STATES AND BARRIER HEIGHT OF METAL-SEMICONDUCTOR SYSTEMS. *Journal of Applied Physics* **36**, 3212 (1965).

8. Crowell, C. R., et al. CURRENT TRANSPORT IN METAL-SEMICONDUCTOR BARRIERS. *Solid-State Electronics* **9**, 1035 (1966).

9. Sze, S. M., et al. CURRENT TRANSPORT IN METAL-SEMICONDUCTOR-METAL (MSM) STRUCTURES. *Solid-State Electronics* **14**, 1209 (1971).

10. Kang, S. B., et al. Transfer of ultrathin molybdenum disulfide and transparent nanomesh electrode onto silicon for efficient heterojunction solar cells. *Nano Energy* **50**, 649-658 (2018).

11. Chaneliere, C., et al. Tantalum pentoxide (Ta2O5) thin films for advanced dielectric applications. *Materials Science & Engineering R-Reports* **22**, 269-322 (1998).

12. Lee, Y. J., et al. ZnO nanostructures as efficient antireflection layers in solar cells. *Nano Letters* **8**, 1501-1505 (2008).

13. Xi, J. Q., et al. Optical thin-film materials with low refractive index for broadband elimination of Fresnel reflection. *Nature Photonics* **1**, 176-179 (2007).

14. Zhu, J., et al. Optical Absorption Enhancement in Amorphous Silicon Nanowire and Nanocone Arrays. *Nano Letters* **9**, 279-282 (2009).

15. Sun, S. L., et al. High-Efficiency Broadband Anomalous Reflection by Gradient Meta-Surfaces. *Nano Letters* **12**, 6223-6229 (2012).

16. Agostinelli, G., et al. Very low surface recombination velocities on p-type silicon wafers passivated with a dielectric with fixed negative charge. *Solar Energy Materials and Solar Cells* **90**, 3438-3443 (2006).

17. Bonilla, R. S., et al. Dielectric surface passivation for silicon solar cells: A review. *physica status solidi (a)* **214**, 1700293 (2017).

18. Dingemans, G., et al. Influence of annealing and Al2O3 properties on the hydrogen-induced passivation of the Si/SiO2 interface. *Journal of Applied Physics* **111**, (2012).

19. Wan, Y. M., et al. Zirconium oxide surface passivation of crystalline silicon. *Appl Phys Lett* **112**, (2018).

20. Green, M. A. The Passivated Emitter and Rear Cell (PERC): From conception to mass production. *Solar Energy Materials and Solar Cells* **143**, 190-197 (2015).

21. Horbelt, R., et al. Surface Recombination Velocity of Local Al-contacts of PERC Solar Cells Determined from LBIC Measurements and 2D Simulation. *Energy Procedia* **92**, 82-87 (2016).

22. Masuko, K., et al. Achievement of More Than 25% Conversion Efficiency With Crystalline Silicon Heterojunction Solar Cell. *Ieee Journal of Photovoltaics* **4**, 1433-1435 (2014).

23. Yoshikawa, K., et al. Silicon heterojunction solar cell with interdigitated back contacts for a photoconversion efficiency over 26%. *Nat Energy* **2** (2017).

24. Yu, P. C., et al. 13% Efficiency Hybrid Organic/Silicon-Nanowire Heterojunction Solar Cell via Interface Engineering. *Acs Nano* **7**, 10780-10787 (2013).

25. Zhang, X., et al. Improved PEDOT:PSS/c-Si hybrid solar cell using inverted structure and effective passivation. *Sci Rep* **6**, 35091 (2016).

26. Zhang, Y., et al. High efficiency hybrid PEDOT:PSS/nanostructured silicon Schottky junction solar cells by doping-free rear contact. *Energy & Environmental Science* **8**, 297-302 (2015).

27. Zielke, D., et al. Organic-silicon Solar Cells Exceeding 20% Efficiency. *Energy Procedia* **77**, 331-339 (2015).

28. Zielke, D., et al. Organic-silicon heterojunction solar cells on n-type silicon wafers: The BackPEDOT concept. *Solar Energy Materials and Solar Cells* **131**, 110-116 (2014).

29. Yoon, S.-S., et al. High Efficiency (>17%) Si-Organic Hybrid Solar Cells by Simultaneous Structural, Electrical, and Interfacial Engineering via Low-Temperature Processes. *Advanced Energy Materials* **8**, 1702655 (2018).

30. Yang, Z., et al. Tuning of the Contact Properties for High-Efficiency Si/PEDOT:PSS Heterojunction Solar Cells. *ACS Energy Letters* **2**, 556-562 (2017).

31. Chen, J., et al. Vacuum-Free, Room-Temperature Organic Passivation of Silicon: Toward Very Low Recombination of Micro-/Nanotextured Surface Structures. *ACS Appl Mater Interfaces* **10**, 44890-44896 (2018).

32. Chen, J. H., et al. Electrochemical grafting passivation of silicon via electron transfer at polymer/silicon hybrid interface. *Electrochimica Acta* **247**, 826-834 (2017).

33. Bullock, J., et al. Superacid Passivation of Crystalline Silicon Surfaces. *ACS Appl Mater Interfaces* **8**, 24205-24211 (2016).

34. Ji, W., et al. Dip Coating Passivation of Crystalline Silicon by Lewis Acids. *ACS Nano* **13**, 3723-3729 (2019).

CHAPTER 3. Si / PEDOT:PSS hetero-interfaces for transparent solar cells

3.1 Research background

Transparent solar cells (TSC) are a new device that combines the advantages of visible transparency and light-to-electrical conversion. Currently, conventional TSCs are mainly based on organics, dyes and perovskite. However, the stiffness and hue transparency characteristics of these devices greatly limit the usefulness of TSCs in practical applications. Here, we show a flexible color-neutral and high-efficiency TSC based on standalone n-silicon microwires (SiMW). Spaced flat tip SiMW is manufactured through deep reactive ion etching and embedded in a standalone transparent polymer matrix. By adjusting the spacing between the microwires, the light transmittance can be adjusted from ˜10% to 55%. In the case of TSC, the heterojunction is formed of a p-type polymer on top of the n-type flat SiMW, ohmic contact with the indium-doped ZnO film occurs at the bottom and an Aluminium-oxide passivation layer occurs at the side. Inclined tip tips are also developed by new solvent assisted wet etching to manipulate light absorption. Finite-difference time domain simulations showed that the light reflected from the SiMW slope assisted the photo-material interaction in adjacent microwires. Based on the sloped SiMPF, the TSC shows 8% efficiency at 10% visible transparency with flexibility. This efficiency is the highest among Si-based TSCs and can be compared with state-of-the-art neutral color TSCs based on organic-inorganic hybrid perovskite and organics. In addition, unlike other studies, the scalable and transparent platform of this research is promising for TSC in the future. Transparent solar cells (TSC) are emerging as building blocks for building integrated power generation [1-4]. In this attractive photovoltaic concept, there is an inevitable trade-off between energy generation (i.e. photoelectric conversion efficiency (PCE)) and light transmission (visible transparency). Thus, based on the criteria of transparent solar cells, there is an inevitable compromise of efficiency to achieve transparency. The most common way to develop transparent solar cells is to use bandgap engineering of active materials that can selectively absorb sunlight to achieve tint transparency.[5-9] For example, if the active layer is designed to absorb short wavelength light and transmit long wavelength light in the visible range (λ> 600 nm), the transparent element is yellow or red. [7-14]. Previous attempts have been made to develop transparent solar cells using dyes as active materials. To obtain a fully transparent dye-sensitized solar cell, the design of a new dye-sensitizer, which determines the absorption of visible light in the device, can be effective [15, 16]. In addition, all components (including TiO2 and electrodes) are transparent [17-19]. Through this strategy, some groups demonstrated various colored transparent solar cells with low PCE of ~ 3-7% at medium transparency [15-19]. However, this colored transparency is not suitable for electronic, car windows and office building integrated solar windows. Recently, attention has been drawn to the field of photovoltaic cells with an emphasis on organic-inorganic hybrid perovskite materials [20-23]. The material of this ABX3 structure shows an appropriate band gap and high absorption coefficient, which is an interesting class of photovoltaic cells [24-28]. Many groups have achieved halide perovskite-based transparent solar cells by controlling the thickness, transport layer and composition of the perovskite. Introducing a thin layer with a bandgap engineering perovskite layer is a well known technique for achieving transparent solar cells [29,30]. Roldán-Carmona et al. In addition, common methyl ammonium lead iodide was used as a sorbent with varying thicknesses to obtain a PCE of 6.4% 9. In addition, Jung et al. And Heo et al. Perovskite-based translucent solar cells with PCE of 10% [8, 31] and above were demonstrated. However, despite the high PCE, these devices again have tint transparency due to transparency. The color is damaged. In general, since the perovskite was designed to absorb part of the visible range of the solar spectrum as the active layer of the transparent solar cell, the device exhibited brown-yellow transparency. In addition, the thinning of the active layer or the engineering of the band gap is highly dependent on the material [5, 7, 12, 14], so the approach to achieving transparency is quite limited. On the other hand, by using the designed semiconductor polymer, transparent cathedral high efficiency was achieved using an organic transparent solar cell. However, as in the case of dyes and perovskite, custom polymers, which are a requirement for neutral color transparent solar cells, are difficult to obtain spectral flat absorption over the entire visible spectrum. Thus, Cui et al. The ultra low band gap fullerene receptor was used to obtain PCE 8.38% with 25.7% visibility transparency, and the device was transparent only in the turquoise region of the visible light spectrum [32]. Liu et al. Have developed a new electron acceptor material exhibiting strong NIR absorption between 600 and 940 nm and successfully applied it to transparent solar cells with transparency in blue tones. [33]. Coloring transparency of perovskite and organic TSC is a major obstacle. On real applications. Here, we show a true color transparent solar cell. Adjustable spacing crystalline n-Si microwire arrays are manufactured through deep reactive ion etching and embedded in a transparent polymer matrix. Subsequently, through a combination of dry and wet etching, a standalone Si microwire array polymer composite film (SiMPF) is obtained by applying a mechanical peel technique. In addition, a p-type conductive polymer is applied on the n-Si tip to form a junction between the polymer and n-Si and produce a neutral colored transparent solar cell. The slanted tip of the n-SiMPF-based transparent solar cell, with its flexibility, provides power conversion efficiency from 10% to 8.07% visibility transparency. The developed device offers similar performance to conventional TSCs, mainly based on perovskite, dyes and organics. In addition, this rugged, ultralight and stretchable platform is a promising technology that future transparent and stretchable solar cells can expand their applications.

3.2 Experimental details

Preparation of Si Micro Wire Arrays

Silicon micro wire arrays were fabricated using n-Si wafers (Czochralski-grown, 525 ± 25 µm thickness, 0.01-0.02 Ω cm, Unisill Inc.). A 20 nm thick conformal SiO 2 oxide layer was grown by dry thermal oxidation at 1000°C for 30 minutes under pure O_2 atmosphere. Thereafter, a 70 nm SiO_2 thin film was deposited by plasma enhanced chemical vapor deposition (PEH-600, Sorona). Circular dot arrays (diameter 2µm, 4,5,6 and 7µm center distances) were patterned on Si substrates by image reversal photolithography using AZ5214 (AZ Electronic Materials) instrument. After depositing Cr (300 nm) on the patterned Si photoresist, the residue was removed with acetone to produce a Cr micro dot array as a metal mask of Si microwires. Si was then etched by deep reactive ion etching (DRIE) (tag 200). The DRIE process was performed using SF6 (250 sccm) / C4F8 (150 sccm) in periodic etching mode and passivated to 1500 W source power using 40 mTorr gas pressure and 100 W stage power. The Cr metal mask was removed with Cr etchant after the DRIE process.

Preparation of Si Micro Wire Array / PDMS

A 15 nm thick Aluminium-oxide layer was deposited on the Si microwire array by atomic layer deposition (Lucida D100, NCD) to passivate the Si layer. Aluminium-oxide-coated Si microwire arrays were treated with O2 plasma by reactive ion etching (RIE, Labstar) for uniform coating with PDMS. The microwire array was then coated with a solution containing 5 g hexa methyl cyclotrisiloxane (Sigma Aldrich), 1 g PDMS (Sylgard 184, Dow Corning), 0.10 g PDMS curing agent and 5 ml dichloromethane. The solution was spin coated on the sample at 800 rpm for 120 seconds and at 1200 rpm for 10 seconds and cured at 100 ° C. for 20 minutes. PDMS etching was performed to expose the tips of the Si microwires through the RIE at 500 W of RF power. The sample is placed in a chamber at a pressure of 60 mTorr; The total gas flow rate was 80 sccm and the O 2 gas and SF 6 gas flow rates were 50 and 30 sccm, respectively.

Preparation of Independently Inclined SiMPF: After dry etching of residual PDMS, only the top of the Al203 coated Si microwires is exposed. In addition to this, the filled PDMS remains in the Aluminium-oxide coated Si microwires and protects the etching of Aluminium-oxide in other parts. Thereafter, the exposed Aluminium-oxide layer on the upper Si microwire was etched with 85% H 3 PO 4 at 50 ° C. for 180 seconds. Thereafter, the Si microwire array was chemically etched with a solution containing HF / HNO3 / CH3COOH / DMF at a volume ratio of 3: 6: 0.3: 0.7. A detailed and complete etching process for fabricating slanted tips of Si microwire-PDMS composite films is illustrated in Figure 25. Si micro wire array-PDMS composite films were mechanically peeled from the parent substrate. For proper contact with the bottom electrode and the top junction layer, the composite was slightly etched with a 1: 2 mixture of 1.0M tetra butyl ammonium fluoride in tetrahydrofuran (Sigma Aldrich) and dimethyl formamide for 10 seconds. A 200 nm thick indium doped ZnO thin film was coated on the composite film as the bottom electrode by RF sputtering (Infovion). A high conductivity PEDOT: PSS (CLEVIOS PH 1000) solution containing 9 wt% ethylene glycol and 0.1 wt% Triton X-100 was spin coated onto the composite film to form a junction.

Optical Simulation of Si Microwire Arrays:

Numerical simulations were performed using Lumerical Finite Difference Time Domain (FDTD) as a time-dependent Maxwell's equation solver. Material data from the literature was used to provide refractive index information for Si, PDMS, and Aluminium-oxide. As a simulation condition of incident light, plane waves parallel to the microwires were used. As the boundary conditions of the simulation, the bleach boundary conditions were used in the x and y directions, and the perfectly matching layer boundaries were used in the z direction. For the absorption and reflection spectra of the microwires and the time-resolved reflected light, simulations were performed using the same parameters used in the experiments.

Characteristics of Transparent Solar Cells:

The morphology of Si microwires and composites was characterized by field emission scanning electron microscopy (Quanta200 FE-SEM, FEI). Transmittance and reflectance of Si microwire-PDMS composite films were measured using a UV-vis-NIR spectrophotometer (Cary 5000, Agilent) with an integrating sphere to describe the total diffuse and reflected light reflected and transmitted from the sample. Was measured. The color coordinates of the samples were recorded with a goniometer (Neolight G500, PIMAX) equipped with a small array spectrometer (CAS 140 CT, instrument system) using one-sun illumination. External quantum efficiency spectra were recorded in the wavelength range of 400-1100 nm using xenon light sources and monochromators. The active area of the device is 0.5 × 0.5 cm2. A shadow mask of 0.25 cm2 area was also used to accurately define the active area. Thus solar cell results were referred to as active regions. The photovoltaic performance of the solar cells was examined under AM 1.5G illumination using a solar simulator. Incident fluxes were identified using NREL-calibrated solar cells (PV Measurements, Inc.).technologies should be low cost, high stability, and high efficiency.

3.3 Results and Discussion

Figure 1a shows the entire manufacturing process of TSC based on a standalone film of n-type SiMW array embedded in poly (dimethyl siloxane) (PDMS). As shown in figure 1b, a hexagonal array of microwires 2 μm in diameter and 30 μm in length was prepared by a photolithography process including reactive ion etching (RIE) using a Cr dot array as an etching mask. Secondly, a 15 nm thick Al 2 O 3 layer is deposited on the SiMW by atomic layer deposition (ALD) to passivate the Si surface. Compared with conventional silicon solar cells, the standalone SiMPF-based TSC in this study has a very high surface area. Therefore, proper surface passivation is essential. As can be seen in Figure 2, TSCs without Al2O3 passivation have very low leakage currents due to surface defects, resulting in very low short circuit current density (Jsc) and open voltage (Voc). Third, SiMW arrays were embedded in PDMS through spin coating. PDMS embedding was performed by a two step spin coating process consisting of a primary spinning for 120 seconds at 600 rpm and a secondary spinning process for 10 seconds at 1500 rpm. In the first step, PDMS conformally and densely fills the SiMW array. Excess PDMS residue on top of the SiMW was removed during the second spin coating. Al2O3-coated SiMW arrays were found to be hydrophobic enough that PDMS could not penetrate deep into the bottom of SiMW, and the adhesion between SiMW and PDMS was not very strong. Thus, PDMS was easily stripped from the SiMW array in the second spin coating step (Figures 3a and b). The surface of Al2O3-coated SiMW was treated with O2-plasma to improve adhesion between Al2O3 surface and PDMS due to covalent bonding of O-Si [34-36]. Figure 1c shows an SEM image of a SiMW array embedded in a PDMS, where PDMS can be seen deeply penetrating into the bottom of the SiMW array after oxygen plasma treatment. Fourth, the residual PDMS layer was removed by dry etching using a gas mixture of O 2 and SF 6. PDMS can be selectively etched because SFMW is protected by SiMW by an Al2O3 film etched very slowly by SF6 gas. Fifth, the SiMW array embedded in the PDMS was peeled from the Si wafer to generate a flexible standalone SiMW array-PDMS composite film (SiMPF) as shown in figure 1d. As indicated by the hexagonal array of diffraction spots when the SiMPF is illuminated vertically with a 532nm diode laser, the pitch and hexagonal array of the SiMW array was maintained even after peeling off the parent substrate (Figure 4). Finally, the TSC process was completed by forming a hetero p-n junction of indium doped zinc oxide (IZO) ohmic contacts at the bottom of the PEDOT: PSS and SiMPF at the exposed tip.

After changing the pitch defined by the distance between the centers of the microwires from 4 to 7 μm in 1 μm intervals (Figure 6), Figures 6a and b represent the current density (J) -voltage (V)) Characteristics and External Quantum Efficiency (EQE) of TSC Based on Flat SiMW Arrays. A summary of device characteristics is presented in Table 1. In addition, the Jsc, Voc and efficiency of the eight solar cells made with pitch indicate that the box distribution is quite narrow, indicating that this manufacturing process is fairly reproducible as shown in figure 7. Compared to bulk solar cells, nanowire or microwire solar cells typically have a very large surface area and thus have a high concentration of surface defects that act as leakage current paths [37, 38]. However, the deposited Al2O3 layer has a very low density of interface defects [39-41]. Therefore, surface defects and dangling bonds can be effectively passivated. In addition, parasitic shunts do not occur when negative charges are present at the interface with silicon [42]. Thus, as shown in Figure 6a and Table 1, the photovoltaic parameters of the 4 μm-pitch cell were 0.542 V and 68.1%, respectively, which can be compared with the bulk counterparts. This means that the heterojunction between n-type Si and p-type PEDOT: PSS acts as an excellent rectifying junction, and the Al2O3 layer also efficiently passivates silicon surface defects. As the pitch of SiMW increased, the Jsc of TSC decreased, which can be explained by the decrease in light absorption. As the pitch increased from 4 μm to 7 μm, the average light absorption of TSC decreased from 78.11 to 38.71% at a wavelength of 400-1100 nm (Table 2). This is in good agreement with the reduction in Jsc. Similar to the change in Jsc, Voc is also inversely proportional to the light transmittance since the Voc of a conventional solar cell is related to photocurrent (IL) and saturation current (I0) as follows: Voc to ln (for IL / optical transparency) Due to the dependence of Voc and Jsc, the efficiency of TSCs also has a trade off with optical transparency, which is inevitable in TSCs.

Nanowire arrays are known to have excellent anti-reflective properties due to graded refractive index effects and light trapping [45-48]. Thus, nanowire arrays can have lower reflectance than microwire arrays. However, nanowire arrays are made by top-down methods [49-51] that include electron beam lithography and subsequently by etching or bottom-up methods [52-54] that include vapor-liquid-solid methods. Both have very limited scalability of the whole area. Moreover, these arrays have a very high surface-to-volume ratio, which increases the likelihood of surface recombination and degrades performance. [38, 55, 56]. In contrast, wafer scale microwire arrays are manufactured by widely used photolithography and etching processes. In the semiconductor industry. In addition, microwire arrays are advantageous for forming effective junctions and are easy to collect carriers [37, 57]. Thus, SiMW with reduced reflectance could be a promising candidate for TSC. Assuming that the reflectance of SiMW is proportional to the area of the upper flat surface of the microwire array, the average calculated reflectance obtained with SiMW with a pitch of 4 μm is as high as 9.54% (Figure 8a). Thus, to reduce high reflectance from flat SiMW tips, antireflective (AR) coating or surface texturing techniques typically employed in bulk silicon solar cells can be applied.

First, a TSC with a 70 nm thick SiN AR coating on a SiMW tip deposited by plasma enhanced chemical vapor deposition (PECVD) was prepared. Figure 8b shows the J-V characteristics of a TSC based on a 4μm pitch SiMW array using SiNx. With the use of antireflective films, Jsc increased from 17.07 to 18.94 mA cm[-2], but Voc and FF decreased simultaneously, which did not significantly improve efficiency compared to TSC without a SiN layer. The reduction in Voc can be due to the fact that n-Si and p-PEDOT heterojunctions are formed only on the side, not on the top surface of SiMW, which do not efficiently separate the electron-hole pairs. Thus, an attempt was made to reduce light reflection by changing the shape of the flat SiMW tip (Figure 9a). For this purpose, a 70 nm thick SiO2 thin film was formed on the tip of the SiMW as an etching mask, and the SiMW was chemically etched using a hydrofluoric acid-nitric acid-acetic acid (HNA) mixed solution [58-61]. Silicon etching with HNA solution proceeds in three steps:

$$Si + 2H^{+} \rightarrow 2Si^{2+} + H_2 \qquad (1)$$

$$Si^{2+} + 2OH^{-} \rightarrow Si(OH)_2 \rightarrow SiO_2 + H_2 \qquad (2)$$

$$SiO_2 + 6HF \rightarrow H_2SiF_6 \qquad (3)$$

The overall reaction is initiated by breaking the covalent bond between silicon atoms by H + ions supplied from HNO3 to produce SiO2 by recombination of Si 2 + ions and hydroxide ions. HF then dissolves the silicon dioxide to produce an aqueous salt. CH3COOH, on the other hand, acts as a diluent to prevent excessive dissociation of HNO3 and to adjust the etch rate and roughness of the etched surface. SiMPF was intensely etched and even partially removed from the PDMS matrix in the HNA solution with a composition of 3: 7: 0, but the etch rate was significantly attenuated in the HNA etch solution with the 3: 6: 1 composition (Figure 10a and b). However, SiMW is still etched extensively by solution leaving only the Al2O3 layer. In order to reduce the etch rate and change the behavior of HF-based etching, various additives, including organics, have been introduced into HF solutions [61, 62]. Surprisingly, the etching rate was greatly reduced by the etching solution with DMF added instead of acetic acid. And this dramatically changed the shape of the SiMW tip (Figure 10c). Interactions between HF and DMF molecules form heterogeneous bonds. This hetero bond has a pyramidal molecular structure consisting of three H-F bonds (H on DMF and F on HF), which causes redistribution of the electron density of HF, which greatly reduces the etching rate of SiO2. As a result, the etching rate of the native oxide (etching intermediate) as well as the etch oxide of the SiO2 etch mask layer on the top surface of the SiMW is significantly reduced, maintaining the shape of the SiMW tip while maintaining the overall shape of the SiMW. In addition, a series of etching experiments were carried out with varying volume ratios of HF-HNO3-CH3COOH-DMF (HNAD) etching solution and found that HNAD solutions with volume ratios of 30: 60: 3: 7 produce SiMW well. Defined and uniform inclined tip as shown in Figure 9b. The measured angle of the inclined SiMW tip was ˜54.7 mm3. Simulation of the angle dependent reflection of the inclined tip also shows that the reflectance reaches saturation after decreasing to 45 ° (Figure 9c). Finite differential time domain (FDTD) simulations were performed to study the reflection and absorption of light from planar and slanted SiMW tips. About 40% of visible and infrared light was reflected back from SiMPF with flat tips; Therefore, the intensity of the electric field inside the SiMW was low (Figure 9d). On the other hand, the light incident on the inclined tip of the SiMW is reflected back toward the inside of the SiMPF and eventually reabsorbed by the adjacent SiMW to increase the intensity of the electric field inside the SiMW. In addition, the low reflectance of the inclined tip SiMPF is mainly due to the reabsorption of light reflected from the inclined tip by the adjacent microwires (Figure 9e). The time difference between the two absorption events provides evidence that the light reflected from the slope Mw is reabsorbed in the adjacent Si Mw. After 10.5 fs, the electromagnetic energy inside Si Mw increases again, indicating that the reflected light propagates to adjacent Si Mw for 10.5 fs. When multiplied by the group velocity of their pulses 64, it corresponds to 3.17um. This is in good agreement with the distance between the center of the Si MW and the edge side of the adjacent Si MW, indicating that the light reflected from the slanted tip is absorbed back into the adjacent wire (Figure 9f). Thus, the absorbed electromagnetic energy of the inclined microwire consists of the electric field of the first unreflected light (white arrow, figure 9d) and the scattered electric field of red-absorbed light of the refracted light (red arrow, figure 9e). 2G-i show the reflection, transmission and absorption spectra of SiMPF with flat and inclined tips as a function of pitch obtained by UV-Vis spectroscopy measurements. As expected, the average reflectance sharply decreased from 10.48-13.90% for flat SiMPF to 1.81-3.45% for tilted counterparts (Table 3). In particular, flat SiMPFs with a pitch of 4 μm or the highest density of microwires had the lowest reflectance. This can be explained by the effect of light trapping by scattering and diffraction due to the narrow spacing (~ 2 μm) between the Si MW [65, 66]. The transmission spectra of planar and slanted SiMPF were determined mainly by pitch, and were similar except that the transmittance of the slanted wavelength was slightly lower than that of the planar sample in the long wavelength region. The extinction coefficient of silicon is small due to the indirect band gap structure and tends to decrease exponentially with increasing wavelengths [67, 68]. Thus, the 30 μm thick silicon layer used in this study may not fully absorb 1- illumination. 69. To determine the origin of this difference in the transmittances of flat and sloped samples, a time-resolved light tracking simulation was performed. It was performed at two wavelengths (short: 550nm) and (long: 900nm). For short wavelength incident light, the light intensity rapidly attenuates as the depth of the microwire increases for both flat and slanted samples, indicating that the short wavelength light is fully absorbed by 30 μm thick Si (Figures 11a and b). . On the other hand, in the case of having long wavelength incident light on a flat SiMW, the light absorption was so weak that a substantial portion of the light was transmitted through the bottom of the SiMW (Figure 12a). However, when long wavelength light was incident on the inclined tip having an incident angle of 50 °, the light was refracted at the air-silicon interface so that the light inside the microwire followed the zigzag path (Figure 12b). Increase the effective light path or decrease the transmittance (Figure 9h). As a result, the absorption calculated from the reflection and transmittance data was significantly improved in the gradient SiMPF (Figure 9I). For example, absorption in SiMW with a pitch of 5 μm increased from 59.24% for flat samples to 72.80% (increasing 13.56%) for tilted relative. Average reflectance, transmittance and absorption of the flat and sloped SiMPFs are summarized in Tables 2 and 3. When applying TSC, the haze value is important. This is because the haze value can reduce the sharpness when viewing something. Haze values represent light scattering and were calculated using the following equation:

$$\text{Haze (\%)} = T\_{\text{Diffusion}} / T\_{\text{Total}}$$

Where T total is total transmittance and T diffuse is diffuse transmittance (detailed measurement methods and additional information in Figure 13) [70, 71]. As expected, the narrower the pitch between the microwires, the higher the actual scattering. Thus, samples with tighter pitches showed higher haze ratios. At a narrow pitch of 4um, haze values greater than 15% are relatively high. On the other hand, a sample with 7um pitch shows very low haze of ~ 2.5%, which can also be compared with ultra-thin silver nanowires with indium tin oxide or haze varieties of 1-3% (Figure S14a) [72-74] . Interestingly, the denser the pitch, the larger the haze ratio difference between flat and sloped. The inclined tip of the microwire causes the light inside the microwire to follow the zigzag path (path "A" in Figure 14b) or reflect back toward the adjacent microwire (path "B" in Figure 14b). Light along the path "A" is almost absorbed. On the other hand, the light of path "B" causes a second scattering into adjacent Si, so that the haze can be increased for a particularly dense pitch of the sample. Figure 15a is an optical photograph showing the neutral color perception of SiMPF with controlled pitch, unlike perovskite filters. Samples with pitches of 7 um (I), 6 um (II), 5 um (III) and 4 um (IV) were displayed on the college logo background. Transparency changed according to pitch, but color was recognized without distortion. For accurate evaluation of color recognition, SiMPF was illuminated with simulated AM1.5 light, and the color coordinates of the transmitted light are shown in the CIE 1931 chromaticity diagram as shown in Figure 15b and Table 4. The color coordinates of the various dyes commonly used for dye-sensitized solar cells (DSSC) and MAPbIxBr3xx perovskite films are also shown. In this study, perovskite thin films were prepared and dye data for DSSC were referenced in other publications [16, 75, 76]. The dye is green or blue tint and the perovskite film is reddish brown to yellow (Figure 16, SiMPF in this study has chromaticity coordinates in the central region of the chromaticity diagram). Figure 15c shows the IV characteristics of a TSC using tilted SiMPF, and detailed photovoltaic power performance is summarized in Table 5. Since HNAD etching only affects the top of the already exposed Si microwires in the first step, they still exist regardless of the flat and tilted tip of the Al2O3 passivation microwire array on the side. Thus, compared to TSC based on flat SiMPF, the Voc and FF of the tilting device remained unchanged, while the Jsc increased significantly. In addition, manufacturing processes involving HNAD etching are still reproducible. As shown in Figure 17, the box plot of the photovoltaic parameters of the slanted SiMPF also has a narrow distribution. Interestingly, the improvement in Jsc (ΔJsc) increased as the pitch of SiMPF increased, which is in good agreement with the change in light absorption as a function of the pitch of the flat sloped sample. TSCs with a pitch of 4 μm showed the highest efficiency of 8.07%. Figure 15d shows the EQE spectrum of a gradient TSC with a different pitch of 4-7 μm in the wavelength range of 400-1100 nm. Integrated Jsc matches that determined from the J-V curve. Comparing the EQE of the flat and sloped samples showed a significant increase in the current density of the sloped sample in the near-infrared region rather than in the visible region (Figure 18). In other words, improving the efficiency of TSCs is achieved by improving absorption in the near infrared region (800-1100 nm) without compromising visible transparency, one of the main parameters of TSCs. Figure 15e shows a plot of the efficiency versus average transmittance of visible light in various neutral colored transparent solar cells, including those based on perovskite, organic semiconductors, and amorphous silicon. Zhang et al. Taking advantage of the NIR non fullerene receptor at a light transmittance of 20% [77], it demonstrated ~ 9% neutral color TSC. Chueh et al. By reducing the thickness of the light absorbing layer and the silver electrode in the organic solar cell was prepared TSC with an efficiency of 5.63% at a light transmittance of 13%. Yi et al. Metal electrodes were replaced with graphene electrodes, showing a transparent organic solar cell that achieved an efficiency of 3.8% at 79% with transparent visibility. Eperon et al. Introduced a microstructured perovskite and enabled the transmission of light through the device, achieving an efficiency of ~ 7% at visible transparency of 8%[80]. Alternatively, even when a thin layer of a-Si (<300 nm) was used for the active layer of TSCs [81], the adjustable transparency range was very limited. As the transmittance increases, an uncontrolled shunt path is formed into thin a-Si, which results in a significant loss of efficiency, further worsening the transmittance gain. Overall performance is comparable to the latest TSCs based on organic or perovskite, but slightly lower in transparency compared to TSC (T> 30%) with high transmission. To improve transparency, the surface treatment of PDMS that fills the spaces between the microwires can be further considered for future work. However, the transparency of the device based on the SiMPF platform can be easily adjusted from 10% to 55% by changing the gap between Si MWs, unlike other developed TSCs. More importantly, SiMPF-based TSCs can be applied as flexible solar cells due to the thinness of the device and the inherent robustness of PDMS [82-84], while most of the currently reported TSCs using organics or perovskite are rigid without flexibility. Glass. TSCs are characterized after bending and periodic bending tests. Interestingly, the performance of transparent solar cells consisting of PEDOT: PSS / Si Mw – PDMS composites / IZO does not significantly decrease in the bending state of 12 mm and 6 mm bend radii (Figures 19a and 19b). Photonic parameters of the device in the bent state are summarized in Table 6. In addition, as shown in Figure 19c, after a cyclic bending test with a bending radius of 6 mm, the normalized efficiency is maintained almost without a significant decrease, which can cause the transparent solar cell to bend. In addition, since SiMPF was manufactured using large area processes such as photolithography and dry etching, it can be easily scaled to wafer scale, unlike perovskite and organics, as shown in Figure 19d and 19e. As shown in Figure 20a, the optical diffraction pattern is generated by transmitted light and exhibits Fourier transform properties between the domains. Even after applying 50% strain, a long-range sequence, still representing the cross-domain of the wire array, was still observed, indicating that the form remains without structural disassembly. After PEDOT: PSS was coated on SiMPF prior to IZO deposition, the resistance change of PEDOT: PSS was measured at each strain value at 5% strain intervals during elongation (0 → 50%) and release state (50 → 0%).) (Figure 20b). After 1 cycle of elongation and release, the resistance of PEDOT: PSS coated on SiMPF was restored to its original value. In addition, the resistance change in the 15th cycle is very similar to the value of the first cycle, indicating the durability of the sample. In addition, under the application of 50% strain, the conductivity of the sample is maintained up to ˜700 S / cm, which is still valid and applicable to photovoltaic cells. In addition, these stretching properties of the solid SiMPF are maintained for several cycles of deformation and release (Figure 20c). The scalability of this platform allows applications to scale to sun windows in a unique way. For example, applying strain can increase the pitch simultaneously. Thus, as shown in Figure 21, transparency can be adjusted as a function of deformation, can also be applied to solar windows to control transparency, and depending on the situation, can be used for both privacy and power generation. Applying uniaxial or biaxial strain is a more serious condition for electronics than applying bending strains [85 , 86]. Currently, IZO, which is used as the bottom contact of transparent solar cells, can bend, but not very stretchy. For stretchable solar cells, an EGain (Eutectic Gallium-Indium) – Ag particle electrode was used, which, unlike IZO, indicates that there is no significant change in sheet resistance under strain application (Figure 22). Straining stretches solar cells, but degrades their performance. With strain applied, PEDOT: Reduced conductivity of PSS increases the series resistance of the device, reducing FF and Jsc. However, after one cycle of elongation and release, the photonic parameters are restored due to the elasticity of PEDOT: PSS / n-SiMPF (Figure 23a). In the EQE spectrum of the device with different strains in the wavelength range from 400 to 1100 nm, the integrated Jsc corresponds to the Jsc determined from the J-V curve (Figure 23b). Photovoltaic parameters of stretchable solar cells using EGain-Ag particles as the bottom contact under different strain applications are summarized in Table 7. After 1, 5 and 10 repeated cycles (stretching → release), the performance of stretchable solar cells consisting of PEDOT: PSS / Si microwire-PDMS composites / EGain-Ag particles is maintained without significant degradation (Figure 24a and table 8). Moreover, when each parameter is normalized to the initial value, there are no significant differences in terms of Voc, Jsc, FF and efficiency, indicating that the stretchable solar cell is mechanically durable (Figure 24b).

3.4 Conclusion

We built a standalone SiMPF with adjustable transparency for application to flexible, true color transparent solar cells. A new wet etch was used to transform the shape of the flat upper surface of the SiMPF into an inclined form. Finite difference time domain simulations were used to explain the phenomena that underlie enhanced absorption. This indicates the reabsorption of light by adjacent SiMWs and the enhanced electric field of SiMWs with a slanted form. In addition, neutral color transparent solar cells based on slanted SiMPF showed PCE of 10% to 8.07% of average transmittance. In addition, the platform is based on c-Si wafers that have already been proven and widely used in the Si PV market. In addition, the freestanding platform is manufactured by photolithography and etching processes, which are now widely used in the semiconductor industry, so it can be combined into advanced optics 87, including microcavity and waveguides made by lithography and etching to improve performance. have. Finally, transparent solar cells in this study are ideally suited for practical applications such as integrated solar power, car attachments or the building of the Internet of Things of the Future.

3.5 References

1. Li, D. H. W., Lam, T. N. T. & Cheung, K. L. Energy and cost studies of semi-transparent photovoltaic skylight. *Energy Conversion and Management* **50**, 1981-1990 (2009).

2. Wong, P. W. *et al*. Semi-transparent PV: thermal performance, power generation, daylight modelling and energy saving potential in a residential application. *Renewable Energy* **33**, 1024-1036 (2008).

3. Chang, S. Y. *et al*. Transparent polymer photovoltaics for solar energy harvesting and beyond. *Joule* **2**, 1039-1054 (2018).

4. Guo, C. F. *et al*. Metallic nanostructures for light trapping in energy-harvesting devices. *Light*: *Science & Applications* **3**, e161 (2014).

5. Yuan, L. G. *et al*. Semi-transparent perovskite solar cells: unveiling the trade-off between transparency and efficiency. *Journal of Materials Chemistry A* **6**, 19696-19702 (2018).

6. Husain, A. A. F. *et al*. A review of transparent solar photovoltaic technologies. *Renewable and Sustainable Energy Reviews* **94**, 779-791 (2018).

7. Heo, J. H. *et al*. Semitransparent $FAPbI_{3-x}Br_x$ perovskite solar cells stable under simultaneous damp heat (85 °C/85%) and 1 sun light soaking. *Advanced Materials Technologies* **4**, 1800390 (2019).

8. Heo, J. H. *et al*. Stable semi-transparent $CH_3NH_3PbI_3$ planar sandwich solar cells. *Energy & Environmental Science* **8**, 2922-2927 (2015).

9. Roldán-Carmona, C. *et al*. High efficiency single-junction semitransparent perovskite solar cells. *Energy & Environmental Science* **7**, 2968-2973 (2014).

10. Xue, Q. F. *et al*. Recent advances in semi-transparent polymer and perovskite solar cells for power generating window applications. *Energy & Environmental Science* **11**, 1688-1709 (2018).

11. Han, K. *et al*. Fully solution processed semi-transparent perovskite solar cells with spray-coated silver nanowires/ZnO composite top electrode. *Solar Energy Materials and Solar Cells* **185**, 399-405 (2018).

12. Kim, G. M. & Tatsuma, T. Semi-transparent perovskite solar cells developed by considering human luminosity function. *Scientific Reports* **7**, 10699 (2017).

13. Kim, K. M. *et al*. Work function optimization of vacuum free top-electrode by PEDOT: PSS/PEI interaction for efficient semi-transparent perovskite solar cells. *Solar Energy Materials and Solar Cells* **176**, 435-440 (2018).

14. Tirado, J. *et al*. Low-cost semi-transparent copper sulfide electrode for indium-tin-oxide-free perovskite solar cells. *Thin Solid Films* **662**, 90-96 (2018).

15. Biancardo, M., West, K. & Krebs, F. C. Optimizations of large area quasi-solid-state dye-sensitized solar cells. *Solar Energy Materials and Solar Cells* **90**, 2575-2588 (2006).

16. Zhang, K. *et al*. High-performance, transparent, dye-sensitized solar cells for see-through photovoltaic windows. *Advanced Energy Materials* **4**, 1301966 (2014).

17. Tai, Q. D. *et al*. *In situ* prepared transparent polyaniline electrode and its application in bifacial dye-sensitized solar cells. *ACS Nano* **5**, 3795-3799 (2011).

18. Tagliaferro, R. *et al*. Interplay between transparency and efficiency in dye sensitized solar cells. *Optics Express* **21**, 3235-3242 (2013).

19. Zhang, X. L., Hägglund, C. & Johansson, E. M. J. Highly efficient, transparent and stable semitransparent colloidal quantum dot solar cells: a combined numerical modeling and experimental approach. *Energy & Environmental Science* **10**, 216-224 (2017).

20. Fang, H. H. *et al*. Photoexcitation dynamics in solution-processed formamidinium lead iodide perovskite thin films for solar cell applications. *Light*: *Science & Applications* **5**, e16056 (2016).

21. Zhao, Y. C. *et al*. Quantification of light-enhanced ionic transport in lead iodide perovskite thin films and its solar cell applications. *Light*: *Science & Applications* **6**, e16243 (2017).

22. Kojima, A. *et al*. Organometal halide perovskites as visible-light sensitizers for photovoltaic cells. *Journal of the American Chemical Society* **131**, 6050-6051 (2009).

23. Lee, M. M. *et al*. Efficient hybrid solar cells based on meso-superstructured organometal halide perovskites. *Science* **338**, 643-647 (2012).

24. Gu, L. L. & Fan, Z. Y. Perovskite/organic-semiconductor heterojunctions for ultrasensitive photodetection. *Light*: *Science & Applications* **6**, e17090 (2017).

25. Xie, C. *et al*. Ultrasensitive broadband phototransistors based on perovskite/organic-semiconductor vertical heterojunctions. *Light*: *Science & Applications* **6**, e17023 (2017).

26. Jeon, N. J. *et al*. Solvent engineering for high-performance inorganic-organic hybrid perovskite solar cells. *Nature Materials* **13**, 897-903 (2014).

27. Jeon, N. J. *et al*. Compositional engineering of perovskite materials for high-performance solar cells. *Nature* **517**, 476-480 (2015).

28. Eperon, G. E. *et al*. The importance of moisture in hybrid lead halide perovskite thin film fabrication. *ACS Nano* **9**, 9380-9393 (2015).

29. Della Gaspera, E. *et al*. Ultra-thin high efficiency semitransparent perovskite solar cells. *Nano Energy* **13**, 249-257 (2015).

30. Zhang, M. *et al*. Electrode design to overcome substrate transparency limitations for highly efficient 1 cm^2 mesoscopic perovskite solar cells. *Joule* **2**, 2694-2705 (2018).

31. Jung, J. W., Chueh, C. C. & Jen, A. K. Y. high-performance semitransparent perovskite solar cells with 10% power conversion efficiency and 25% average visible transmittance based on transparent CuSCN as the hole-transporting material. *Advanced Energy Materials* **5**, 1500486 (2015).

32. Cui, Y. *et al*. Efficient semitransparent organic solar cells with tunable color enabled by an ultralow-bandgap nonfullerene acceptor. *Advanced Materials* **29**, 1703080 (2017).

33. Liu, F. *et al*. Efficient semitransparent solar cells with high nir responsiveness enabled by a small-bandgap electron acceptor. *Advanced Materials* **29**, 1606574 (2017).

34. Browning, J. *et al*. Adhesive strength of rubber bonded to Al_2O_3 surfaces: the role of chemistry and morphology. *The Journal of Adhesion* **75**, 229-253 (2001).

35. Tan, S. H. *et al*. Oxygen plasma treatment for reducing hydrophobicity of a sealed polydimethylsiloxane microchannel. *Biomicrofluidics* **4**, 032204 (2010).

36. Tang, K. C. *et al*. Evaluation of bonding between oxygen plasma treated polydimethyl siloxane and passivated silicon. *Journal of Physics*: *Conference Series* **34**, 155-161 (2006).

37. Lee, K. *et al*. 17.6%-Efficient radial junction solar cells using silicon nano/micro hybrid structures. *Nanoscale* **8**, 14473-14479 (2016).

38. Oh, J., Yuan, H. C. & Branz, H. M. An 18.2%-efficient black-silicon solar cell achieved through control of carrier recombination in nanostructures. *Nature Nanotechnology* **7**, 743-748 (2012).

39. Pawlik, M. *et al*. Electrical and chemical studies on Al_2O_3 passivation activation process. *Energy Procedia* **60**, 85-89 (2014).

40. Repo, P. *et al*. Silicon surface passivation by Al_2O_3: effect of ALD reactants. *Energy Procedia* **8**, 681-687 (2011).

41. Simon, D. K. *et al*. Symmetrical Al_2O_3-based passivation layers for *p*- and *n*-type silicon. *Solar Energy Materials and Solar Cells* **131**, 72-76 (2014).

42. Schmidt, J. *et al*. Advances in the surface passivation of silicon solar cells. *Energy Procedia* **15**, 30-39 (2012).

43. Kang, S. B. *et al*. Self-assembled, highly crystalline porous ferroelectric poly(vinylidene fluoride-co-trifluoroethylene) interlayer for Si/organic hybrid solar cells. *Nano Energy* **41**, 243-250 (2017).

44. Kang, S. B. *et al*. Transfer of ultrathin molybdenum disulfide and transparent nanomesh electrode onto silicon for efficient heterojunction solar cells. *Nano Energy* **50**, 649-658 (2018).

45. Chao, Y. C. *et al*. Light scattering by nanostructured anti-reflection coatings. *Energy & Environmental Science* **4**, 3436-3441 (2011).

46. Garnett, E. & Yang, P. D. Light trapping in silicon nanowire solar cells. *Nano Letters* **10**, 1082-1087 (2010).

47. Kibria, M. G. *et al*. Visible light-driven efficient overall water splitting using p-type metal-nitride nanowire arrays. *Nature Communications* **6**, 6797 (2015).

48. Polman, A. & Atwater, H. A. Photonic design principles for ultrahigh-efficiency photovoltaics. *Nature Materials* **11**, 174-177 (2012).

49. Nuzaihan, M. N. M. *et al*. Top-down nanofabrication and characterization of 20 nm silicon nanowires for biosensing applications. *PLoS One* **11**, e0152318 (2016).

50. Seo, K. *et al*. Multicolored vertical silicon nanowires. *Nano Letters* **11**, 1851-1856 (2011).

51. Sun, Y. G. *et al*. Top-down fabrication of semiconductor nanowires with alternating structures along their longitudinal and transverse axes. *Small* **1**, 1052-1057 (2005).

52. Fasoli, A. & Milne, W. I. Overview and status of bottom-up silicon nanowire electronics. *Materials Science in Semiconductor Processing* **15**, 601-614 (2012).

53. Hannon, J. B. *et al*. The influence of the surface migration of gold on the growth of silicon nanowires. *Nature* **440**, 69-71 (2006).

54. Ma, D. D. D. *et al*. Small-diameter silicon nanowire surfaces. *Science* **299**, 1874-1877 (2003).

55. Gunawan, O. & Guha, S. Characteristics of vapor-liquid-solid grown silicon nanowire solar cells. *Solar Energy Materials and Solar Cells* **93**, 1388-1393 (2009).

56. Toor, F. *et al*. Multi-scale surface texture to improve blue response of nanoporous black silicon solar cells. *Applied Physics Letters* **99**, 103501 (2011).

57. Yu, L. W. *et al*. Bismuth-catalyzed and doped silicon nanowires for one-pump-down fabrication of radial junction solar cells. *Nano Letters* **12**, 4153-4158 (2012).

58. Robbins, H. & Schwartz, B. Chemical etching of silicon I. the system HF, HNO_3, and H_2O. *Journal of the Electrochemical Society* **106**, 505-508 (1959).

59. Hamzah, A. A. *et al*. Optimization of HNA etching parameters to produce high aspect ratio solid silicon microneedles. *Journal of Micromechanics and Microengineering* **22**, 095017 (2012).

60. Hamzah, A. A., Majlis, B. Y. & Ahmad, I. HF etching of sacrificial spin-on glass in straight and junctioned microchannels for MEMS microstructure release. *Journal of the Electrochemical Society* **154**, D376-D382 (2007).

61. Lippold, M. *et al*. Etching silicon with $HF\text{-}HNO_3\text{-}H_2SO_4/H_2O$ mixtures - unprecedented formation of trifluorosilane, hexafluorodisiloxane, and Si-F surface groups. *European Journal of Inorganic Chemistry* **2012**, 5714-5721 (2012).

62. Roman, P. *et al*. Current advances in anhydrous hf/organic solvent processing of semiconductor surfaces. *Solid State Phenomena* **145-146**, 231-234 (2009).

63. Tarakanova, E. G. & Yukhnevich, G. V. Composition and structure of heteroassociates formed in the HF-*N*, *N* dimethylformamide binary liquid system. *Russian Chemical Bulletin* **60**, 81-88 (2011).

64. El Gawhary, O., Severini, S. & Christillin, P. Which group velocity of light in a dispersive medium? *The European Physical Journal Plus* **126**, 1-5 (2011).

65. Kosten, E. D., Warren, E. L. & Atwater, H. A. Ray optical light trapping in silicon microwires: exceeding the $2n^2$ intensity limit. *Optics Express* **19**, 3316-3331 (2011).

66. Putnam, M. C. *et al*. Si microwire-array solar cells. *Energy & Environmental Science* **3**, 1037-1041 (2010).

67. Sai, H. *et al*. Light trapping effect of submicron surface textures in crystalline Si solar cells. *Progress in Photovoltaics* **15**, 415-423 (2007).

68. Zhao, J. H., Wang, A. H. & Green, M. A. 24·5% efficiency silicon PERT cells on MCZ substrates and 24·7% efficiency PERL cells on FZ substrates. *Progress in Photovoltaics* **7**, 471-474 (1999).

69. Hu, L. & Chen, G. Analysis of optical absorption in silicon nanowire arrays for photovoltaic applications. *Nano Letters* **7**, 3249-3252 (2007).

70. Preston, C. *et al*. Silver nanowire transparent conducting paper-based electrode with high optical haze. *Journal of Materials Chemistry C* **2**, 1248-1254 (2014).

71. Galeotti, F. *et al*. Tailorable perylene-loaded fluorescent nanostructures: a multifaceted approach enabling their application in white hybrid LEDs. *Journal of Materials Chemistry C* **4**, 5407-5415 (2016).

72. Araki, T. *et al*. Low haze transparent electrodes and highly conducting air dried films with ultra-long silver nanowires synthesized by one-step polyol method. *Nano Research* **7**, 236-245 (2014).

73. Niu, Z. Q. *et al*. Synthesis of silver nanowires with reduced diameters using benzoin-derived radicals to make transparent conductors with high transparency and low haze. *Nano Letters* **18**, 5329-5334 (2018).

74. Xu, Q. S. *et al*. Flexible transparent conductive films on PET substrates with an AZO/AgNW/AZO sandwich structure. *Journal of Materials Chemistry C* **2**, 3750-3755 (2014).

75. Gao, S. *et al*. Multifunctional Zn(II)/Cd(II) metal complexes for tunable luminescence properties and highly efficient dye-sensitized solar cells. *RSC Advances* **5**, 43705-43716 (2015).

76. Gao, S. *et al*. An insight into the controllable synthesis of Cd(ii) complexes with a new multifunctional ligand and its application in dye-sensitized solar cells and luminescence properties. *Journal of Materials Chemistry A* **3**, 6053-6063 (2015).

77. Zhang, J. W. *et al*. Highly efficient semitransparent organic solar cells with color rendering index approaching 100. *Advanced Materials* **31**, 1807159 (2019).

78. Chueh, C. C. *et al*. Toward high-performance semi-transparent polymer solar cells: optimization of ultra-thin light absorbing layer and transparent cathode architecture. *Advanced Energy Materials* **3**, 417-423 (2013).

79. Song, Y. *et al*. Visibly-transparent organic solar cells on flexible substrates with all-graphene electrodes. *Advanced Energy Materials* **6**, 1600847 (2016).

80. Eperon, G. E. *et al*. Neutral color semitransparent microstructured perovskite solar cells. *ACS Nano* **8**, 591-598 (2014).

81. Wook Lim, J. *et al*. Highly transparent amorphous silicon solar cells fabricated using thin absorber and high-bandgap-energy n/i-interface layers. *Solar Energy Materials and Solar Cells* **128**, 301-306 (2014).

82. Kang, S. B. *et al*. Enhanced piezoresponse of highly aligned electrospun poly(vinylidene fluoride) nanofibers. *Nanotechnology* **28**, 395402 (2017).

83. Yang, B. *et al*. Nature degradable, flexible, and transparent conductive substrates from green and earth-abundant materials. *Scientific Reports* **7**, 4936 (2017).

84. Yang, R. S. *et al*. Power generation with laterally packaged piezoelectric fine wires. *Nature Nanotechnology* **4**, 34-39 (2009).

85. van den Brand, J. *et al*. Flexible and stretchable electronics for wearable health devices. *Solid-State Electron* **113**, 116-120 (2015).

86. Wu, W. Stretchable electronics: functional materials, fabrication strategies and applications. *Science and Technology of Advanced Materials* **20**, 187-224 (2019).

87. Liu, S. *et al*. End-fire injection of light into high-*Q* silicon microdisks. *Optica* **5**, 612-616 (2018).

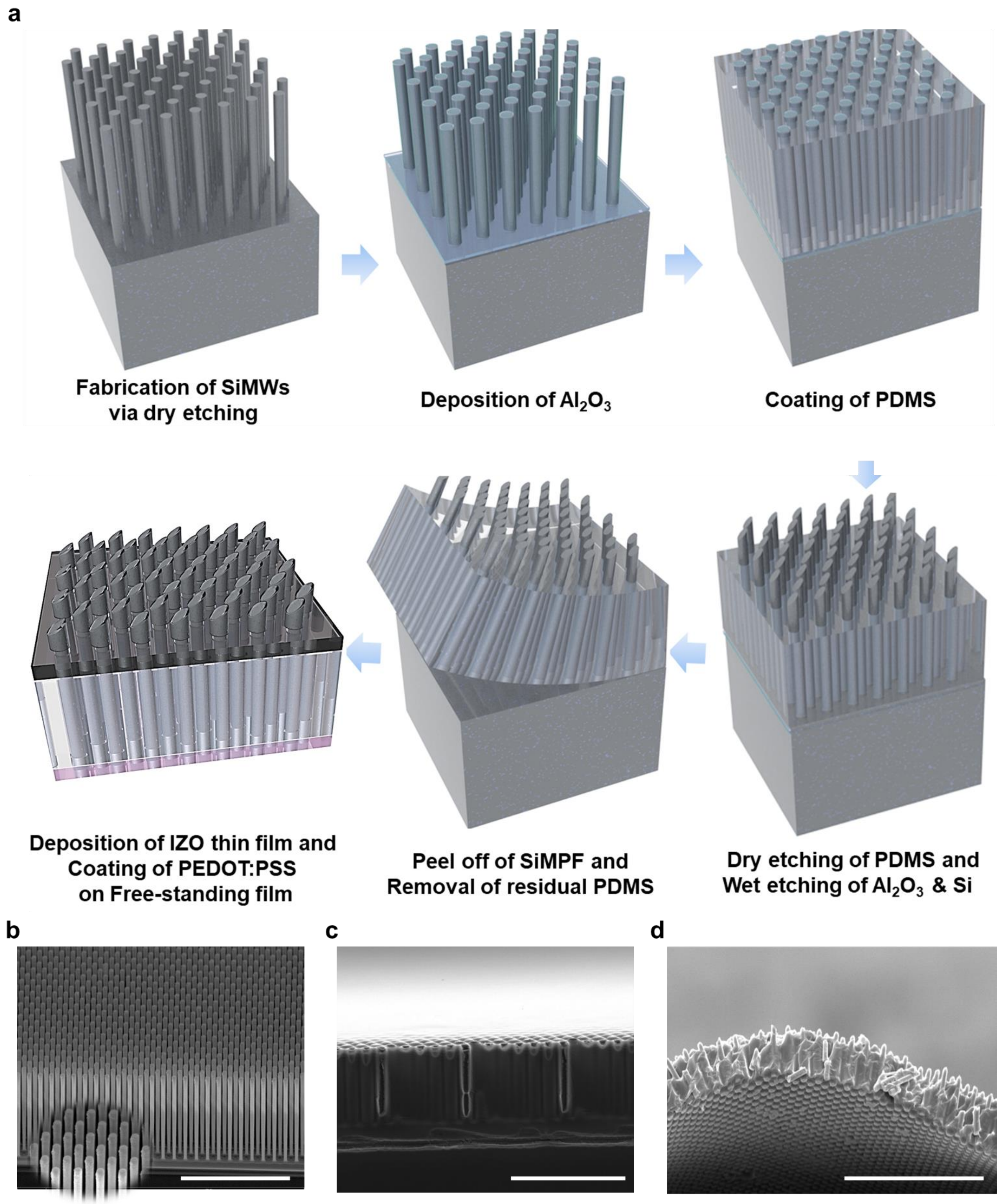

Figure 1. Experimental procedure of large-area SiMPF composite. (a) Schematic of fabrication process. SEM images of (b) Si microwire arrays in a bird's-eye view (scale bar: 50 μm), (c) Si microwire array filled with PDMS after surface treatment (scale bar: 50 μm) and (d) Free standing SiMPF after peeling off from the Si parent (scale bar: 100 μm)

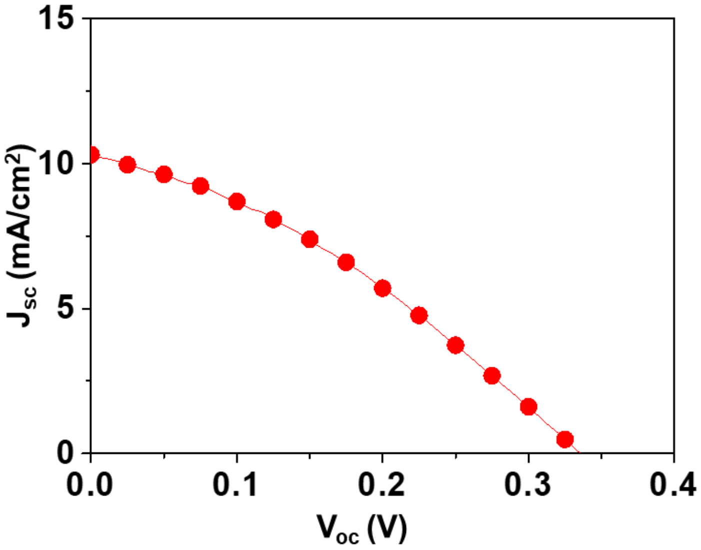

Figure 2. J-V characteristics of the transparent solar cells without Al_2O_3 passivation.

	V_{oc} (V)	J_{sc} (mA/cm^2)	FF	Eff. (%)
W/O Al_2O_3 passivation	0.33	10.7	0.327	**1.08**

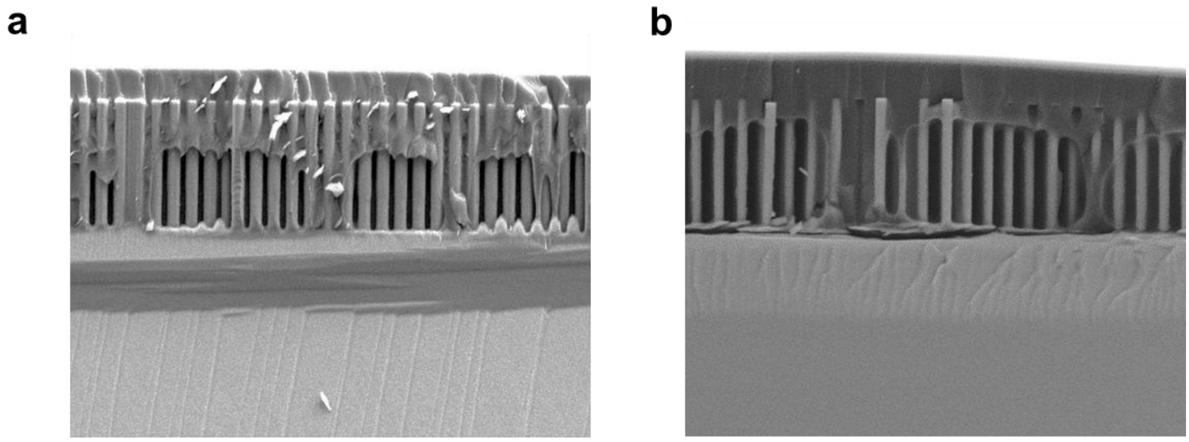

Figure 3. (a,b) Cross sectional SEM images of Si microwire arrays filled with PDMS before the surface treatment

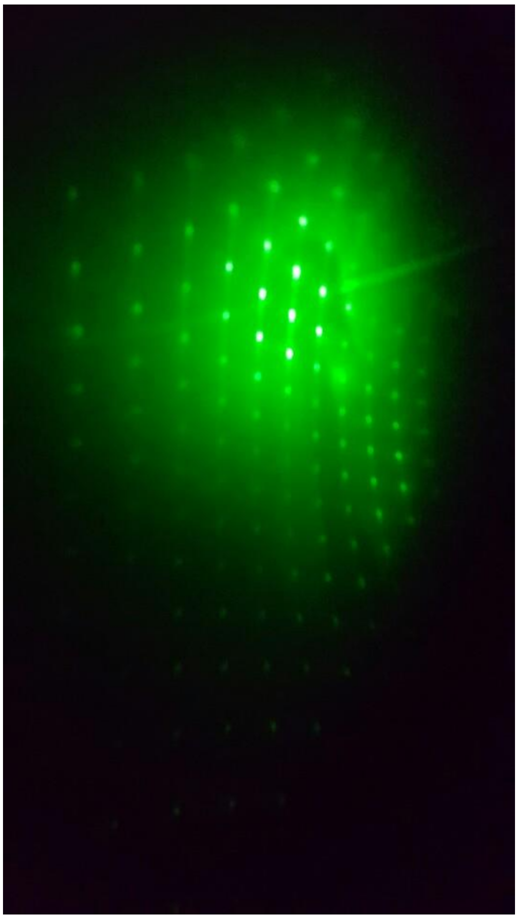

Figure 4. Optical diffraction pattern produced by transmitted light (λ = 532 nm), demonstrating the long-range order of the wires.

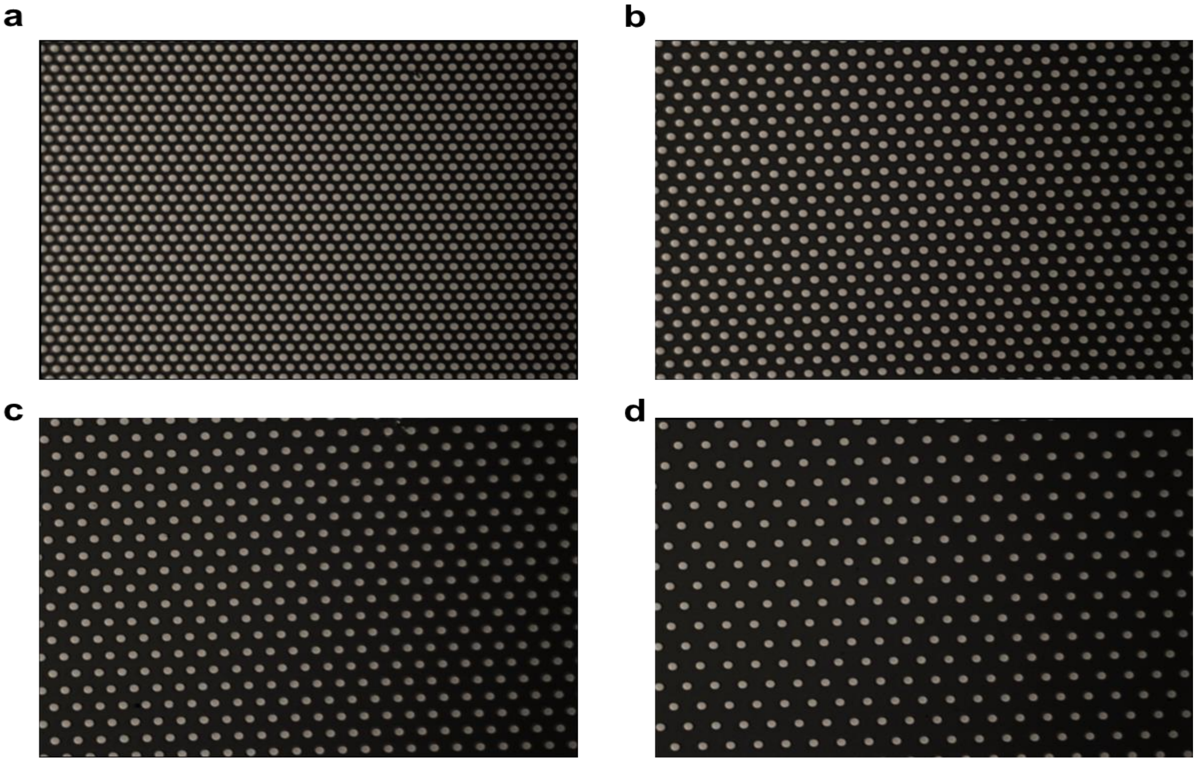

Figure 5. SEM images of Si microwire arrays; pitch of (a) 4 μm pitch, (b) 5 μm, (c) 6 μm and (d) 7 μm.

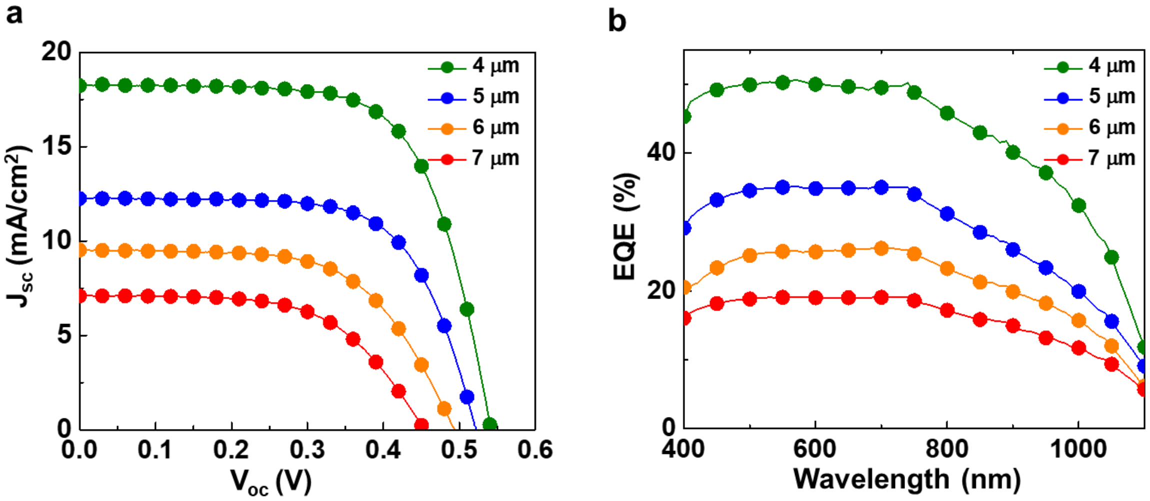

Figure 6. Photovoltaic performances of TSCs based on flat SiMPFs (a) J-V characteristics and (b) EQE of the transparent solar cells with controlled pitches.

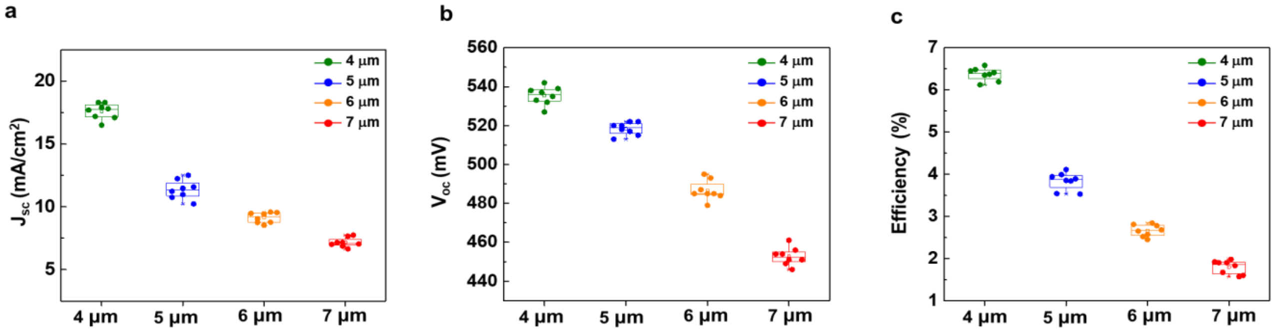

Figure 7. Box plots (minimum–maximum, 25–75%, mean: open square symbol, median: solid line) of photovoltaic parameters: (a) short circuit current, (b) open circuit voltage and (c) efficiency of flat-tip of SiMPF-based solar cells.

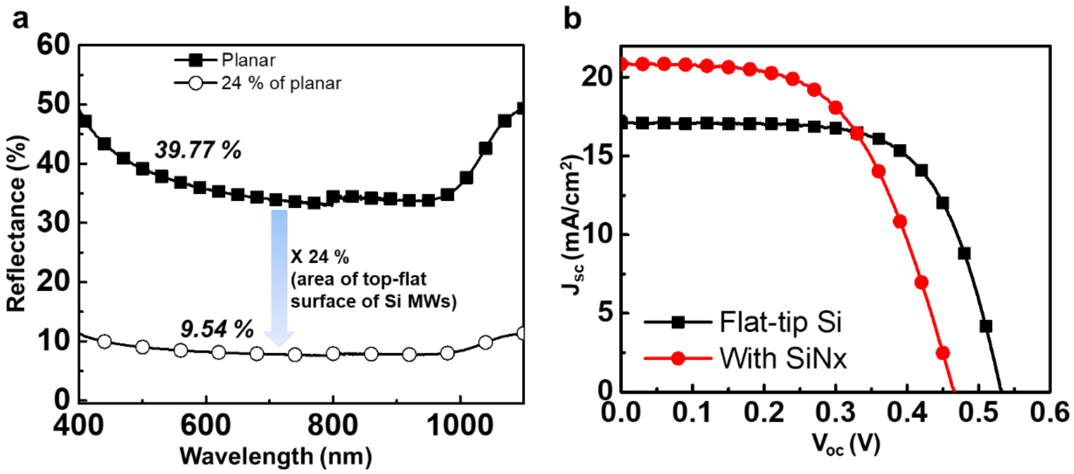

	V_{oc} (V)	J_{sc} (mA/cm^2)	FF	Eff. (%)
Flat tip Si	0.533	17.07	0.658	**5.99**
With SiNx on the tip	0.466	18.94	0.534	**4.71**

Figure 8. (a) The experimental and calculated reflectance spectra of planar Si (black square and 24 % of planar Si (black circle, calculated). (b) J-V characteristic of the TSC based on the 4 μm-pitched SiMW array with (black line) and without SiNx (red line).

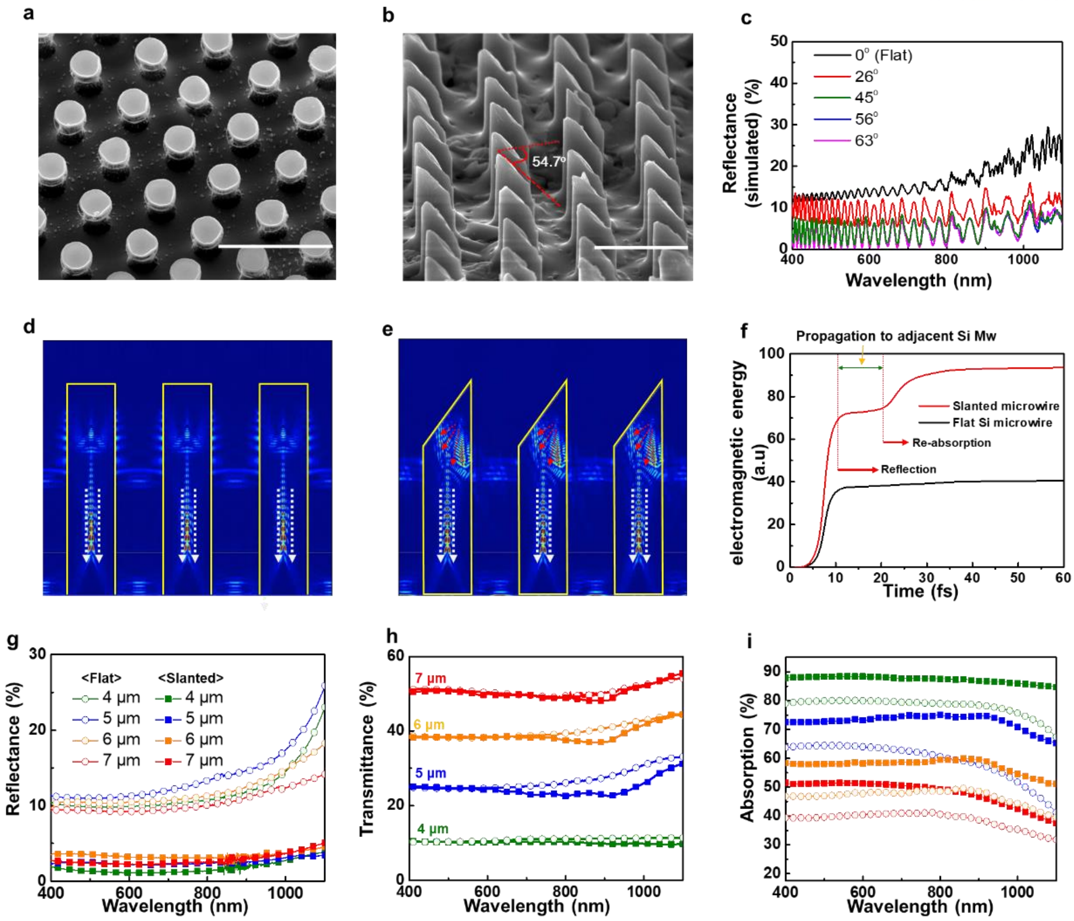

Figure 9. Enhancing the light absorption of SiMPF by etching. (a) SEM image of flat SiMPF without etching (scale bar: 10 μm). (b) Slanted SiMPF with etching by HNAD solution having a HF: HNO$_3$: CH$_3$COOH: DMF volume ratio of 3:6:0.3:0.7 (scale bar: 5 μm). (c) Simulated reflectance of SiMPF with difference angle of etched surface. The electric field intensity in the (d) flat and (e) slanted SiMPF. (f) The total amount of electromagnetic energy in a single flat SiMPF (black solid line) and slanted SiMPF (red solid line). (g) Transmittance spectra of the slatned SiMPF of different center-to-center distance between microwires. (h) Reflectance spectra of the flat (circle dot) and slanted SiMPF (square dot) as a function of wavelength (i) The total amount of absorption in slanted SiMPF : 4 μm (green line), 5 μm (blue line), 6 μm (yellow line) and 7 μm (red line) .

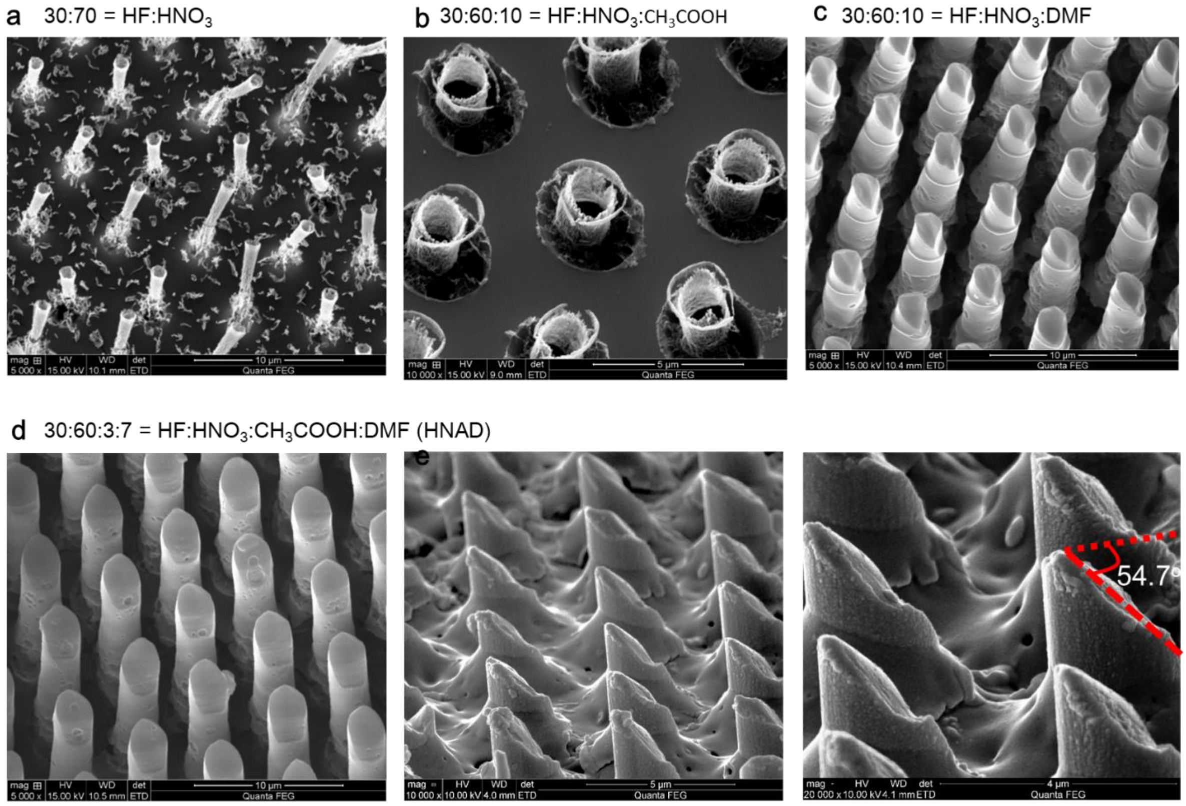

Figure 10. SEM images showing (a) the dislodged Si microwire from the PDMS due to aggressive $HF:HNO_3$ (3:7) etching, (b) Etched Si microwire by the 3:6:1 ($HF:HNO_3:CH_3COOH$) solution and (c) by 3:6:1 ($HF:HNO_3$:DMF) solution. (d) Slanted Si microwire by the solution of having a HF: HNO_3: CH_3COOH: DMF volume ratio of 3:6:0.3:0.7.

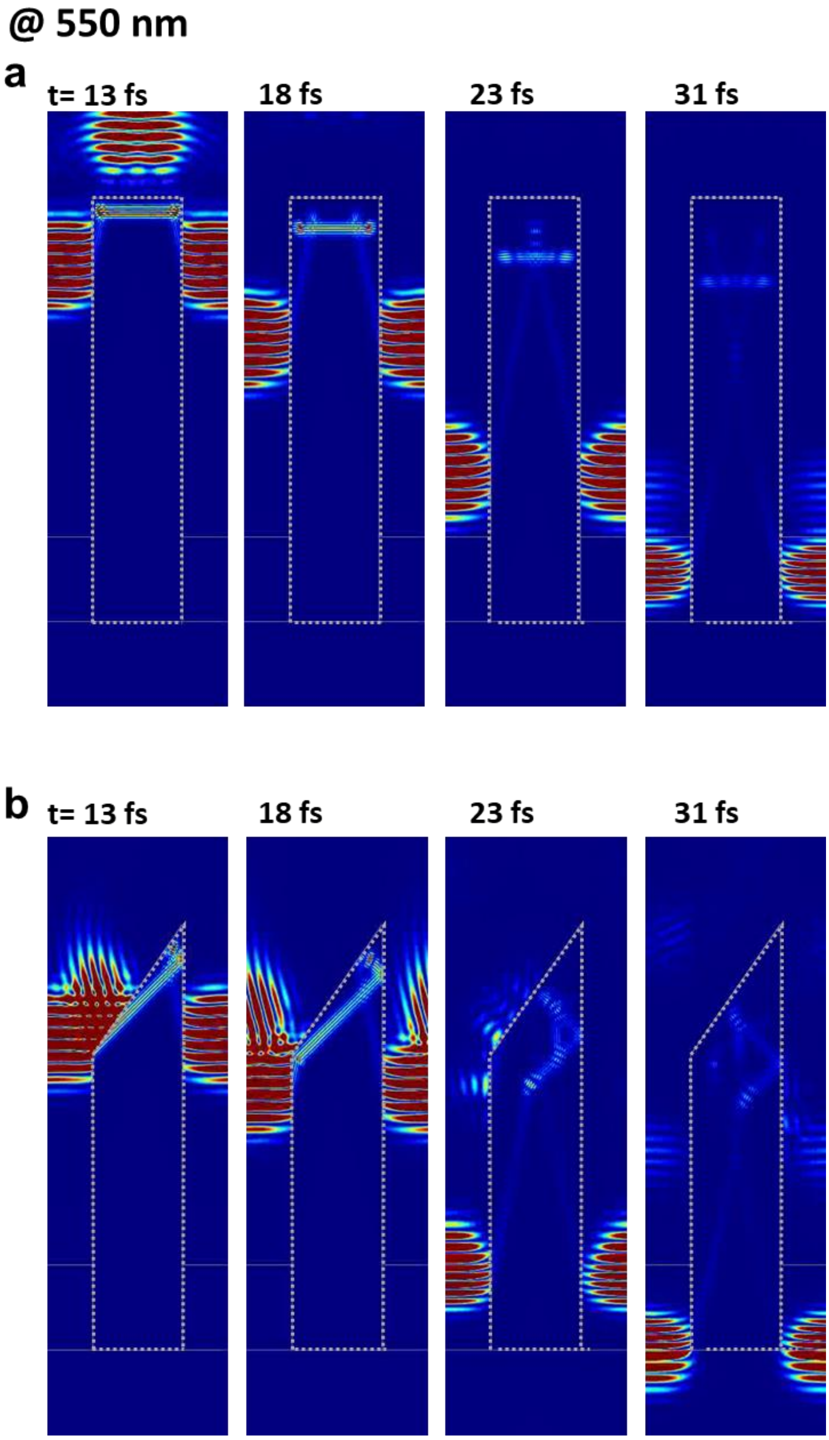

Figure 11. Time resolved light-tracing simulation with wavelength of 550 nm at (a) flat and (b) slanted Si microwire.

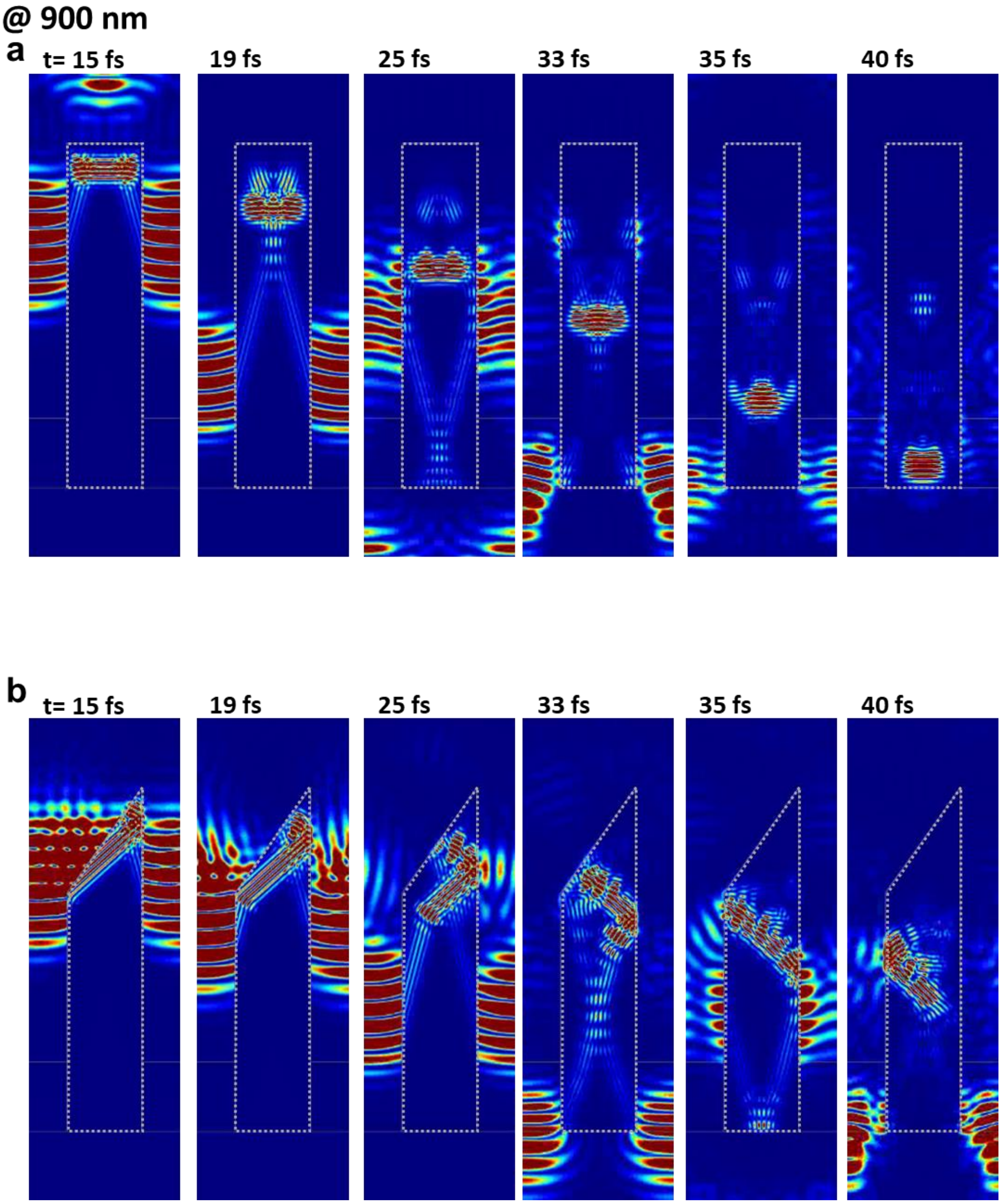

Figure 12. Time resolved light-tracing simulation with wavelength of 900 nm at (a) flat and (b) slanted Si microwire.

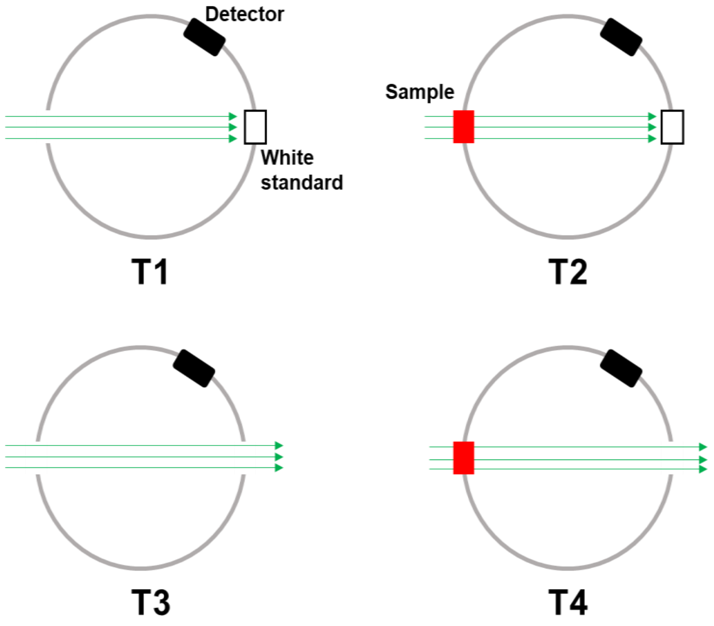

Figure 13. The configurations to measure the haze ratio.

For each samples, the hazeness is calculated by four scans using the configuration as shown in Fig. Sxx. The haze value is defined as the ratio of T_{diffuse} (diffuse transmittance) T_{total} (total transmittance). At the configuration T1, transmittance is measured when integrating sphere is closed with white standard, while in configuration T2 additionally a sample is placed at the entrance to the sphere. In configuration T3 light can pass through the sphere undisturbed and in configuration T4 it is scattered by the sample at the entrance to the sphere The T1 and T3 are the corrections for the experimental setup. Moreover, T2 is total forward scattered illumination and T4 is total transmitted illumination, respectively. Therefore, the The haze (%) is $\mathrm{T}_{\mathrm{diffuse}}$ / $\mathrm{T}_{\mathrm{total}}$ where $\mathrm{T}_{\mathrm{diffuse}} = [(\mathrm{T4} - \mathrm{T3}*(\mathrm{T2}/\mathrm{T1}))]/\mathrm{T1}$ and $\mathrm{T}_{\mathrm{total}} = \mathrm{T2}/\mathrm{T1}$.

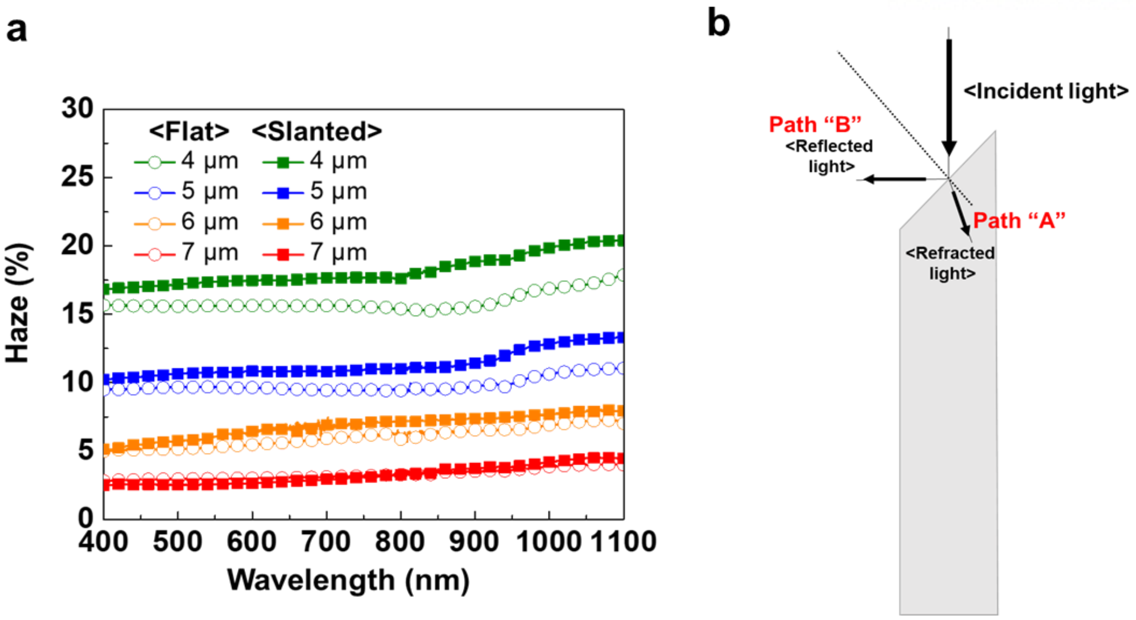

Figure 14. (a) The haze of the SiMPF with flat (circle dot) and slanted (square dot) tip as a function of wavelength: 4 μm (green line), 5 μm (blue line), 6 μm (yellow line) and 7 μm (red line). (a) Schematic illustration of refracted and reflected light at the slanted microwire

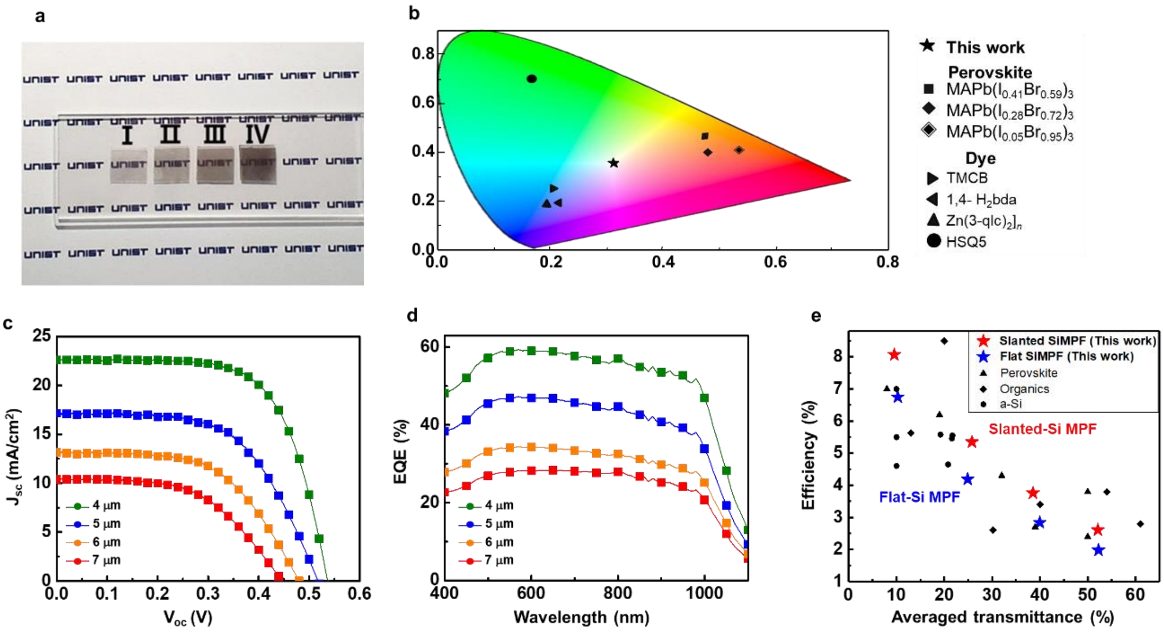

Figure 15. Performance of Transparent solar cells based on the slanted SiMPF

(a) Optical images of freestadning slanted SiMPF. (b) The representation of the color coordinates of slanted SiMPF (★, This work), halide perovskites (◆,■, and ◈) and dyes

(►,◄,▲, and ●) with AM1.5G illumination on the CIE chromaticity diagram. (c) J-V characteristics and (d) EQE of slanted SiMPF based the transparent solar cells: 4 μm (green line), 5 μm (blue line), 6 μm (yellow line) and 7 μm (red line). (e) The comparisons with previous reported neutral color transparent solar cells based on halide perovskite, dye, a- Si, and organics.

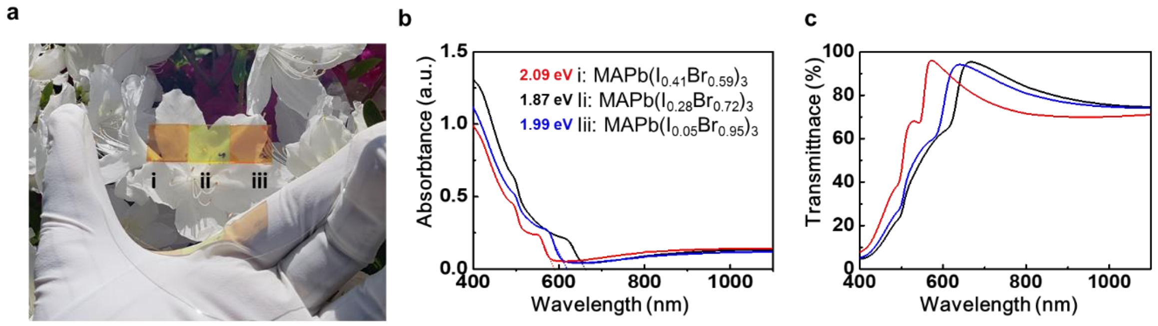

Figure 16. (a) Optical images of perovskite filters: i) $MAPb(I_{0.41}Br_{0.59})_3$, ii) $MAPb(I_{0.28}Br_{0.72})_3$ and iii) $MAPb(I_{0.05}Br_{0.95})_3$ (b) absorbance and (c) transmittance spectra of various perovskite filters

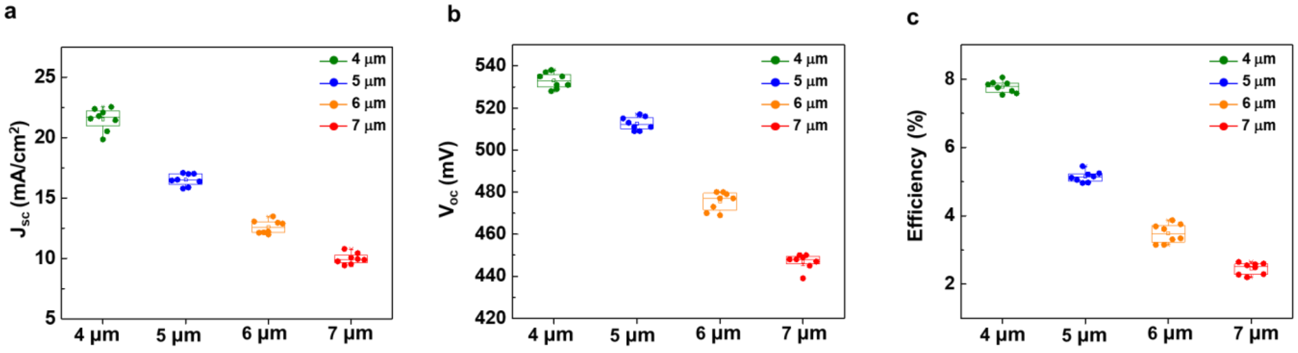

Figure 17. Box plots (minimum–maximum, 25–75%, mean: open square symbol, median: solid line) of photovoltaic parameters: (a) short circuit current, (b) open circuit voltage and (c) efficiency of slanted-tip of SiMPF-based solar cells.

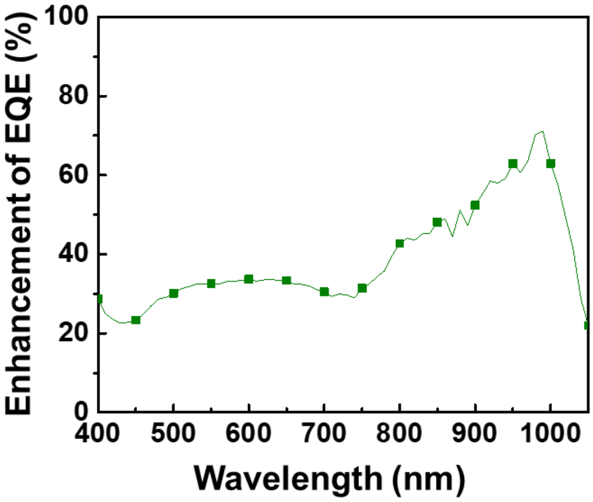

Figure 18. The averaged EQE enhancement of slanted SiMPF based devices as function of wavelength.

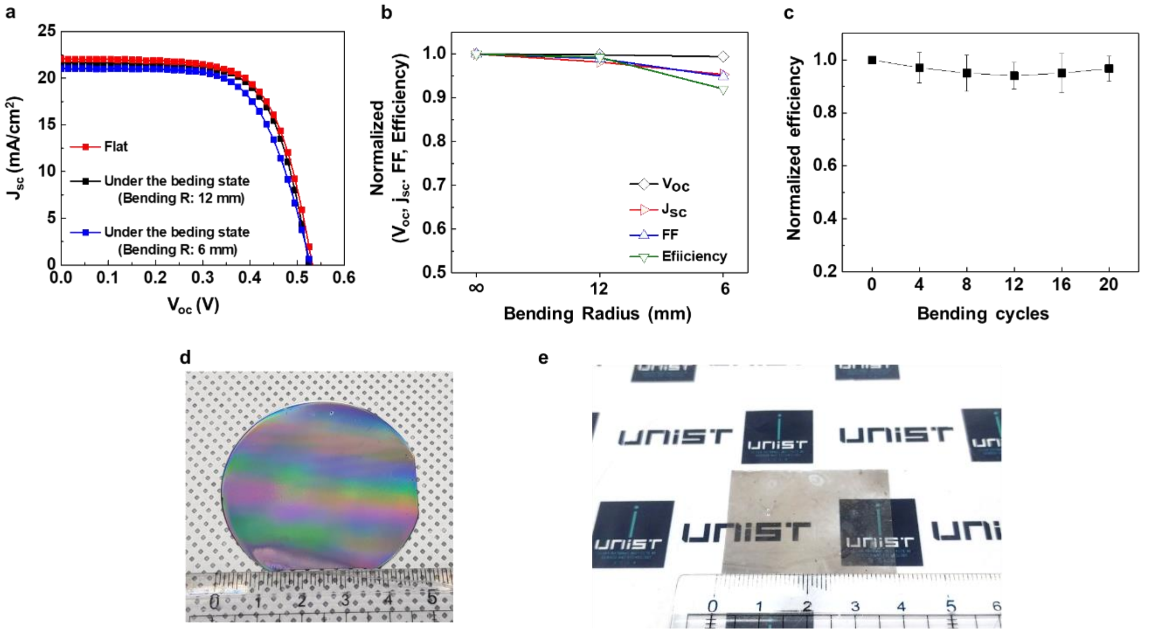

Figure 19. **Flexibility of transparent solar cell and Large scalability of free-standing SiMPF** (a) Light J-V curves and (b) normalized photovoltaic parameters of transparent solar cells under the bending state with the different bending radius. (c) Normalized efficiency of the transparent solar cells after cyclic bending test. Photographic images of (d) Si Mw arrays on 2-inch wafer, and (e) Free-standing SiMPF peeled from the (d).

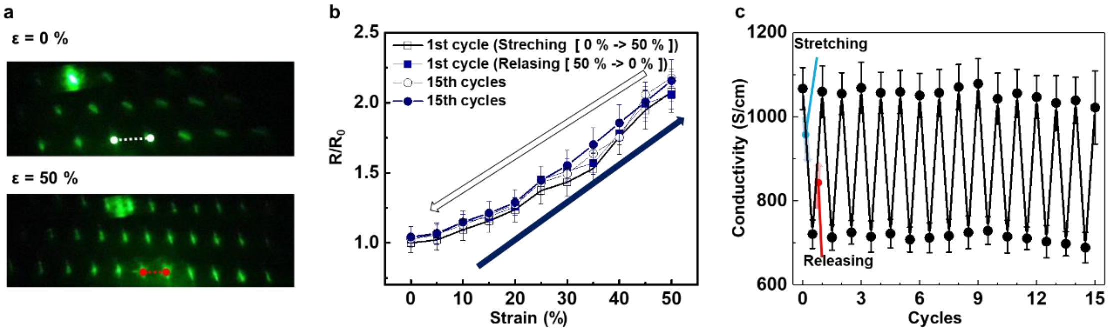

Figure 20 Stretchablity of free-standing SiMPF. (a) Optical diffraction pattern of the SiMPF at ε = 0 % and 50 %. (b) The changes in resistances at each strain values as the 5 % strain interval during stretching (0 → 50 %) and releasing state (50 → 0 %) at 1 cycle and 15 cycles. (c) Changes in conductivity when the applied strain is 0 % and 50 % under repetition of stretching and releasing cycles.

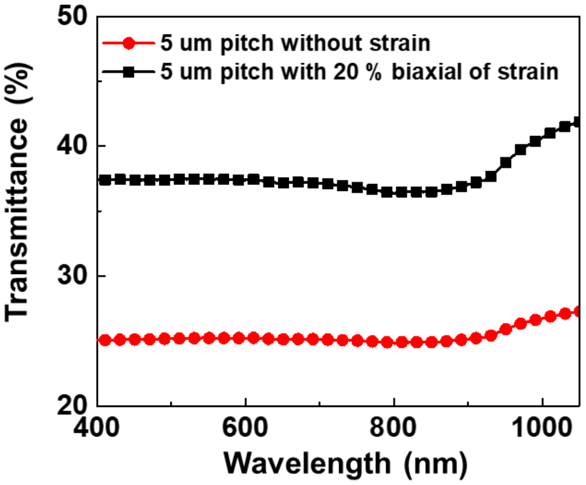

Figure 21. The transmittance spectra of the sample with 5 um pitch without (red line) and with strain (black line).

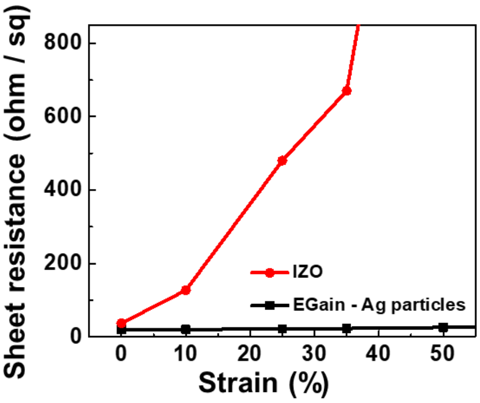

Figure 22. Sheet resistance versus strain of IZO (red line) and EGain-Ag particles electrodes (black line) on PDMS subjected to uniaxial strain.

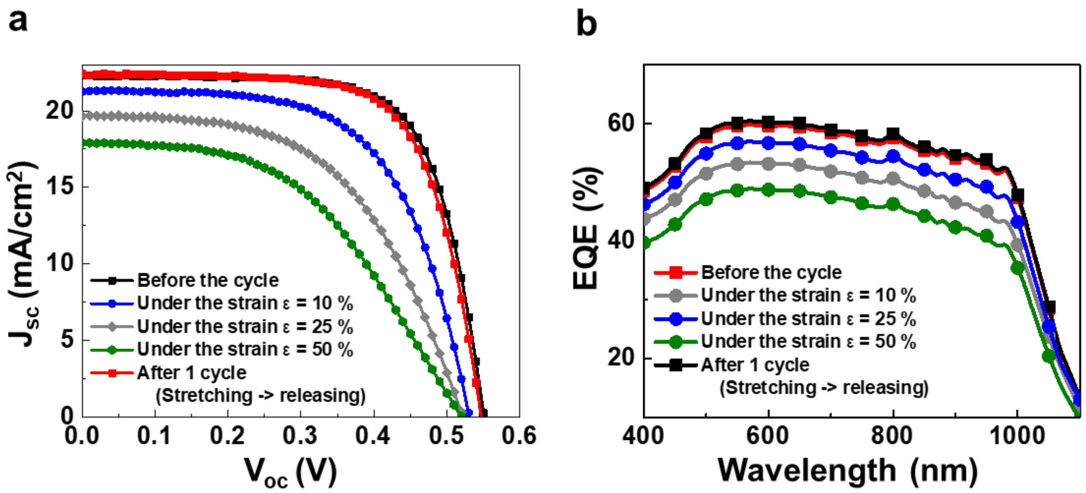

Figure 23. (a) Light J-V curves and (b) corresponded external quantum efficiency of stretchable solar cells under the different strain.

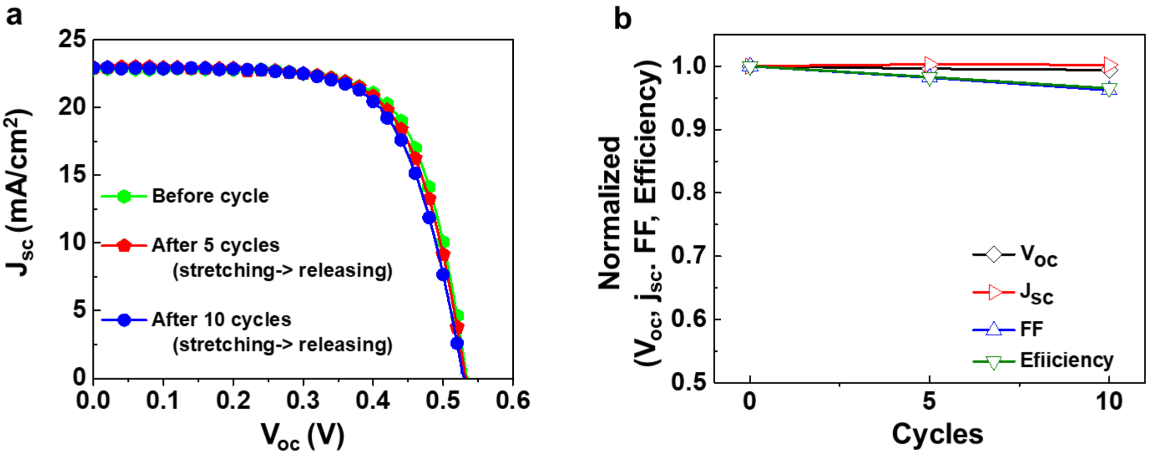

Figure 24. (a) Light J-V curves and (b) Normalized photovoltaic parameters of stretchable solar cells before and after 5 and 10 cycles.

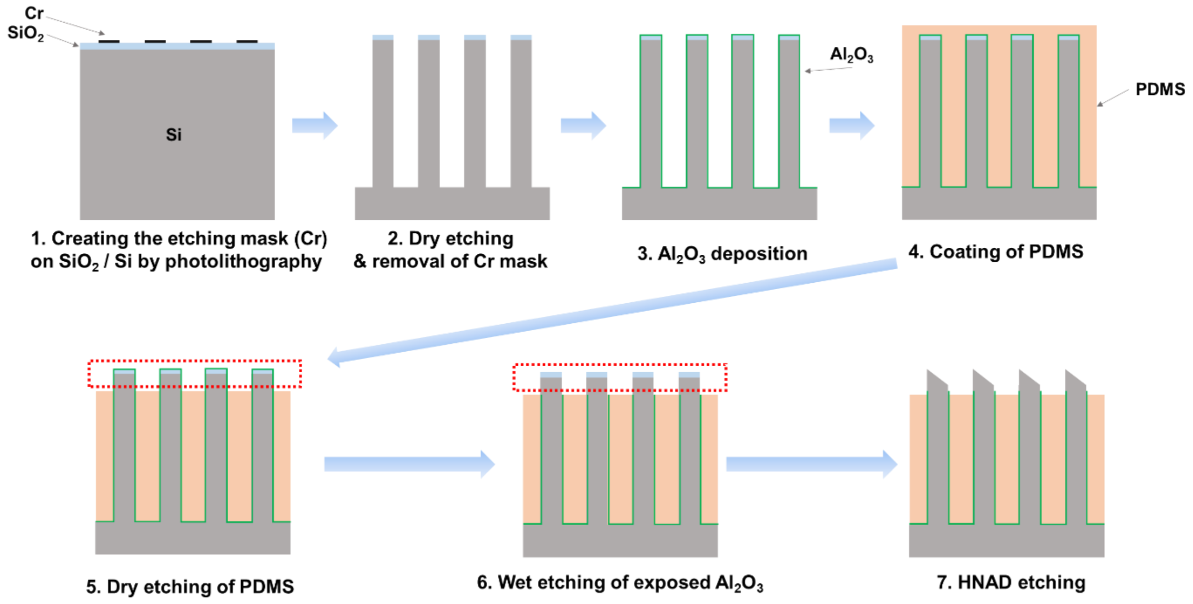

Figure 25. Overall etching process to fabricate the slanted-tip of Si microwire – PDMS composite film.

Table 1. Average photovoltaic performance of flat SiMPF based transparent solar cells[a] and champion device with controlled spacing between microwires. [a]Average performance for 8 devices.

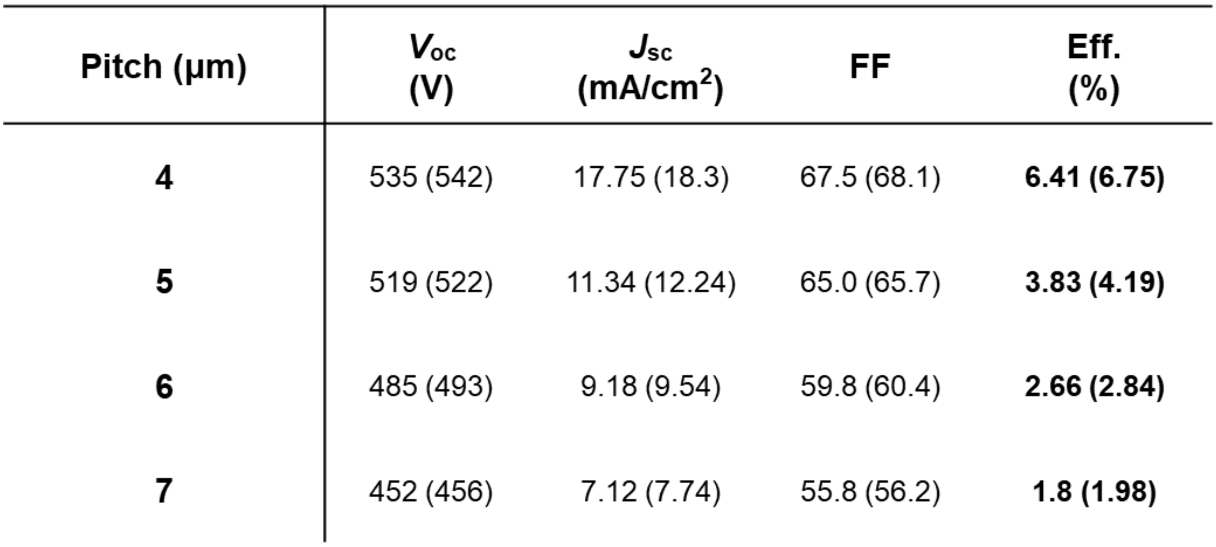

Pitch (μm)	V_{oc} (V)	J_{sc} (mA/cm^2)	FF	Eff. (%)
4	535 (542)	17.75 (18.3)	67.5 (68.1)	**6.41 (6.75)**
5	519 (522)	11.34 (12.24)	65.0 (65.7)	**3.83 (4.19)**
6	485 (493)	9.18 (9.54)	59.8 (60.4)	**2.66 (2.84)**
7	452 (456)	7.12 (7.74)	55.8 (56.2)	**1.8 (1.98)**

Table 2. Optical properties (reflectance, transmittance) of flat SiMPF.

Flat

Averaged reflectance

Pitch (μm)	4	5	6	7
Visible + NIR (400 ~ 1100 nm)	11.84	13.90	12.02	10.48
Visible (400 ~ 800 nm)	10.10	11.60	10.57	9.44
Near-IR (800 ~ 1100 nm)	14.22	17.05	14.01	11.90

Averaged transmittance

Pitch (μm)	4	5	6	7
Visible + NIR (400 ~ 1100 nm)	10.05	26.85	39.95	50.81
Visible (400 ~ 800 nm)	10.23	24.95	38.53	50.28
Near-IR (800 ~ 1100 nm)	9.80	29.46	41.89	51.52

Averaged absorbance

Pitch (μm)	4	5	6	7
Visible + NIR (400 ~ 1100 nm)	78.11	59.24	48.03	38.71
Visible (400 ~ 800 nm)	79.66	63.45	50.90	40.28
Near-IR (800 ~ 1100 nm)	75.98	53.49	44.10	36.58

Table 3. Optical properties (reflectance, transmittance) of slanted SiMPF

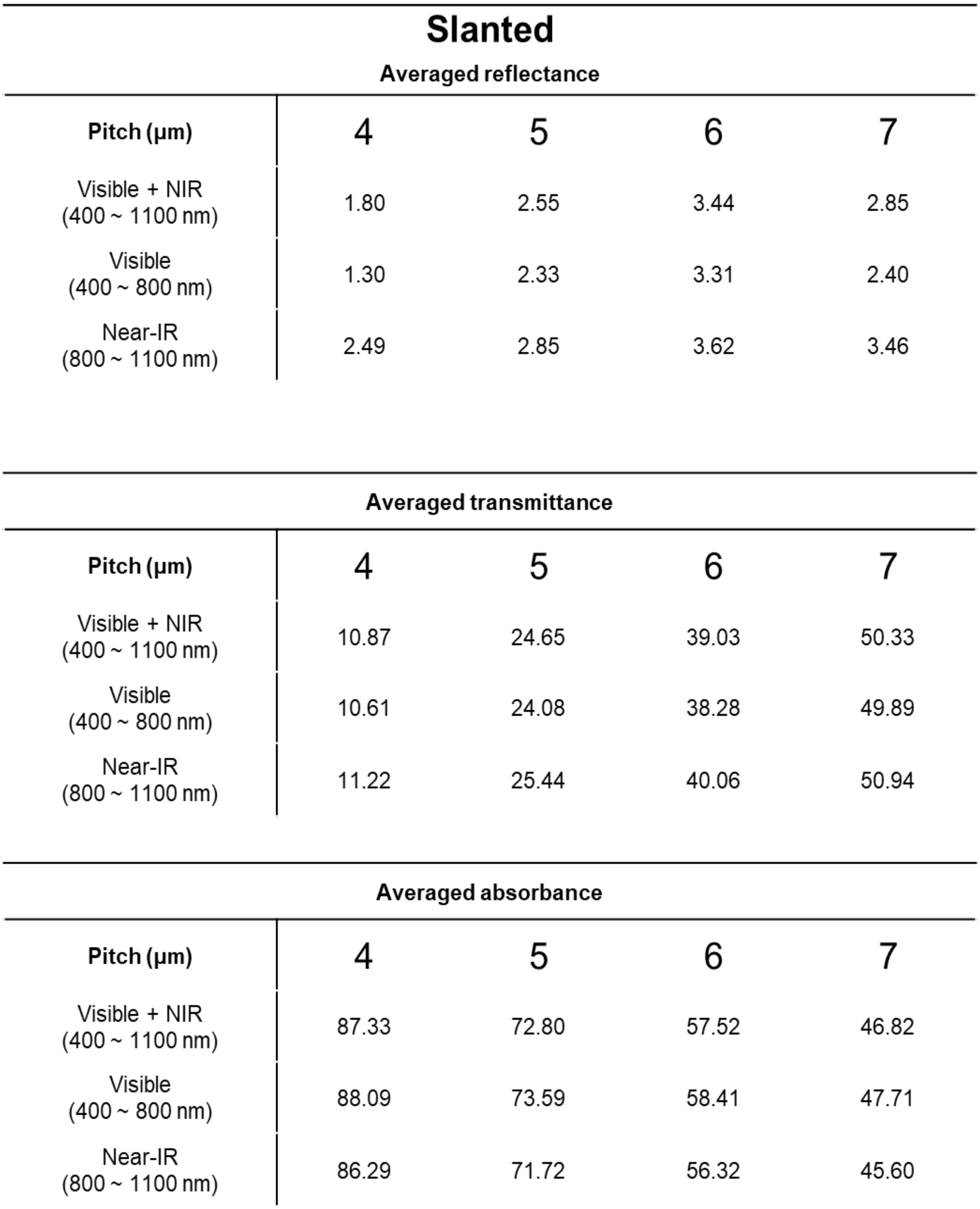

Slanted

Averaged reflectance

Pitch (μm)	4	5	6	7
Visible + NIR (400 ~ 1100 nm)	1.80	2.55	3.44	2.85
Visible (400 ~ 800 nm)	1.30	2.33	3.31	2.40
Near-IR (800 ~ 1100 nm)	2.49	2.85	3.62	3.46

Averaged transmittance

Pitch (μm)	4	5	6	7
Visible + NIR (400 ~ 1100 nm)	10.87	24.65	39.03	50.33
Visible (400 ~ 800 nm)	10.61	24.08	38.28	49.89
Near-IR (800 ~ 1100 nm)	11.22	25.44	40.06	50.94

Averaged absorbance

Pitch (μm)	4	5	6	7
Visible + NIR (400 ~ 1100 nm)	87.33	72.80	57.52	46.82
Visible (400 ~ 800 nm)	88.09	73.59	58.41	47.71
Near-IR (800 ~ 1100 nm)	86.29	71.72	56.32	45.60

Table 4. The color coordinates of dye, perovskite and SiMPF represented in the CIE 1931 chromaticity diagram

Materials		*Color*	*CIE* 1931		Ref
			x	y	
Dye	HSQ5	Green	0.68	0.19	
	TMCB	Blue	0.21	0.20	
	1,4- H_2bda	Blue	0.19	0.21	
	Zn(3-qlc)$_2$]$_n$	Blue	0.19	0.17	
Perovskites	$MAPb(I_{0.05}Br_{0.95})_3$	Brown	0.53	0.42	
	$MAPb(I_{0.28}Br_{0.72})_3$	Brown	0.47	0.40	
	$MAPb(I_{0.41}Br_{0.59})_3$	Yellow	0.46	0.47	
SiMPF		**Gray (neutral)**	0.34	0.34	

Table 5. Average photovoltaic performance of slanted SiMPF based transparent solar cells[a] and champion device with controlled spacing between microwires. [a]Average performance for 8 devices.

Pitch (μm)	**V_{oc} (V)**	**J_{sc} (mA/cm^2)**	**FF**	**Eff. (%)**
4	533 (537)	21.84 (22.54)	66.1 (66.7)	**7.70 (8.07)**
5	511 (516)	16.77 (17.08)	60.1 (60.8)	**5.15 (5.35)**
6	476 (479)	12.81 (13.47)	57.3 (58.2)	**3.49 (3.75)**
7	445 (450)	9.98 (10.43)	54.6 (55.7)	**2.42 (2.61)**

Table 6. The photovoltaic parameters of transparent solar cells under the bending state with different bending radius.

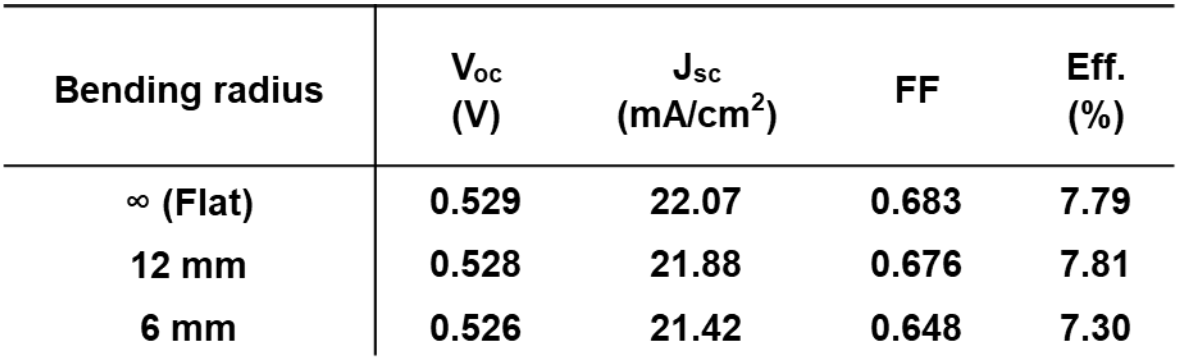

Bending radius	V_{oc} (V)	J_{sc} (mA/cm^2)	FF	Eff. (%)
∞ (Flat)	0.529	22.07	0.683	7.79
12 mm	0.528	21.88	0.676	7.81
6 mm	0.526	21.42	0.648	7.30

Table 7. The photovoltaic parameters of stretchable solar cells taking advantages of EGain – Ag particles as bottom contact under the application of different strain.

Applied strain	V_{oc} **(V)**	J_{sc} **(mA/cm^2)**	**FF**	**Eff. (%)**
ε = 0 % (Before the cycle)	0.537	22.289	0.698	**8.360**
Under the ε = 10 %	0.531	21.258	0.614	**6.933**
Under the ε = 25 %	0.522	19.641	0.538	**5.520**
Under the ε = 50 %	0.520	17.916	0.483	**4.497**
ε = 0 % After 1 cycle (Stretching -> Releasing)	0.533	22.381	0.686	**8.179**

Table 8. The photovoltaic parameters of stretchable solar cells taking advantages of EGain – Ag particles as bottom contact after repeated stretching – releasing cycles.

	V_{oc} (V)	J_{sc} (mA/cm^2)	FF	Eff. (%)
Before cycle	0.534	22.86	0.697	**8.51**
After 5 cycles	0.532	22.94	0.685	**8.37**
After 10 cycles	0.531	22.92	0.673	**8.19**

CHAPTER 4. Si / P(VDF-TrFE) hetero-interface for interlayer in solar cells

4.1 Research background

Ferroelectric materials with organics like poly(Vinylidene fluoride) (PVDF) and trifluoroethylene (P(VDF-TrFE)) are usually utilized for production of ferroelectric field-effect transistor and piezoelectric energy harvester, separators of battery. Filtration equipment, etc [1-11] On the other hand, to gain best efficiency in their applied area, these ferroelectric materials must show a certain morphology and characteristics, e.g., be processible in thin films free of pinhole for usage in ferroelectric transistors and nonvolatile memories to avoid electrical shorts [12]. Kang et al. added poly (methylmethylmethyl methate) as an additive efficiently delayed the fast crystallization of the PVDF during quenching and thereby set ferroelectric thin films[13]. In contrast, poly(Vinylidene fluoride) nanofibers have been found to be more suitable for manufacturing piezoelectric energy harvesting devices than thin films that can accept larger stress and thus afford improved piezoelectric power [14-16]. In recent years, improvements in solar cell efficiency have been widely tried by integrating the PVDF and its co-polymers into interlays. This approach demands ferroelectric materials with organics to show a distinctive porous thin film structure, because the pair of photogenic electron holes must be carried through the holes of insulated ferroelectric polymers. Yuan et al. [17]. Photoelectric efficiency improvements were made by setting the P (VDF-TrFE) interlayer between the active layer of heterojunction and the solar cell anode. The middle layer was composed using the Languir-Blodgett (LB) method, moved to the active layer and heated at 135°C, converting the precursor unceasing thin film into a nanoscale mesa structure. As a result, the interface was split into ferroelectric areas (with a strong electric field) and electrode areas (with photo-electricity charge). Therefore, the ability to control the coverage of layer of ferroelectrics is crucial to improve photoelectric performance. Furthermore, the ferroelectric polymer thin films utilized as the interlayers for solar cell must show high crystallinity and ferroelectrical phase content. For example, comparing P (VDF-TrFE) thin films manufactured using LB and spin coating with organic solar cell interlayers exhibited that the film produced by LB method is extremely improved the efficiency of the solar cells because of its high crystallization and ferroelectric phase content in spite of its thin thickness of 3nm. Meanwhile, the spin-coated thin film did not make cell efficiency better as it acted as an insulator than a ferroelectric material [18] Inspired by traditional the (bf) method, we explain the composition of extremely crystalline P(VDF-TrFE) films with regulated porosity which is from small quantity of water. The study, as long as we know, is the pioneer report of porous P(VDF-TrFE) films which are assembled by spin coating method and used to improve the efficiency of organic and inorganic hybrid photovoltaic solar cells. Used as a rift, the size of the pore and porosity of P(VDF-TrFE) would be regulated by the quantity of water added to it, by affecting the photovoltaic efficiency of poly(3,4-ethylenedioxythiophene):poly(styrenesulfonate) (PEDOT:PSS)/Si hybrid solar cells, with P(VDF-TrFE) gap can be easily manipulated by the journey to the positive to the negative. The principal of getting improved efficiency of PEDOT:PSS/P(VDF-TrFE)/n-Si solar cells was explained grounded on FDTD simulations.

4.2 Experimental details

P (VDF-TrFE) Thin Film with porosity

A porous P (VDF-TrFE) thin film with a VDF:TrFE ratio of 3:1 was ready for using a P (VDF-TrFE) solution of acetone (15 mg/mL). The supplement of deionized water to the solution greatly changed the shape of the film produced thin films. In general, 0.3 g of P (VDF-TrFE) is melted at 20 mL acetone, which is then added to the porosity with deionized water (15-80 μL) due to the hydrophobic interaction between water and P (VDF-TrFE) which causes P(VDF-TrFE) thin film formed in the process of spin coating.

Characteristics of P(VDF-TrFE) Thin Film

The study of P(VDF-TrFE) film was found by FE-SEM equipment (Quanta200). X-rays used for XRD measure were made from X-ray tube close to Cu at generator which has 40 kV voltage and 30 mA current. The FT-IR spectrum (670, Varian) was obtained in a fully weakened reflective mode making use of a mercury cadmium telluride sensor. AFM and PFM measurements were conducted with an AFM (XE70, Park System). In the case of the images of PFM phase, the patterns were recorded in contact mode by applying an electric bias to the probe on the surface. The speed of scanning of 0.9 Hz, Alternating Current frequency of 16.786 kHz, and 1.5 V amplitudes were employed. Conducting Si cantilever coated with Pt (SCM-PIT, Brucker) were utilized to record ferroelectric area. P (VDF-TrFE) film porosity was figured from many Images of SEM such as porous P(VDF-TrFE) films.

Device Fabrication and Characterization

Spin-coated P(VDF-TrFE) / water / acetone solution on n-Si 100 substrate surface (Czochralski cultivation, 525 ± 25 μm thick, 1-10 Ω, Unisill Inc), 4 hot plates -H 140 °C. High Conducting PEDOT:PSS solution including 9wt ethylene glycol, 0.1% Triton X-100 was on the P(VDF-TrFE)/Si substrates, and the manufactured composites of PEDOT:PSS/P(VDF-TrFE)/Si were heated at 125 °C for 10 min. Silver electrodes were put in the PEDOT: PSS layer utilizing shade masks (10%, 950 μm) and electron beam evaporators. Au (200nm) / Ti (20nm) was put in the Si substrate as a lower contacts. The activated region of the device manufactured was 0.7 × 0.7 cm2. Every devices was featured by illumination AM 1.5G (100 mW/cm2) simulated utilizing solar simulator with xenon.

FDTD Simulation of PEDOT:PSS/P(VDF-TrFE)/Si Solar Cells

The latent energy of static electricity of PEDOT:PSS/P(VDF-TrFE)/Si solar cells was featured by utilizing COMSOL's closed-circuit modeling software equipped with semiconductors, Alternating Current / Direct Current and piezoelectric modules. Although this includes Ti / Au rear contact, the Ag top electrode was not taken into account since the PEDOT: PSS can role as an electrode and the hole carrying layer of the short-key joint. The conditions in boundary for Si, Shottky contacts and P(VDF-TrFE) ferroelectric films are provided along with other information [17] [19].

4.3 Results and Discussion

The porous regulated P (VDF-TrFE) thin film was put together by itself with the small amount of water as indicated in Figure 26. Sarazin et al. proposed that P (VDF-TrFE) melt in acetone solution are adjusted to fiber region of any other direction [20]. The synthetic access to the ferroelectric organic films suggested in this research was motivated by BF method, where the organic solution in the volatile solvent is vaporized in the stream of moist air to make the coinciding water absorption of vaporized water. The vaporized water affects the hydrophobic interaction with polymers , by making droplets of water with magnitude from hundreds of nanometers to micrometers. As a result, a polymer film with porosity which has a thickness of a few micrometers is fabricated by perfect solvent and humidity vaporization. The thickness of the dropped polymer film means that the resulting pores need not be connected together to offer a path to the interface with the substrate (Figure 26a). [21, 22]. However, when spin coating is utilized in place of falling casting, the rapid vaporization put poor time for absorption of water from moist air. Therefore, the polymer film did not choose a porous hole structure even though it was only n100 nm (Figure 27b) thick [23]. Accordingly, this invention proposes a modified spin coating-based BF method that overcomes the limitations of prior techniques by forming a small amount of water in an acetone's P (VDF-TrFE) solution used in spin coatings to form porous thin films (Figure 26a). The hydrophobic interaction of P (VDF-TrFE) with added water causes the formation and growth of droplets (Figures 26b and c), resulting in a uniform porous P (VDF-TrFE) thin film (Figure 26d). Compared with the conventional BF method, the amount of water added not only controls the pore size and its porosity of the P (VDF-TrFE) thin film, but also allowed the formation of a fully perforated pore structure. For example, ˜300-nm pores began to occur at an added water content of 0.25% by weight (Figures 28a and e), and the observed porosity is 5%. Increasing the moisture content increased pore size and porosity (Figs. 28b, c, f and g), i.e. ~ 4 μm porosity and 80% porosity at 0.94% by weight moisture content (Figure 28d and h). The influence of moisture content on the morphology and properties of P (VDF-TrFE) thin films was investigated by scanning electron microscopy (SEM), X-ray diffraction (XRD) and Fourier transform infrared (FT-IR) spectroscopy. Water-free P (VDF-TrFE) formed a continuous thin film characterized by random nano needle-like domains in line with previous studies (Figure 29a) [24-26]. In contrast, the addition of water led to the formation of a porous structure in which each domain was aligned in the radial pore direction (Figure 29b). This behavior was explained by the hydrophobic interaction between water and P (VDF-TrFE), reducing the contact area and total energy by directing the P (VDF-TrFE) domain in the radial direction with respect to the water droplets in the pores. Thus, porous P (VDF-TrFE) thin films exhibited extended crystalline domains, while continuous films had shorter crystalline domains (Figures 29c and 29b). Figure 29e shows the XRD pattern of continuous and porous P (VDF-TrFE) films, with sharp peaks corresponding to β-phase (110/200) reflection at 2θ ≈ 20 °. The narrower peak of the porous film showed higher crystallinity than that of the continuous film. For a more quantitative analysis, the XRD spectra were separated into crystalline (C) and amorphous (N) peaks, and the crystallinity was calculated as the C / (N + C) peak area ratio. For porous films, this parameter is 63%, much higher than the 41% value observed in continuous films. In addition, as shown in Figure 29f, porous P (VDF-TrFE) thin films are much more crystalline than copolymer films prepared by methods such as PVDF and elongation [27], polling [28], and gamma irradiation [29], Electrospinning [30,31] with high β-phase content of porous P (VDF-TrFE) thin films was also confirmed by FT-IR spectroscopy (Figure 30). Taking into account that the only factor explaining the difference between continuous and porous P (VDF-TrFE) thin films is the addition of water, the crystallinity and β phase content of porous thin films can be explained by the fact that they are fibrous domains radially with respect to the pores Aligned and tight, causing alignment and strengthening in the β-phase polarization direction. Figure 31 shows an atomic force microscope (AFM) determined topography and piezoelectric force microscope (PFM) image of a porous P (VDF-TrFE) film. For PFM measurements, there is no conductive layer on top of the ferroelectric material to clearly investigate the switching behavior [32,33]. Thus, porous P (VDF-TrFE) thin films were fabricated on n-Si / Ti / Au without the PEDOT: PSS layer, unlike solar cell structures. Thin films of porous P (VDF-TrFE) were prepared on n-Si with Ti / Au back contact. Samples for PFM measurements are made without the PEDOT: PSS layer to investigate the ferroelectric properties of the film, such as the inversion function or local polarization. Films with 65% porosity were networked in a manner that exposes the Si surface inside the pores, to a thickness of ˜150 nm (Figures 31a and 32). Figure 31b shows the downwardly polarized PFM amplitude obtained by scanning a 3 x 3 μm2 porous film using a grounded tip and applying a positive voltage to the bottom electrode. Line analysis of the PFM amplitude image (Figure 31c) clearly shows that the polarization is induced only in the network P (VDF-TrFE) region (except pores). To confirm the polarization reversal function of the porous film, downward polarization was performed in the 3 × 3 μm2 region (Figure 31d) and upward polarization was performed in the small internal region of 1 × 1 μm2. As a result, the polarization reversal (Figure 31e and f) was confirmed by a clear phase shift of 180 ° relative to the clean P (VDF-TrFE) background with uniform downward polarization, indicating a porous ferroelectric P (VDF-TrFE). . The film is suitable for use as a solar cell interlayer. Organic-inorganic hybrid solar cells based on n-type Si and PEDOT: PSS junctions are of increasing interest due to hole select transport in Schottky heterojunctions and the high transparency and hole conductivity of PEDOT: PSS [34-42]. The built-in electric field associated with the Schottky junction separates the photoelectrons and holes to create a photoelectron. Figure 33a shows a schematic of a PEDOT: PSS / P (VDF-TrFE) / Si organic-inorganic hybrid solar cell prepared using a porous P (VDF-TrFE) film as the interlayer. The ferroelectric layer strengthens the built-in electric field of the contact Si, but its insulating properties suggest that blocking the transport of charge carriers, the porosity of this layer should be optimized. Thus, we have a series of intermediate layers comprising different porous P (VDF-TrFE) films (0% for continuous thin film to 100% for nonferroelectric) with corresponding current density-voltage (J). Hybrid solar cells were prepared. -V) curves and photovoltaic performance are shown in Figure 34 and Table 9, respectively. Shows. . Clearly, solar cells with continuous ferroelectric thin films as interlayers have negligible photovoltaic effects due to the insulating properties of P (VDF-TrFE) (Figure 34a). As porosity increases, PCE and ΔPCE increase to maximum values and then decrease. Specifically, the average PCE has a porosity of 80% to 11.4%, while the PCE has a maximum value of 46.8% when the porosity is 40%. Since the previous parameters are approximately proportional to the heterojunction region between n-Si and PEDOT: PSS, the maximum values of PCE and ΔPCE are observed at different porosities, since the maximum value is achieved at a relatively high porosity of ˜80%. In contrast, ΔPCE is affected by an additional electric field induced by the ferroelectric thin film in the periphery region of the void. As shown in Figure 28, the porosity is positively correlated with the pore size, so the peripheral region is the highest at the porosity of ~ 40%. It is worth noting that solar cells with an interlayer porosity of 80% are more efficient than ferroelectric interlayer free solar cells with a layer porosity of 100%. Figure 33b shows the J-V curve of a hybrid solar cell with an 80% porosity interlayer recorded at various polling voltages (Table 10). Polling of the ferroelectric thin film was performed by applying a voltage of 0 to 20V in the positive direction and -5 to -15V in the positive direction with a negative pole PEDOT (Table 10). : PSS / P (VDF-TrFE) / Si solar cell, showing Jsc = 28.7 mA cm-2, Voc = 532 mV and FF = 53.2%, yielding PCE of 8.40%. Lower Voc and FF originate from electron-hole recombination caused by negative ferroelectric layer polling. When positive polling at a voltage of + 20 V, the PCE of PEDOT: PSS / P (VDF-TrFE) / Si solar cells improved to 11.73% with Jsc = 30.8 mA cm-2, Voc = 583 mV and FF. = 65.4%. This dramatic increase resulted in a 10% performance improvement over the corresponding non-polling cell because the amount of photogenerated charge increased due to reduced recombination. Figure 33c shows the Voc of a hybrid solar cell as a function of polling voltage. Regardless of the polling direction, Voc changes rapidly in the region between -5 and 5V and is saturated at polling voltages above 5V, suggesting that a 150nm thick P (VDF-TrFE) thin film can be sufficiently polled at voltage. , That is, at an electric field of ~ 33 MV / cm. Mai et al. By measuring the displacement-electric field (D–E) curves of P (VDF-TrFE) thin films prepared by spin coating and LB methods on the Al bottom electrode, it shows that the coercive force of this film obtained from the D-E hysteresis loop is inversely proportional. Proportional to film thickness, in the range of 43–127 MV / cm. This coercive field was significantly higher than the polling voltage of the porous P (VDF-TrFE) thin film used in this study, due to the different crystallinity of the porous and continuous P (VDF-TrFE) thin films. This polling effect can be repeatedly reversibly switched between positive and negative states. As shown in Figure 35, the bipolar device showed 11.7% at Jsc = 29.7 mA cm-2, Voc = 580 mV and FF = 68.0% in the first scan. As a result, the device was negatively polled to -15V and then 8.67% with Jsc = 28.2 mA cm-2, Voc = 550 mV and FF = 55.9% on the second scan. When the device is repeatedly switched from positive polling state to negative polling state, the efficiency is maintained at about 11% after positive polling, and the efficiency is maintained at about 8.5% after negative polling. After each cycle, all output parameters can be returned to a similar level. Figure 36 shows the Voc change of the device with or without ferroelectric layer as a function of time. Three photovoltaic devices (without positive, non-polar and ferroelectric layers) were made and polling was carried out only once after the device was manufactured. The fabricated nonpolar device showed a Voc of 563mV (black line) and a device without ferroelectric interlayer showed 570mV (green line). On the other hand, the positively connected device represents V¬ of 587 mV (blue line). PEDOT: PSS / n-Si-based solar cells are known to decompose rapidly due to the penetration of moisture into the contacts and the deterioration of VOCs [44]. Similarly, the VOC of all devices decreases over time (Figure 36a). But over time, the degradation of the device must be distinguished from the polling duration. Specifically, ΔV-oc (the V-oc difference between the non-polled and polled devices) corresponding to the magnitude of the polling effect is maintained after 12 hours, and the V-oc deteriorates over time. After 12 hours, ΔV¬ also begins to decrease (Figure 36b). As a result, the effect of polling is maintained up to 12 hours and slightly weakened. In addition, since the P (VDF-TrFE) layer can prevent moisture penetration into the junction, the stability of the hybrid solar cell is also improved. PEDOT: PSS / n-Si initially degrades from 565mV to 503mV, while the Voc of PEDOT: PSS / n-Si with ferroelectric layer decreases from 587mV to 536mV. The dark J–V curve is a good indicator of solar performance along with the curve recorded for PEDOT: PSS / P (VDF-TrFE) / Si solar cells before and after polling, as shown in Figure 33d. After positive polling, the dark saturation current decreased by more than 1 times with negative polling (Table 11), which can be explained using energy band diagrams for heterojunctions of n-Si and

PEDOT: PSS with polling P (VDF-TrFE) interlayer. The junction was assumed to be of Schottky type, similar to a metal semiconductor junction, and PEDOT: PSS acts as a metal due to its high work function. At this junction, the built-in potential ψbi at the metal-semiconductor junction is ideally defined as the difference in electron affinity of Si with band energy of PEDOT: PSS work function qϕP and qχS + (EC − EF). During thermal equilibrium setup, electrons migrate from the n-type semiconductor to the metal, causing upward band bending in the n-type Si. The presence of porous P (VDF-TrFE) at the n-Si / PEDOT: PSS interface affects the band bending along the direction of ferroelectric polarization. For positive polling (Figure 33e), the upward band bending of n-Si increases, which reduces the reverse saturation current flowing from PEDOT: PSS to Si. Conversely, in the case of negative polling, the band bending of n-Si is reduced, resulting in an almost flat band state and an increase in reverse saturation current (Figure 33f). The open circuit voltage depends on the saturation current J0 and the photogeneration current JL of the solar cell (Equation 1) [45]. Since JL typically does not show a large change, the main effect is exerted by J0, since this amount can vary by several orders, as described herein.

$$V_{OC}=\frac{nkT}{q}\ln\left(\frac{J_L}{J_0}+1\right) \qquad (1)$$

Where n is the diode anomaly coefficient, k is the Boltzmann constant, T is the absolute temperature, and q is the charge of the electron. According to equation (1), the decrease in saturation current is responsible for the increase in Voc after positive polling. The anomaly coefficients obtained by linear fitting of the J-V curve in the forward bias region are summarized in Table 11, decreasing in the order of negative polling> no polling> positive polling. After positive polling, the parameter is close to 1, implying that the recombination of electrons and holes at the n-Si / PEDOT: PSS interface is delayed. This observation can be explained by the fact that the photogenerated electrons and holes are not collected by the interfacial state between n-Si and PEDOT: PSS, but efficiently collect photon electrons and holes, reducing the anomaly coefficient to 1.0 and increasing the charge coefficient of the solar cell with the anode. FDTD simulation was performed to more clearly understand the effect of porous ferroelectric thin films on the photovoltaic performance of hybrid solar cells (Fig. 5). The geometry of the PEDOT:PSS/P(VDF-TrFE)/Si hybrid solar cell considered in this simulation is shown in Fig. 5b, featuring island-shaped ferroelectric interlayers inserted at the interface between n-Si and PEDOT:PSS. Moreover, the calculations were performed assuming a poled ferroelectric material which has the remnant polarization of 100 mCm^{-2} (detailed in derivation S1, Supporting Information). The PEDOT:PSS/Si hybrid solar cell without a ferroelectric layer was calculated to exhibit a moderate built-in potential of ~0.7 V induced by electrostatic potential energy differences, in good agreement with experimental data (Fig. 5a and 5c) [46]. However, after the ferroelectric thin film was inserted between *n*-Si and PEDOT:PSS, the built-in potential increased (Fig. 5b and 5c). Specifically, the electric field strength increased not only directly beneath ferroelectric islands (path “C” in Fig. 5c) but also in the peripheral regions of these islands not covered by the ferroelectric layer (path “B” in Fig. 5c), increasing the separation of photogenerated electron-hole pairs. Moreover, these photo generated carriers flatten the shape of the Schottky junction, the ferroelectric layers help to flow photo generated carriers and prevent recombinations. The efficient charge separation at the interface shortens the time required for the photogenerated carriers to stay at this interface, increasing their probability of being collected at the corresponding electrodes without recombining via interfacial states between *n*-Si and PEDOT:PSS. To more clearly understand the effect of porous ferroelectric thin films on the photovoltaic performance of hybrid solar cells, FDTD simulations were performed (Figure 37). The structure of the PEDOT: PSS / P (VDF-TrFE) / Si hybrid solar cell considered in this simulation is shown in Figure 37b, which features an island-like ferroelectric layer inserted at the interface between n-Si and PEDOT: PSS. In addition, calculations were performed assuming a polar ferroelectric with a residual polarization of 100 mCm-2. The PEDOT: PSS / Si hybrid solar cell without ferroelectric layer was calculated to show a good intrinsic potential of ˜0.7 V induced by electrostatic potential energy difference in good agreement with experimental data (Figures 37a and 37c) [46]. However, after the ferroelectric thin film was inserted between n-Si and PEDOT: PSS, the intrinsic potential increased (Figures 37b and 37c). Specifically, the field strength increased not just below the ferroelectric islands (path “C” in Figure. 37c) but also in the peripheral region of these islands (path “B” in Figure 37c) that is not covered by the ferroelectric layer. Separation of light-generating electron-hole pairs. In addition, these light generating carriers flatten the shape of the Schottky junction, and the ferroelectric layer helps to flow the light generating carriers and prevent recombination. Efficient charge separation at the interface shortens the time required for photogenerated carriers to stay at this interface, increasing the likelihood that it will be collected at the corresponding electrode without recombination through the interface state between n-Si and PEDOT: PSS.

4.4 Conclusion

It has developed a modified BF technique that spins a P (VDF-TrFE) solution on acetone that contains a small amount of deionized water to produce a porous, intense P (VDF-TrFE) thin film. XRD, FT-IR, and PFM measurements show that porous P (VDF-TrFE) thin films have superior crystallization and stiffness compared to continuous P (VDF-TrFE) thin films, which are due to improved crystallinity and stiffness. The electron is formed due to alignment and stacking of fibrous areas in the radial direction of the pores. Photovoltaic characteristics of the PEDOT with porous P (VDF-TrFE) interlays: PSS / Si hybrid solar cells have been proven to be reversible by repetitive positive and negative polling, and optimized iron-ferrous solar cells have a PCE of 11.73%. It was more than 10 percent higher than free solar cells between floors. The FDTD simulation clearly showed that the railway electric interlayers increased the strength of the built-in electric field between n-Si and the PEDOT:PSS, thereby facilitating the separation of the photoelectrons' electron hole pairs and suppressing recombination. The modified BF technique compared to conventional LB method is very useful for synthesis of substrate-supported porous polymer thin film by spin-coating and can be widely applied to various organic inorganic hybrid devices.

4.5 References

1. S. Fujisaki, H. Ishiwara, Y. Fujisaki, Appl Phys Lett, 90 2007, 185013

2. K. N. N. Unni, R. de Bettignies, S. Dabos-Seignon, J. M. Nunzi, Appl Phys Lett, 85 2004, 1823-1825

3. M. Y. Li, H. J. Wondergem, M. J. Spijkman, K. Asadi, I. Katsouras, P. W. M. Blom, D. M. de Leeuw, Nat Mater, 12 2013, 433-438

4. L. H. Fan, J. L. Harris, F. A. Roddick, N. A. Booker, Water Research, 35 2001, 4455-4463.

5. S. Srisurichan, R. Jiraratananon, A. G. Fane, J. Membr. Sci., 277 2006, 186-194.

6. J. F. Hester, P. Banerjee, A. M. Mayes, Macromolecules, 32 1999, 1643-1650.

7. C. H. Lang, J. Fang, H. Shao, H. X. Wang, G. L. Yan, X. Ding, T. Lin, Nano Energy, 35 2017, 146-153

8. X. H. Ren, H. Q. Fan, C. Wang, J. W. Ma, S. H. Lei, Y. W. Zhao, H. Li, N. S. Zhao, Nano Energy, 35 2017, 233-241

9. M. Choi, G. Murillo, S. Hwang, J. W. Kim, J. H. Jung, C. Y. Chen, M. Lee, Nano Energy, 33 2017, 462-468

10. W. J. Song, S. H. Joo, D. H. Kim, C. Hwang, G. Y. Jung, S. Bae, Y. Son, J. Cho, H. K. Song, S. K. Kwak, S. Park, S. J. Kang, Nano Energy, 32 2017, 255-262

11. Z. Lou, S. Chen, L. L. Wang, K. Jiang, G. Z. Shen, Nano Energy, 23 2016, 7-14.

12. F. Xia, H. S. Xu, B. Razavi, Q. M. Zhang, Mater Res Soc Symp P, 665 2002, 407-412.

13. S. J. Kang, Y. J. Park, I. Bae, K. J. Kim, H. C. Kim, S. Bauer, E. L. Thomas, C. Park, Adv. Funct. Mat, 19 2009, 2812-2818

14. W. Zeng, X. M. Tao, S. Chen, S. M. Shang, H. L. W. Chan, S. H. Choy, Energ Environ Sci, 6 2013, 2631-2618

15. W. T. Liu, X. Y. Cheng, X. Fu, C. Stefanini, P. Dario, Microelectron. Eng., 88 2011, 2251-2254

16. S. B. Kang, S. H. Won, M. J. Im, C. U. Kim, W. I. Park, J. M. Baik, K. J. Choi, Nanotechnology, 28 2017, 395402

17. Y. B. Yuan, T. J. Reece, P. Sharma, S. Poddar, S. Ducharme, A. Gruverman, Y. Yang, J. S. Huang, Nat Mater, 10 2011, 296-302

18. Y. B. Yuan, P. Sharma, Z. G. Xiao, S. Poddar, A. Gruverman, S. Ducharme, J. S. Huang, Energ Environ Sci, 5 2012, 8558-8563

19. W. Regan, S. Byrnes, W. Gannett, O. Ergen, O. Vazquez-Mena, F. Wang, A. Zettl, Nano Lett, 12 2012, 4300-4304

20. D. Sarazin, C. Picot, S. Patlazhan, Macromolecules, 39 2006, 1226-1233.

21. J. Y. Ding, A. J. Zhang, H. Bai, L. Li, J. Li, Z. Ma, Soft Matter, 9 2013, 506-514

22. H. Bai, C. Du, A. J. Zhang, L. Li, Angew. Chem. Int. Ed. 52 2013, 12240-12255

23. A. Munoz-Bonilla, E. Ibarboure, E. Papon, J. Rodriguez-Hernandez, Langmuir, 25 2009, 6493-6439

24. S. J. Kang, Y. J. Park, J. Hwang, H. J. Jeong, J. S. Lee, K. J. Kim, H. C. Kim, J. Huh, C. Park, Adv Mater, 19 2007, 581.

25. C. Harnagea, M. Alexe, J. Schilling, J. Choi, R. B. Wehrspohn, D. Hesse, U. Gosele, Appl Phys Lett, 83 2003, 1827.

26. L. Zhang, S. Ducharme, J. Li, Appl Phys Lett, 91 2007, 123974

27. A. Salimi, A. A. Yousefi, Polym Test, 22 2003, 699-704

28. V. Sencadas, S. Lanceros-Mendez, J. F. Mano, Thermochim Acta, 424 2004, 201-207

29. M. H. A. Rahaman, M. U. Khandaker, Z. R. Khan, M. Z. Kufian, I. S. M. Noor, A. K. Arof, Phys Chem Chem Phys, 16 2014, 11527-11537

30. L. Persano, C. Dagdeviren, Y. W. Su, Y. H. Zhang, S. Girardo, D. Pisignano, Y. G. Huang, J. A. Rogers, Nat. Commun., 4 2013, 1633

31. C. H. Du, B. K. Zhu, Y. Y. Xu, J Appl Polym Sci, 104 2007, 2254-2259

32. B.B. Tian, J.L. Wang, S. Fusil, Y. Liu, X.L. Zhao, S. Sun, H. Shen, T. Lin, J.L. Sun, C.G. Duan, M. Bibes, A. Barthe´le´my, B. Dkhil, V. Garcia, X.J. Meng, J.H. Chu, Nat comm 7 2016,11502

33. Z.Wen, C. Li, D. Wu, A. Li, N. Ming, Nat Mater 12 2013, 617-621

34. J. Zhang, T. Song, X. L. Shen, X. G. Yu, S. T. Lee, B. Q. Sun, *ACS* Nano, 8 2014, 11369-11376

35. J. Y. Chen, C. Con, M. H. Yu, B. Cui, K. W. Sun, ACS Appl. Mater. Interfaces, 5 2013, 7552-7558

36. H. M. Zhao, D. Xie, T. T. Feng, Y. F. Zhao, J. L. Xu, X. M. Li, H. W. Zhu, T. L. Ren, Appl Phys Express, 7 2014, 031603

37. L. N. He, C. Y. Jiang, H. Wang, D. Lai, Rusli, Appl. Phys. Lett, 100 2012, 073503

38. N. Ikeda, T. Koganezawa, D. Kajiya, K. Saitow, J Phys Chem C, 120 2016, 19043-19048.

39. H. J. Syu, S. C. Shiu, C. F. Lin, Sol Energ Mat Sol C, 98 2012, 267-272.

40. Q. M. Liu, T. Ohki, D. Q. Liu, H. Sugawara, R. Ishikawa, K. Ueno, H. Shirai, Nano Energy, 11 2015, 260-266.

41. L. Mao, Q. Chen, Y. W. Li, Y. Li, J. H. Cai, W. M. Su, S. Bai, Y. Z. Jin, C. Q. Ma, Z. Cui, L. W. Chen, Nano Energy, 10 2014, 259-267.

42. X. H. Mu, X. G. Yu, D. K. Xu, X. L. Shen, Z. H. Xia, H. He, H. Y. Zhu, J. S. Xie, B. Q. Sun, D. R. Yang, Nano Energy, 16 2015, 54-61.

43. M. F. Mai, B. Martin, H. Kliem, J Appl Phys, 110 2011, 064101

44. J. Schmidt, V. Titova, and D. Zielke Appl. Phys. Lett. 103, 2013, 183901

45. K. Bouzidi, M. Chegaar, A. Bouhemadou, Sol Energ Mat Sol C, 91 2007, 1647-1651.

46. S. Jackle, M. Mattiza, M. Liebhaber, G. Bronstrup, M. Rommel, K. Lips, S. Christiansen, Sci Rep, 5 2015, 13008

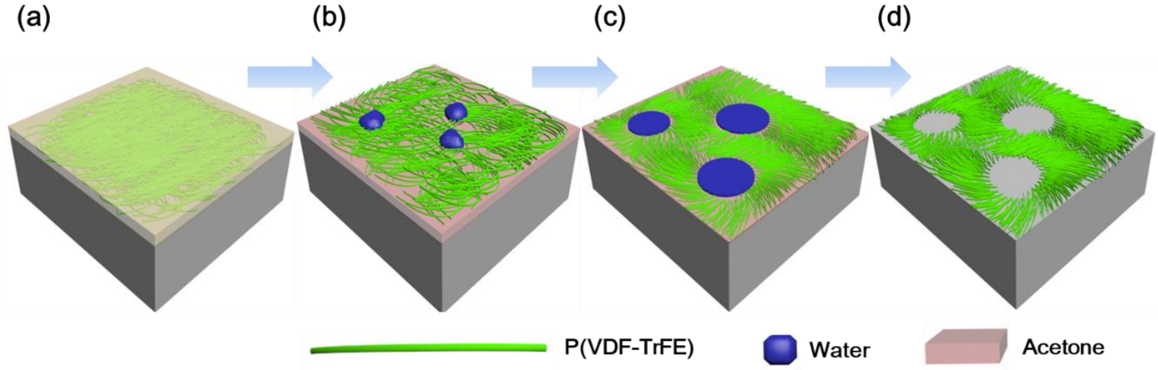

Figure 26. Schematic fabrication of P(VDF-TrFE) porous thin films. (a) Homogenous solution of P(VDF-TrFE) and water in acetone, (b) coalescing water droplets in solution, (c) expansion of coalesced water droplets during spin coating, and (d) self-assembled porous ferroelectric P(VDF-TrFE) thin film after complete evaporation of all solvents.

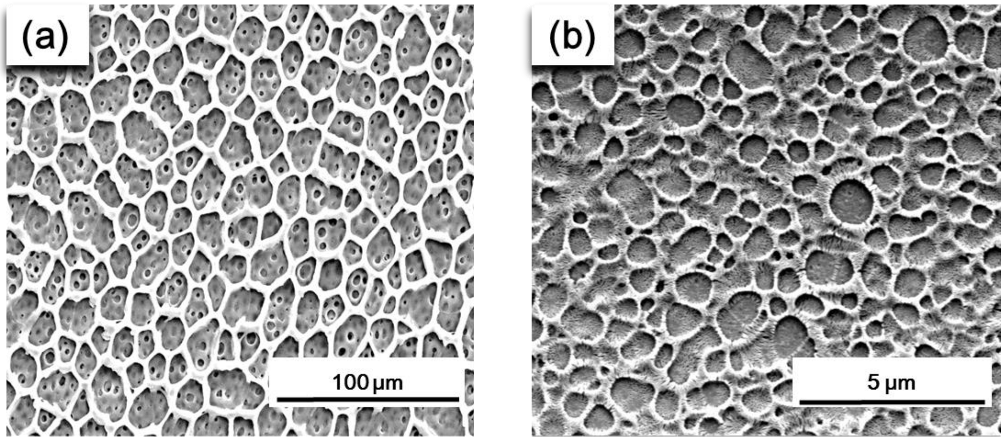

Figure 27. SEM images of porous P(VDF-TrFE) films prepared using (a) the static breath figure method and (b) spin coating without added water under humid conditions (relative humidity = 80%).

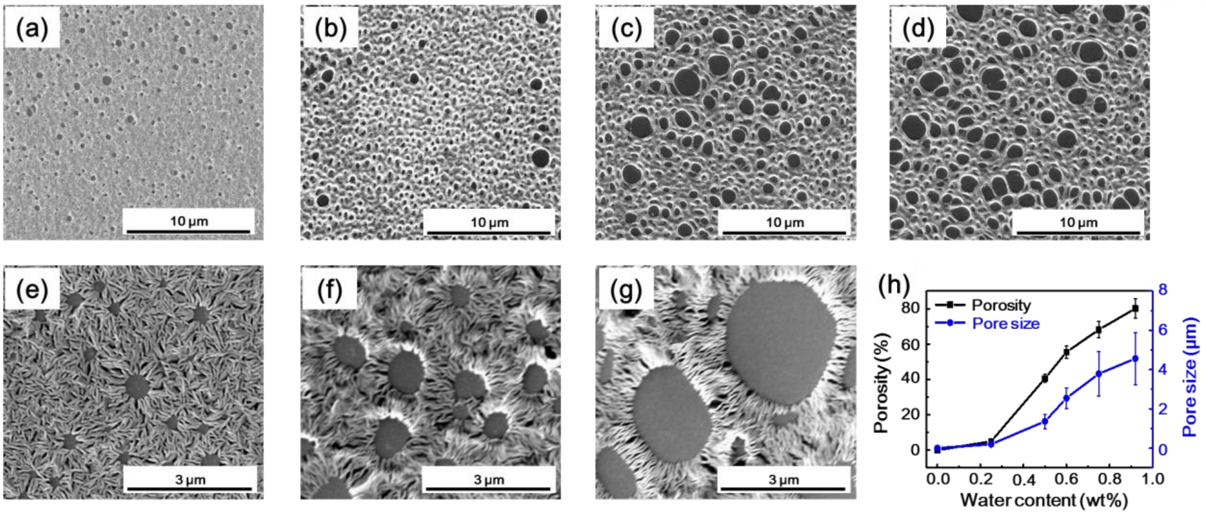

Figure 28. High-magnification SEM images of P(VDF-TrFE) porous thin films with added water contents of (a, e) 0.25 wt%, (b, f) 0.45 wt%, (c, g) 0.75 wt%, and (d) 0.9 wt%. (h) Dependence of pore size and porosity on the amount of added water.

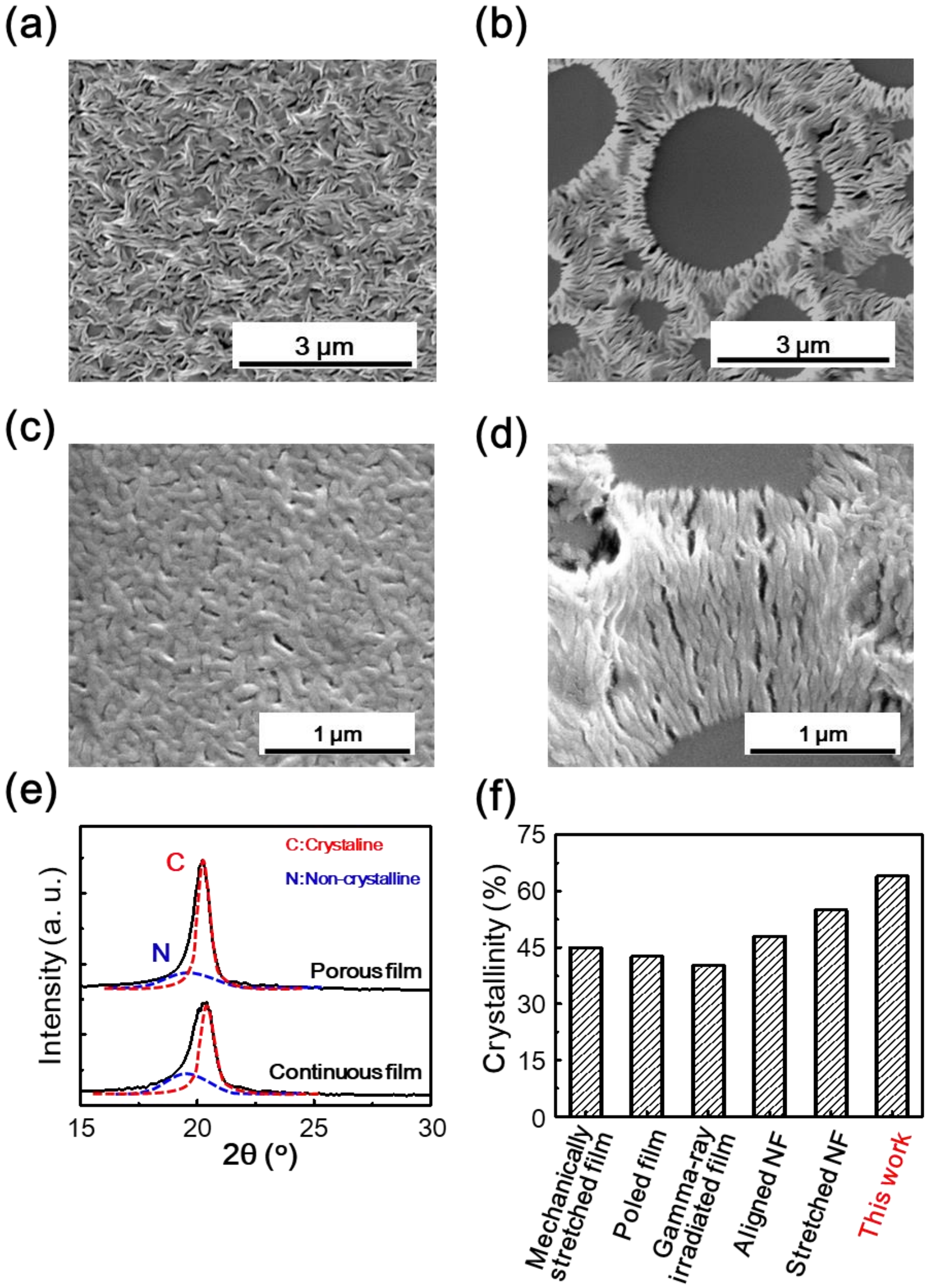

Figure 29. SEM images of (a,c) continuous and (b,d) porous P(VDF-TrFE) thin films. (e) XRD patterns of continuous (black line) and porous (red line) P(VDF-TrFE) thin films, (f) crystallinities of PVDF/P(VDF-TrFE) films prepared by methods reported elsewhere

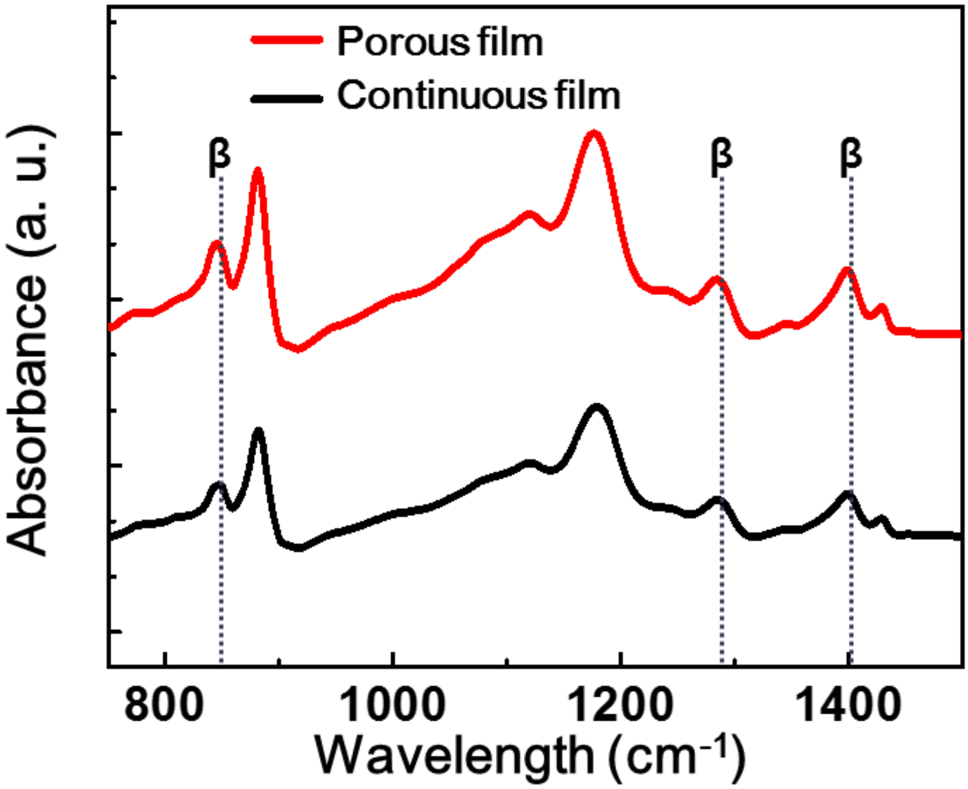

Figure 30. FT-IR spectra of continuous (black line) and porous (red line) P(VDF-TrFE) thin films, with polar β-phase bands appearing at 846, 1285, and 1431 cm^{-1}.

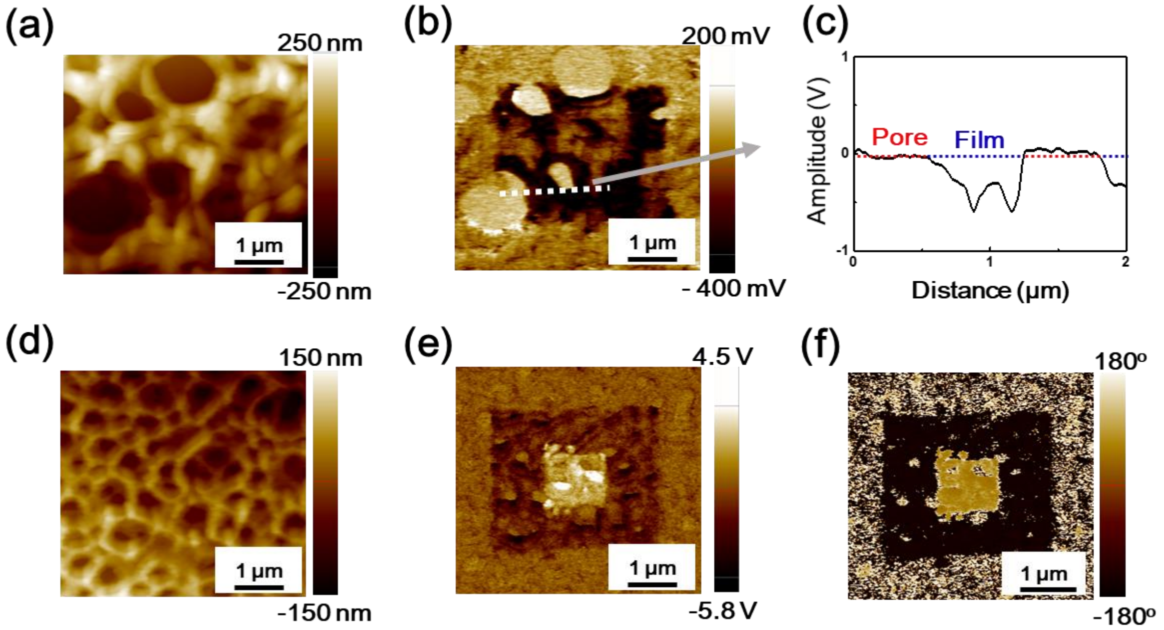

Figure 31. AFM and piezoresponse images of a P(VDF-TrFE) porous film. (a) AFM topography, (b) PFM amplitude for a film with 65% porosity poled at +10 V over the central 3 × 3 µm2 area. (c) Line scanning of PFM amplitude. (d) AFM topography, (e,f) PFM amplitude, and PFM phase for a film with 40% porosity poled at +10 and –10 V over 3 × 3 and 1 × 1 µm2 areas, respectively .

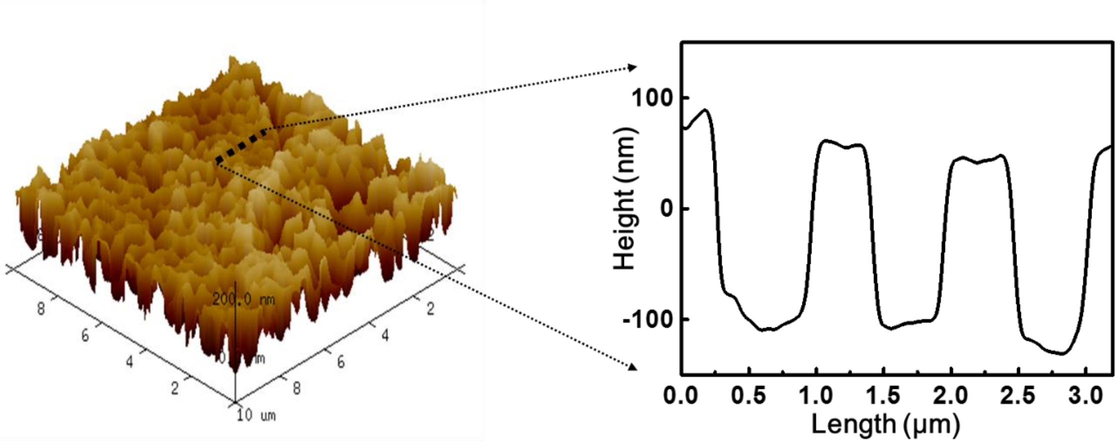

Figure 32. 10 × 10 µm^2 three-dimensional topological AFM image of a porous P(VDF-TrFE) thin film.

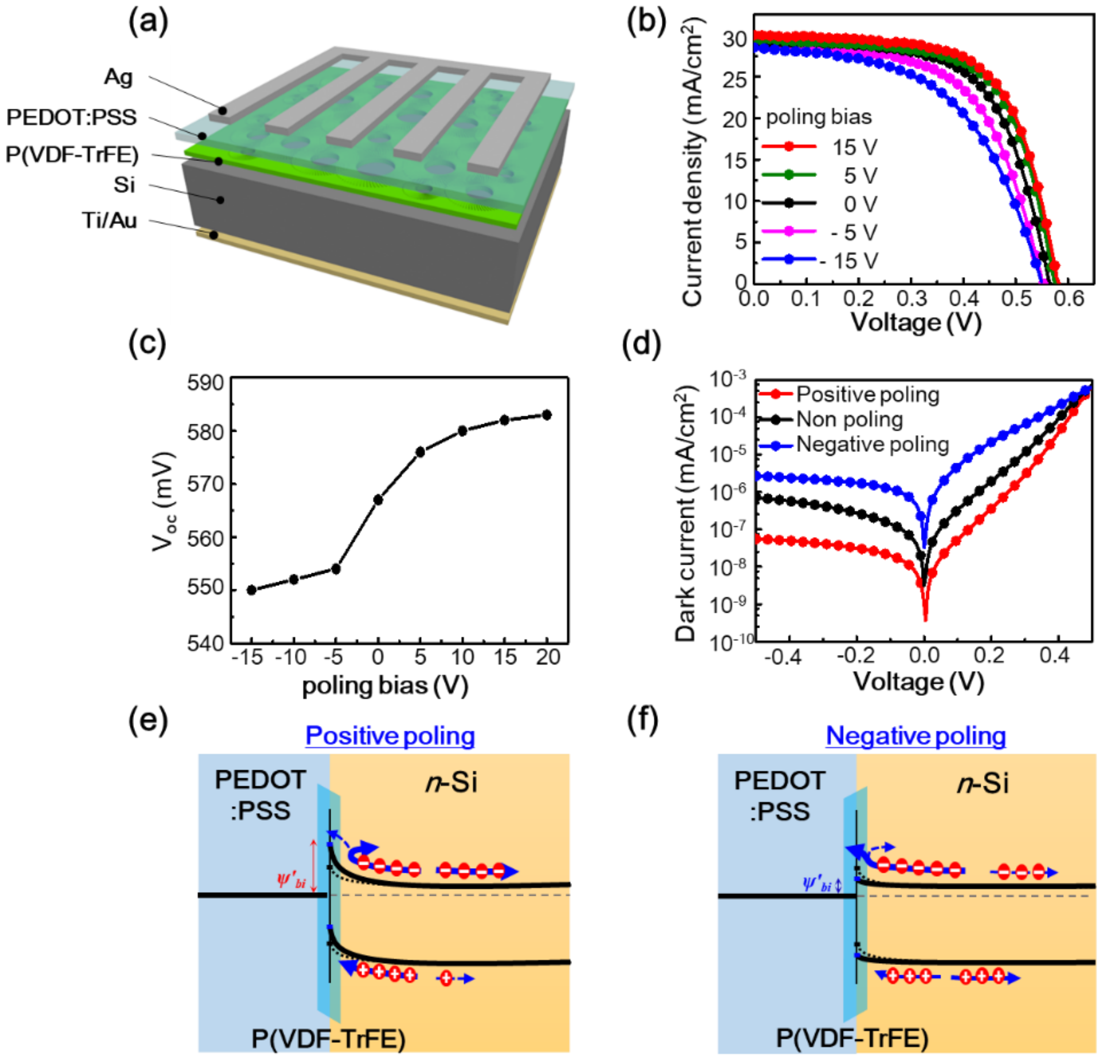

Figure 33. (a) Schematic illustration of a PEDOT:PSS/P(VDF-TrFE)/Si solar cell and photovoltaic performance variation upon insertion of a porous P(VDF-TrFE) thin film between PEDOT:PSS and Si. (b) J–V curves for 1-sun-illuminated devices poled under different conditions. (c) Open circuit voltage as a function of poling voltage. (d) Dark J–V curves of devices subjected to positive poling (red line), no poling (black line), and negative poling (blue line). Band diagram and working principles of the porous ferroelectric P(VDF-TrFE) interlayer for hybrid solar cells under positive (e) and (f) negative poling conditions.

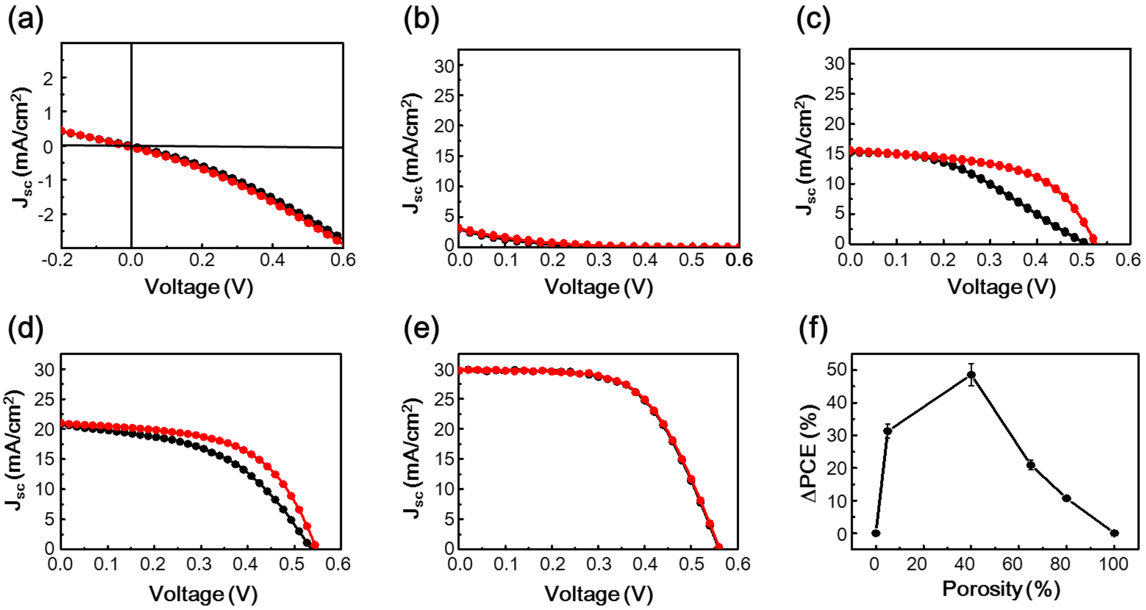

Figure 34. J–V curves of 1-sun-illuminated devices containing P(VDF-TrFE) films with porosities of (a) 0%, (b) 5%, (c) 40%, (d) 65%, and (e) 100% before (black lines) and after positive poling (red lines, +20V). (f) Post-poling efficiency enhancement as a function of film porosity.

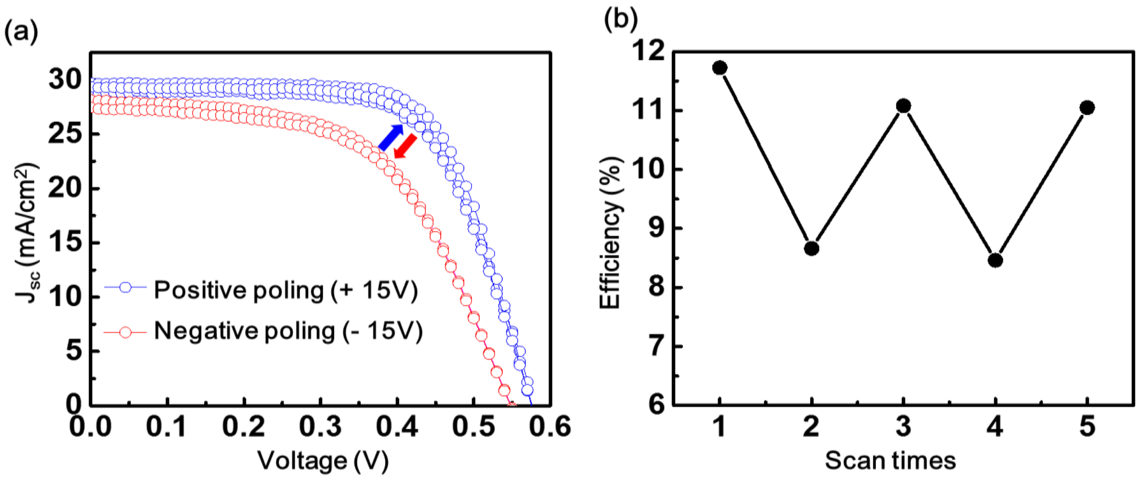

Figure 35. Reversible behaviors of the poling effect (a) J-V characteristics of PEDOT:PSS/P(VDF-TrFE)/n-Si hybrid solar cell. (b) The efficiency of PEDOT:PSS/P(VDF-TrFE)/n-Si hybrid solar cell are switched from positive poling state to negative poling state repeatedly.

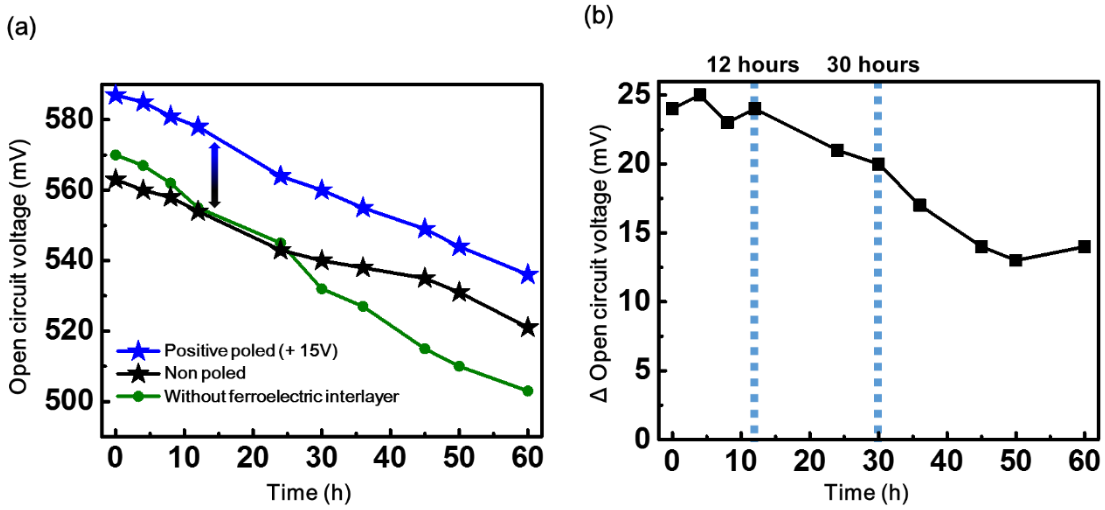

Figure 36. (a) The open circuit voltage of PEDOT:PSS/n-Si solar cell without ferroelectric interlayer (green line), non-poled (black line), and positively poled (blue line) PEDOT:PSS/P(VDF-TrFE)/n-Si solar cell as a function of elapsed time after device fabrication (b) The changes of the open circuit voltage between positively poled and non poled devices as a function of elapsed time after device fabrication..

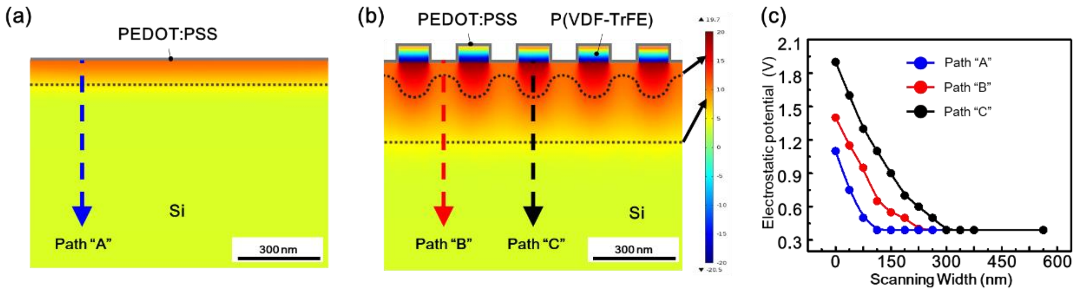

Figure 37. FDTD electrostatic potential simulation for (a) PEDOT:PSS/n-type Si solar cell and (b) PEDOT:PSS/n-type Si solar cell with a ferroelectric layer; (c) line scans along paths A, B, and C.

Table 9. J–V characteristics of PEDOT:PSS/P(VDF-TrFE)/Si solar cells containing ferroelectric films of different porosities before and after poling as 20 V

Porosity of P(VDF-TrFE)		J_{sc} [mA/cm^2]	V_{oc} [V]	FF [%]	PCE [%]	Δ PCE [%]
0% (continuous film)	-	-	-	-	-	-
5%	Before poling	3.05 (± 0.15)	0.495 (± 0.01)	9.0 (± 0.5)	0.13 (± 0.05)	**31.30**
	After poling	3.16 (± 0.19)	0.506 (± 0.01)	11.0 (± 0.7)	0.18 (± 0.05)	
40%	Before poling	15.29 (± 0.05)	0.505 (± 0.02)	39.5 (± 4.5)	3.05 (± 0.26)	**46.8**
	After poling	15.59 (± 0.08)	0.527 (± 0.04)	54.5 (± 3.4)	4.48 (± 0.22)	
65%	Before poling	20.88 (± 0.11)	0.537 (± 0.03)	47.7 (± 3.1)	5.35 (± 0.35)	**20.9**
	After poling	21.07 (± 0.17)	0.549 (± 0.04)	56.0 (± 3.8)	6.47 (± 0.50)	
80%	Before poling	29.97 (± 0.08)	0.564 (± 0.03)	59.5 (± 2.5)	10.1 (± 0.25)	**11.3**
	After poling	30.13 (± 0.14)	0.578 (± 0.04)	65.2 (± 3.7)	**11.4 (± 0.38)**	
100% (Non-ferroelectric)	Before poling	29.7 (± 0.03)	0.560 (± 0.01)	60.3 (± 2.5)	10.0 (± 0.22)	**0.01**
	After poling	29.7 (± 0.07)	0.560 (± 0.01)	60.8 (± 3.0)	10.1 (± 0.25)	

Table 10. J-V characteristics of PEDOT:PSS / P(VDF-TrFE) / Si solar cells with poling voltage

Poling voltage [V]	-15	-10	-5	0	5	10	15	20
V_{oc} [V]	0.55	0.552	0.554	0.567	0.576	0.58	0.582	0.583
Current density [mA/cm^2]	28.7	29.2	29.5	29.9	30.2	30.3	30.6	30.8
FF [%]	53.2	57.5	59.2	62.5	65.0	65.0	65.1	65.4
Efficiency [%]	8.40	9.25	9.67	10.58	11.30	11.44	11.59	11.73

Table 11. Reverse saturation current density (Js) and ideality factor (n) of PEDOT:PSS/P(VDF-TrFE)/Si solar cell before and after poling

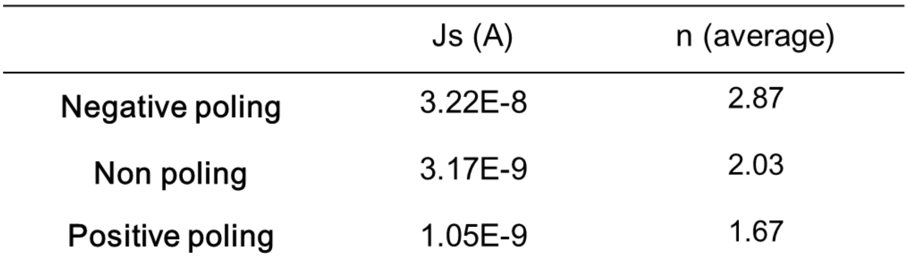

	Js (A)	n (average)
Negative poling	3.22E-8	2.87
Non poling	3.17E-9	2.03
Positive poling	1.05E-9	1.67

CHAPTER 5. Si / P(VDF-TrFE) hetero-interface for back surface field layer in solar cells

5.1 Research background

The surface of the semiconductor is the key to determine the performance of devices including transistors, optoelectronics and photovoltaics.[1-4] In particular, for the Si-based solar cells, obtaining the high effective carrier lifetime (τ_{eff}) at the surfaces enables the large open-circuit voltage (Voc) of the device. [5-8] Thus, the reduction of recombination process is essential for high-efficient solar cells. One effective strategy is the formation of the surface-field by diffusion of high concentrations of dopants such as Al, phosphine (PH_3) or diborane ($B2H_6$) on p-type or n-type Si surfaces at high temperatures. [9, 10] However, it results in the creation of additional Si dangling bonds and activation of metastable defects due to the high process temperatures (800 ~ 1000 ^oC).[11, 12] On the other hand, chemical and field-effect passivation are common ways to prevent recombination. Surface defects such as dangling bonds on the Si surface are reduced in a chemical manner by concentrated hydrofluoric acid (HF), methanol or the deposition of hydrogenated amorphous silicon (a-Si:H).[13-15] The field-effect passivation has been widely used in Si photovoltaic technologies by taking advantage of nitride or oxide thin films with Al_2O_3, SiN_x, ZrO_x, and TaO_x. [16-21] In this case, the electric field is established by a fixed charge density from the dielectric film leading to the band bending of Si. Among them, a-Si:H and oxides are considered to be the most preferred way to generally adapt to the Si solar cells due to their excellent passivation effect. Thus, the state-art-of Si solar cells such as passivated emitter rear cell (PERC), heterojunction with an intrinsic thin layer (HIT) or interdigitated back contacts (IBC) with photovoltaic conversion efficiency (PCE) of 23 ~ 26 % have been developed with the device architectures taking advantage of a-Si:H, oxides or nitrides, minimizing the recombinations at the surfaces. [8, 22-25] However, such passivation techniques generally require heavy and expensive vacuum processes, including plasma-enhanced chemical vapor deposition (CVD) and atomic layer deposition. Moreover, conventional thin-film based passivation is stable but accompanied by additional chemical, post-annealing at high temperature or under the forming gas to enhance the passivation quality.[26, 27] In addition, the fabrication process for the state-art-of Si solar cells is very complicated rather than the devices based on Al back-surface-field (BSF) and thus the technical features of schemes including passivation and post-process poses challenges to reduce the costs.

Alternatively, organics that can be processed at low-temperature via solution process have been recently revisited in the field of Si-based photovoltaics. Specifically, the researches on organic materials that can be applied to passivation or junction layers are actively underway. In terms of passivation, organic superacid, polystyrenesulfonate and Nafion were recently reported as the superior passivation layer for the Si over the previous organics providing low τ_{eff} and poor air-exposed longevity.[28-31] Notably, the Nafion films with the dip- or spin-coating are effective for both p and n-type Si and provide Si surface passivation of up to τ_{eff} = 9 ~ 12 ms.[29, 31] However, their passivation mechanisms which are effective to both types of Si have not been clearly understood and still require further investigation. In addition, there has been little discussion of organic passivation layers for practical applications in Si-based photovoltaic devices.

In the approaches utilizing the organics as junction layers, the PEDOT:PSS as hole-selective layers is the most promising partner of Si.[32-34] The high work function of PEDOT:PSS forms Schottky junctions with n type Si (n-Si), separating the photogenerated electrons and holes and creating a photocurrent. To date, hybrid solar cells of n-Si / PEDOT:PSS exhibited the PCE of more than 16% via advanced surface texturing on Si and interfacial engineering between Si and PEDOT:PSS.[35-38] In order to achieve a 16 % of relatively high PCE of the device, a doping process or vacuum or high-temperature process involving the deposition of an a-Si:H or oxide layer on the rear-side of Si is usually accompanied.[35, 37, 39,40] However, this ignores the original motivation of hybrid solar cells which is fabricating the Si-based photovoltaics in a simple and inexpensive way. Additionally, the PCE of 16% is not enough with the vacuum and expensive processes since the state-of-the-art Si solar cells have already easily achieved more than the PCE of 22% using the same process.

In this study, we developed porous and crystalline P(VDF-TrFE) thin film and analyzed its extraordinary crystallinity via Grazing incident X-ray diffraction. More importantly, we demonstrated that the films provide superior passivation to both p- and n-Si. Due to its switchable ferroelectric properties, polarization-induced-passivation is enhanced with the additional electric field and manipulated to maximize τ_{eff} at p- or n-Si, respectively. For the application to the solar cells, the P(VDF-TrFE) thin films are spin-coated on the bottom of the n-Si surface by modified breath figure methods. After that, PEDOT:PSS is formed on the top of nano-textured Si as the junction. Finite-difference time-domain simulation reveals that the electric field causes band bending of Si, reflecting minority carriers and reducing the surface recombinations of the devices. Moreover, when applying it to the p-type homojunction solar cells, it was shown to be a better-passivated BSF layer than the existing Al-based BSF. In addition, the photovoltaic parameters were maintained, passing a standard 1000 h damp heat test, with >95% of their initial performance.

5.2 Experimental details

Fabrication of black Si

Cone-shape of Si nanostructures at black Si have been obtained using equal flows of 60 sccm for SF_6 and O_2 by inductively coupled plasma reactive-ion etching (ICP-RIE) process (ICP380, oxford instrument). After ICP-RIE, the damaged Si surface was treated and removed by piranha solution and slow Si etchant (RSE-100, TRANSENE).

Fabrication and characterization of porous P(VDF-TrFE) Thin Films

The powder of P(VDF-TrFE) (VDF:TrFE=75:25, Solvay) was purchased from Solvay and used in the experiments without further purification. Porous thin films were prepared using a solution of P(VDF-TrFE) in acetone, dimethylformamide or dimethyl sulfoxide (15 mg/mL). Moreover, itric acid to the above solutions. After that, the solutions were spincoated on the Si substrate followed by 4-h annealing at 135 °C on a hotplate. The highly crystalline thin film was only obtained with a solution of P(VDF-TrFE) in acetone. The morphology of P(VDF-TrFE) films was characterized by scanning electron microscopy (Quanta200 FE-SEM, FEI). GIXD data was acquired at PLS-II 9A U-SAXS beamline of Pohang Accelerator Laboratory in Korea. X-ray beam at 11.015 keV ($\lambda = 1.12574$ Å) was obtained by monochromating the X-rays coming from the in-vacuum undulator (IVU) by a double crystal monochromator. The X-ray beam was irradiated in the incidence angle of 0.13° and for 3-30 s. GIXD patterns were recorded by a 2D CCD detector (SX165, Rayonix, USA) with the sample-to-detector distance (SDD) of 222.6 mm.

Device Fabrication

The PEDOT:PSS / n-Si solar cells were fabricated with one-side polished, Czochralski, n-type ($N_d \approx 1 \times 10^{17}$ cm^{-3}) wafers with a thickness of 525 μm. The un-polished (bottom) side of Si wafer was planarized and slightly textured by 15 % (w/w) of potassium hydroxide solution.

After that, cone-shaped nanostructures were formed on polished (top) side of Si by ICP-RIE for fabricating black-Si. The ~ 2 nm-thick Al_2O_3 layer was deposited on black Si substrate by Cluster ALD (Atomic premium, CN1) and then the samples were annealed at 400 ◦C for 20 min in forming gas ambient (5 % of H_2 in N_2) to activate the surface passivation. The porous P(VDF-TrFE) thin film was spincoated on bottom side of Si and Ti(20 nm)/Au(200 nm) was deposited as a bottom electrodes. Finally, A PEDOT:PSS (CLEVIOS PH 1000) solution containing 8 wt% ethylene glycol and 0.1 wt% Triton X-100 was spin coated Al_2O_3/black-Si substrates and annealed at 125 °C for 10 min. A silver electrode was deposited on top of the PEDOT:PSS thin film using a shadow mask (Areal coverage ≈ 10%, 950 μm of spacing between the silver contacts).

A double-sided, polished, floating zone (FZ) 1–5 ohm cm p-type Si wafer <100> with a thickness of 300 μm was used to prepare a p-type homojunction (n++ emitter / p type black Si) solar cells. The both side of Si substrate was etched and textured like the case of PSC. After that, the phosphorus SOD (Filmtronics SOD P507) were spin-coated on the c-Si wafers and n++ emitter was formed with heat treatment at 900 °C for 2 min using a rapid thermal annealing system. The residual phosphorous silicate glass was removed by hydrogen fluoride. Subsequently, the Ti (20 nm) / Ag metal top grid electrodes (1 μm) were deposited by e-beam evaporation. The rest of the non-contacted rear was passivated by 20 nm-thick Al_2O_3 layer. Finally, the porous P(VDF-TrFE) thin film was spincoated on bottom side of Si followed by deposition of Au (500 nm) as a bottom contacts.

Set up and conditions for Corona poling

Corona triode configuration is utilized for the corona poling. Corona and grid voltages were applied to a tungsten needle and a grid electrode, respectively, which were operated independently by two different power supplies. The grid voltage was fixed to 70 V and the corona voltage applied to the needle was varied from 0 kV to 20 kV for positive charging. Vice versa, for negative charging, - 70 V for the grid voltages and 0 kV to -20 kV for corona voltages were applied. Moreover, the corona discharge was conducted in ambient air.

5.3 Results and Discussion

The ferroelectricity of P(VDF-TrFE) thin film is mainly determined by the crystallinity of the film such as crystal orientation and size of the grain. Commonly, P(VDF-TrFE) thin films are formed by spin-coating process and annealed at 135°C, which is a well-known process to obtain the thin film with a moderate degree of crystallinity, indicating the needle-like structure of domains in P(VDF-TrFE) (Figure 38a). However, to fully utilize the ferroelectric property of P(VDF-TrFE) thin films, the crystallinity of the films should be further enhanced for spurring the performance of memories, transistors and solar cells. Recently, Lee et al formed highly crystalline P(VDF-TrFE) thin films by taking advantages of single-crystalline organic semiconductor rubrene as a substrate. Moreover, Kim et al demonstrated an epitaxial form of P(VDF-TrFE) thin films on graphene. However, the crystallinity of thin films is strongly depending on the specific substrates and it needs for melt and re-crystallization process, limiting the broader applications. Previously, we reported that highly crystalline P(VDF-TrFE) thin films can be fabricated by a simple spin-coating process with the addition of water to the solution. The porous morphology and enlarged grains in the thin films are totally originated from self-assembly in the solution during the spin-coating process via the hydrophobic interactions between P(VDF-TrFE) and water. Therefore, when using the 59 wt % HNO_3 in water as an additive to the solution, the porosity can be controlled by the amount of additive in the same way. Moreover, the crystalline and porous P(VDF-TrFE) thin films can be formed on the various substrate whether it is hydrophilic SiO_2 or hydrophobic Si and Cu, indicating that there is no dependency on the substrates unlike other methods (Figure 39). Moreover, we found that the structural evolution of the thin film does not only occur by just adding water to the solution. Even if the water is added to the solution, the highly crystalline structures or even pores are not observed with the solvents for P(VDF-TrFE) such as N,N-Dimethyl methanamide (boiling-point = 153 °C) and Dimethyl sulfoxide (boiling-point = 189 °C) (Figure 40). However, when using the acetone as a solvent for P(VDF-TrFE), the porous and crystalline P(VDF-TrFE) thin films are formed (Figure 38b). As the water vapors are absorbed into solution instead of quickly evaporated acetone (boiling-point = 56 °C), the water droplets are expanded and engaged in maximizing hydrophobic interactions with P(VDF-TrFE) during spin-coating process. This means that the rapid evaporation of the solvent is the key to control the size and alignment of micro-grains in P(VDF-TrFE) thin films. Grazing incident X-ray diffraction (GIXD) was performed to investigate the molecular and crystal arrangement of the

P(VDF-TrFE) thin films. The pristine thin film fabricated by using acetone solution without water additive exhibits (200) plane in a 2D diffraction pattern (Figure 38c). This is a well agreement with previous GIXD results of the spin-coated and subsequently annealed film at 130~135 °C. In comparison, the reflection from (110) at an azimuthal angle, $\phi = 30°$ which is a clear indicator of the epitaxial property of P(VDF-TrFE) thin films is evidently observable at the crystalline and porous thin films fabricated with water additive (Figure 38d). It is noted that full-width half-maximum (fwhm) of the (200) reflection of porous thin films is much smaller than that of pristine thin films, confirming the better crystallinity of porous thin films due to strong structural correlation from self-assembly and hydrophobic interactions. (Figure 41a and b). To understand the interfacial property between P(VDF-TrFE) and Si, X-ray photoelectron spectroscopy (XPS) depth-profiling data is acquired with Ar^+ ion sputtering. Then, the obtained spectra were analyzed to determine the interface between continuous P(VDF-TrFE) / Si and crystalline P(VDF-TrFE) / Si, respectively. In the case of continuous P(VDF-TrFE) / Si, the Si 2p core-level spectrum exhibited only one peak at ~ 99.4 eV corresponding to Si^0 (Si) at the surface and the subsequent etching process. Due to the small pinholes in the continuous films, the peak of 99.4 eV derived from the Si appears from the surface. Moreover, in approach to the interface, the signal intensity at 99.4 eV is increased, indicating that the P(VDF-TrFE) thin film is etched and the Si surface is exposed (Figure 42). Interestingly, the additional peak of ~104 eV matching to the Si^{4+} (SiO_2) state appears at the Si 2p spectrum of crystalline P(VDF-TrFE) / Si. A high-quality oxide layer is formed during the spin-coating of P(VDF-TrFE) solution containing nitric acid and a subsequent annealing process. In addition, the porous structure of the crystalline P (VDF-TrFE) thin film results in Si^0 (Si) and Si^{4+} (SiO_2) peaks from the surface before the etching (black line, Figure 43a). As with the continuous thin film, it is seen clearly that with proceeding etching the intensity of peaks gradually increase. However, in particular, after passing the certain point, then the intensity of Si^{4+} decreases back, meaning that the oxide layer at the interface between P(VDF-TrFE) and Si was etched by Ar^+ ion. Therefore, the yellow line in Figure 43a when the peak of ~104 eV is maximized can be regarded as the Si 2p spectrum of the interface and these results clearly show that the presence of the SiO_x layer on the top of Si and underneath of P(VDF-TrFE). In addition, the C 1s spectra taken near the interfaces for both samples provide valuable information on crystallinity and chain conformation of the P(VDF-TrFE) films at the interfaces. For the The C 1s XPS spectrum showed the signal peaks of H–C–H, H–C–F and F–C–F, presenting the P(VDF-TrFE). As shown in Figure 43b, the peak of hydrocarbon (CH_2) is dominant rather than fluorine-bonding carbons (CHF, CF_2) at the interface between the continuous P (VDF-TrFE) thin film and Si, indicating the poor crystallinity of the film. In addition, the crystallinity of the film on the surface is not maintained at the interface. Conversely, the intensive structural correlation of crystalline P(VDF-TrFE) thin films led to a 1.0−1.4 eV higher energy shift. More importantly, strong peak of CF_2 appeared as well as CH_2, suggesting that the chain conformation is well-aligned with high crystallinity at the interface. Based on the XPS measurement, the interfaces of continuous P(VDF-TrFE) / Si and crystalline P(VDF-TrFE) / Si are schematically illustrated in Figure 43d and 43e, respectively. The P(VDF-TrFE) chains are randomly arranged on the Si surface in case of the interface between continuous P(VDF-TrFE) and Si without any directionality. In contrast, the additive creates a thin SiO_2 during fabrication process and the highly crystalline P (VDF-TrFE) is formed with a preferential orientation towards SiO_2 / Si.

Furthermore, to verify the surface charge dynamics of crystalline P(VDF-TrFE) thin film on Si, Atomic force microscopy (AFM) and scanning kelvin probe microscopy (SKPM) were performed. The thin film is networked and the Si surface inside pore is exposed without any contaminants (Figure 43a). Particularly, the surface potential of P(VDF-TrFE) exhibited high positive potential about ~ 400 mV, implying positive charges are at the surface of P(VDF-TrFE) and negative charges are at the interface (Figure 44b and c). These are also in good agreement with schematic illustration that the Si surface is passivated by multilayers of thin SiO_x and negative charges from P(VDF-TrFE). The passivation effect of P(VDF-TrFE) layer was then investigated on both n and p-Si wafers. Comparing SiO_2 or SiN_x thin films which are conventionally used for Si passivation layer with the P(VDF-TrFE), A superior passivation effect is achieved with P(VDF-TrFE) thin films on both p- and n-type Si surface, with τ_{eff} of 3.9 ms and 3.3 ms, respectively (Figure 44d and e). The ultra-thin SiO_2 layer predominantly can reduce the dangling bonds at the Si surface and minimize recombination probabilities of carriers. Moreover, the surface passivation is ruled for a partial part by polarization-induced passivation induced by a relatively negative charges of P(VDF-TrFE). Because recombination process requires the presence of both electrons and holes, surface recombination can be lowered by reducing the number of one type of carriers available at the surface. Negative charges reduce the minority carrier concentration near the p-type Si surface and thus the surface recombination is effectively suppressed. On the other hands, a surface depletion layer is formed near the n-type Si surfaces due to the repulsion of electrons. Then, recombinations can be decreased as the same mechanism of Al_2O_3 layer which is known for effective passivation layers for n-type Si surfaces due to their negative fixed charge. However, unpoled state of

P(VDF-TrFE) is more likely to the dielectric layers. Thus, the polarization-induced passivation can be further enhanced and the polarity of charges can also be manipulated to maximize it due to the ferroelectric property of P(VDF-TrFE). Corona poling is powerful method to pole the ferroelectric materials in non-contact way or to control the charges of dielectric layers including Al_2O_3. The positive or negative voltages were applied to the P(VDF-TrFE) thin films on Si under the ambient air as described elsewhere. As shown in Figure 44f, the polarization-induced passivation is governed by the charge polarity of P(VDF-TrFE), indicating the ambipolarity. It is noteworthy that the τ_{eff} of both n and p-type Si is rather decreased when the 2 kV of corona voltage is applied. At this stage, the negative charge is balanced and neutralized with a positive corona charge, negating the polarization-induced passivation of P (VDF-TrFE). Therefore, the passivation level is similar to the state where only SiO_x itself is present, which is in excellent agreement with the presence of the intrinsic negative charges of P(VDF-TrFE) at the interface. On the other hands, for a positive corona charging exceeding the 2 kV, the charges of P(VDF-TrFE) turns into positive charges, repelling the holes which are minority carriers of n-type Si. Therefore, τ_{eff} increases by 7.2 ms at 12 kV corona charge. However, when the high corona voltages over 12 kV, the P(VDF-TrFE) films start to be damaged by high corona charges and the polarization of P(VDF-TrFE) is deteriorated. Vice versa, the strong negative charges can drive back the electrons which are minority carriers of p-Si and thus τ_{eff} of P(VDF-TrFE) covered p-Si is enhanced up to 7.55 ms at -12 kV of corona voltage. Interestingly, enhanced charges regardless of polarity may improve passivation effect to the Si. The recombinations are summation of recombination activity of interface states determined by electron recombination velocity and hole capture velocity. Since a recombination process causes the presence of both electrons and holes, lower recombination rates are achieved by reducing the number of one type of carriers at the surface by changing their ratio. Thus, for example, the positive charges at the interfaces of p-Si can lead to accumulation of electrons at the surface but simultaneously holes can stay away from the surface, leading to a reduction in recombination rates upon excitation.

The junction between PEDOT:PSS and n-Si were optimized before the integration of the P(VDF-TrFE) thin film to rear-side of PEDOT:PSS / Si solar cells (PSC). Interface engineering for the n-Si / PEDOT:PSS junction is also critical, which promotes carrier separation and improves performance. On the top side of Si surface was textured via black Si methods (detailed in supplementary information), demonstrating a very low reflection of ~ 3 % (Figure 45). After that, PEDOT:PSS layer is spin-coated on textured Si to form the junction. However, the nanotextured Si can hardly be fully coated by the PEDOT:PSS layer (Figure 46a), which is quite well-known issue in the field of PSC. The approach to resolve this issue is the use of ultra-thin Al_2O_3 layer which is also extensively used for tunneled passivation layer. Figure 47a shows the collected TEM image with native oxide layer grown during Al_2O_3 deposition at 130 °C, confirmed by EDS layered image and element mapping (Figure 47b-f). As expected, the ultra-thin Al_2O_3 layer results in an increase of the wettability, so that the PEDOT:PSS layers can be conformally coated on the textured Si (Figure 46b and 46c-e, respectively). The conformal coating increased built-in potential and effectively reduced the dark saturation current, leading to enhanced the photovoltaic parameters to an open circuit voltage (V_{oc}) of 612 mV from 574 mV, a short circuit current density (J_{sc}) of 34.79 mA cm^{-2} from 31.12 mA cm^{-2}, and FF of 62.7 % from 59.5%, which are corresponding to the PCE of 13.34 % from 10.62 %. (Figure 48 and Table 12).

However, this efficiency is not comparable to state-art-of hybrid solar cells which have PCE of ~ 17 %. Cui et al predicted that the theoretical PCE of PSC is up to 19.5% with complete passivation at the top and bottom side. Comparing our devices with predicted value, we found that there is significant Voc loss due to recombination at the un-passivated rear-side of Si. Therefore, as shown in Figure 49a, we fabricated the PSC with crystalline P(VDF-TrFE) as a back passivated layer. The pores in P(VDF-TrFE) layer can be the conducting paths of carriers from Si to bottom electrode and networked-structure can passivate the rest of bottom side Si, mimicking the PERC structure. Figure 50 shows the statistical distribution of the photovoltaic parameters for all devices. We observe that all parameters are increased with high reproducibility. Particularly, the Voc and FF are improved significantly by the polling process. The PCE of PEDOT:PSS / Si / P(VDF-TrFE) solar cells are improved to 16.53 %, with J_{sc} = 37.35 mA cm^{-2}, V_{oc} = 628 mV, and FF = 70.5 % due to reduced recombinations at the rear-side. Moreover, taking advantage of the ferroelectric property of P(VDF- TrFE), the device is poled with a voltage of + 20 V to repel the minority carriers. As a result, the polarization-induced passivation by P (VDF-TrFE) is enhanced at the surface while at the same time a strong electric field can form and penetrate to the Si. The overall photovoltaic parameters are enhanced and especially the V_{oc} is increased up to 641 mV. After poling, the PCE of the champion device of PSC with P(VDF-TrFE) is increased to 18.11 % (Figure 49b), which is record-breaking efficiency among the heterojuntion solar cells based on the interface between Si and PEDOT:PSS. The photovoltaic parameters of the devices are summarized in the Table 13. The external quantum efficiency (EQE) spectrum of the devices clearly shows the effect of the P(VDF-TrFE). At wavelengths above 800 nm, the EQE loss mainly occurs due to recombination on the rear-side of Si. The P (VDF-TrFE) can significantly prevent recombinations, resulting in higher EQE at longer wavelengths (Figure 49c). The mechanism of the back surface field due to poled P(VDF-TrFE) layer was elucidated via FDTD simulation. The geometry was defined as the PEDOT:PSS / Si / P(VDF-TrFE) in this simulation is shown in Figure 49d, featuring island-shaped ferroelectric layers inserted between Si and electrodes. Moreover, the calculations were performed taking advantages of the equations from several works. The positively charged P(VDF-TrFE) strongly reflect the holes from the rear-side of Si. Therefore, electric potential beneath the ferroelectric islands appears to be negative, corresponding to a reduction in the concentration of holes. To understand the effect of the porous ferroelectric thin film more clearly, the line scan of the electric potential of Si is shown in Figure 49e. At the interface of PEODT:PSS and Si, the highly positive electric potential are presented because a large number of holes are generated. On the other hands, at the rear side, the holes are repelled and electrons can easily approach the bottom electrodes due to the electric field of the P(VDF-TrFE), representing the negative potential. This electric field from positively poled P(VDF-TrFE) is anticipated to promote downward band-bending inside the silicon, drawing electrons to the surface and repelling the holes, consequently preventing recombination as illustrated schematically in Figure 49f.

The ambipolar P(VDF-TrFE) thin films can be also applicable to the passivated BSF layer for p-Si solar cells. The porous and crystalline P(VDF-TrFE) thin films were integrated into the complete p-type Si homojunction solar cells (HSC) as schematically depicted in Figure 50a. The current-voltage (J–V) photovoltaic characteristic curves under 1-sun illumination are shown in Figure 51b for HSC with and without porous P(VDF-TrFE) thin films. The detailed photovoltaic parameters of all the cells are given in Table 14. Moreover, the box plot of Jsc, Voc, FF and the efficiency of six solar cells has a fairly narrow distribution, indicating that this fabrication process is fairly reproducible (Figure 52). As expected from the measurement of effective lifetime, the insertion of P(VDF-TrFE) suppresses recombination at the surface of Si thus the HSC with P(VDF-TrFE) exhibited J_{sc} = 36.90 mA cm^{-2}, V_{oc} = 587 mV, and FF =74.0 %, yielding a PCE of 16.02 %. As already shown in Figure 44f, the negative charged P(VDF-TrFE) is much effective for p-type Si solar cells. Thus, upon [-] poling of 20 V, the PCE of HSC with P(VDF-TrFE) enhanced to 17.08 %, with J_{sc} = 37.75 mA cm^{-2}, V_{oc} = 598 mV, and FF =75.7 %. The electric field forming the back surface field can penetrate the surface of Si and modifies the surface carrier concentration, resulting in reduced recombinations and reflection of minority carriers. It is worth mentioning that the performance of HSC with P(VDF-TrFE) is superior to HSC with aluminum (Al) BSF which is the common strategy to enhance the performance of p-Si solar cells (Figure 53). The Al BSF is achieved by high-temperature with in-diffusion of a high concentration of dopants to the back surface of Si, forming an additional electric field. However, the rear recombination is also severely increased at the interface between fully covered Al contact and Si. In contrast, the porosity of P(VDF-TrFE) thin film is around ~ 5 % and thus the bottom electrodes are locally contacted to the Si like the local point contact in PERC (passivated emitter rear cell), minimizing contact recombination. Moreover, the stability and reliability of P(VDF-TrFE) were also demonstrated (Figure 51c). P (VDF-TrFE) itself is chemically stable but susceptible to humidity. However, when incorporating a P (VDF-TrFE) layer into the device, the layer was protected by the deposited bottom electrode. Therefore, the passivation effect by SiO_x / P(VDF-TrFE) is sustained in 1000 hours of damp heat test while maintaining 95% of its initial performance. Furthermore, the poling effect of P(VDF-TrFE) is also stable for 1000 hours of damp heat test, and there is no significant difference in the performance. This behavior might be related to the fact P(VDF-TrFE) have a relatively high curie temperature of 110^{o}C and the charges from covered electrodes prevent deterioration of polarization.

5.4 Conclusion

The porous and self-assembled P(VDF-TrFE) thin films are fabricated by a simple spin-coating process with the use of nitric acid in the water as an additive in the solution. The GIXD measurement reveals the extraordinary excellent crystallinity of the porous P(VDF-TrFE) thin films. More importantly, During the spin-coating on Si substrate and subsequent annealing process, the high-quality of SiO_2 is formed on the top of Si and underneath of crystalline P(VDF-TrFE) thin-film, unlike continuous films. The combination of SiO2 and crystalline P(VDF-TrFE) films provide excellent passivation property to both n-and p-type Si. In addition, the passivation effect from the P(VDF-TrFE) can be manipulated in a direction to maximize the carrier lifetime of the wafer by controlling the electric field due to its ferroelectric properties. Therefore, the P(VDF-TrFE) thin films are utilized as passivated back surface field layers to both n-and p-type solar cells. For PEDOT:PSS/n-Si solar cells, such devices demonstrate record-breaking photovoltaic conversion efficiency of 18.1% with electrostatic passivation and reflection of minority carriers by the induced built-in electric field. Furthermore, the performance of the p-type homojunction solar cells with P(VDF-TrFE) is superior to that of the cells based on Al-BSF. The P(VDF-TrFE) passivated back surface field layer was also found to be maintained under high relative humidity (85%) at 85 ^oC for over 1000 h. This work can open up the possibility of organic / Si solar cells with new passivation techniques in an inexpensive and simple way beyond traditional Si photovoltaics with inorganics.

5.5 References

1. McKone, J. R., et al. Evaluation of Pt, Ni, and Ni-Mo electrocatalysts for hydrogen evolution on crystalline Si electrodes. Energy & Environmental Science 4, 3573-3583 (2011).

2. Nomura, K., et al. Room-temperature fabrication of transparent flexible thin-film transistors using amorphous oxide semiconductors. Nature 432, 488-492 (2004).

3. Tian, B. Z., et al. Coaxial silicon nanowires as solar cells and nanoelectronic power sources. Nature 449, 885-U888 (2007).

4. Xu, Q. F., et al. Micrometre-scale silicon electro-optic modulator. Nature 435, 325-327 (2005).

5. Glunz, S. W., et al. Field-effect passivation of the SiO2-Si interface. Journal of Applied Physics 86, 683-691 (1999).

6. Hoex, B., et al. Silicon surface passivation by atomic layer deposited Al(2)O(3). Journal of Applied Physics 104, 044903, (2008).

7. Kayes, B. M., et al. Comparison of the device physics principles of planar and radial p-n junction nanorod solar cells. Journal of Applied Physics 97,114302 (2005).

8. Yoshikawa, K., et al. Silicon heterojunction solar cell with interdigitated back contacts for a photoconversion efficiency over 26%. Nature Energy 2,17032 (2017).

9. Fossum, J. G. PHYSICAL OPERATION OF BACK-SURFACE-FIELD SILICON SOLAR-CELLS. Ieee Transactions on Electron Devices 24, 322-325 (1977).

10. Goodrich, A., et al. A wafer-based monocrystalline silicon photovoltaics road map: Utilizing known technology improvement opportunities for further reductions in manufacturing costs. Solar Energy Materials and Solar Cells 114, 110-135 (2013).

11. Grant, N. E., et al. Thermal activation and deactivation of grown-in defects limiting the lifetime of float-zone silicon. Phys Status Solidi-R 10, 443-447 (2016).

12. Jackson, W. B., et al. Effect of Temperature during Illumination on Annealing of Metastable Dangling Bonds in Hydrogenated Amorphous-Silicon. Appl Phys Lett 49, 957-959 (1986).

13. Bender, H., et al. Hydrogen Passivation of Hf-Last Cleaned (100)Silicon Surfaces Investigated by Multiple Internal-Reflection Infrared-Spectroscopy. J Electrochem Soc 141, 3128-3136 (1994).

14. De Wolf, S., et al. Surface passivation properties of boron-doped plasma-enhanced chemical vapor deposited hydrogenated amorphous silicon films on p-type crystalline Si substrates. Appl Phys Lett 88, 022104 (2006).

15. Msaad, H., et al. Electronic Passivation of Silicon Surfaces by Halogens. J Electron Mater 23, 487-491 (1994).

16. Agostinelli, G., et al. Very low surface recombination velocities on p-type silicon wafers passivated with a dielectric with fixed negative charge. Solar Energy Materials and Solar Cells 90, 3438-3443 (2006).

17. Hoex, B., et al. Excellent passivation of highly doped p-type Si surfaces by the negative-charge-dielectric Al2O3. Appl Phys Lett 91, 112107 (2007).

18. Kamal, H., et al. Influence of the Recombination Parameters at the Si/SiO2 Interface on the Ideality of the Dark Current of High Efficiency Silicon Solar Cells. J Semicond Tech Sci 15, 232-242 (2015).

19. Lauinger, T., et al. Record low surface recombination velocities on 1 Omega cm p-silicon using remote plasma silicon nitride passivation. Appl Phys Lett 68, 1232-1234 (1996).

20. Wan, Y. M., et al. Zirconium oxide surface passivation of crystalline silicon. Appl Phys Lett 112, 201604 (2018).

21. Wan, Y. M., et al. Tantalum Oxide Electron-Selective Heterocontacts for Silicon Photovoltaics and Photoelectrochemical Water Reduction. Acs Energy Lett 3, 125-131 (2018).

22. Green, M. A. The Passivated Emitter and Rear Cell (PERC): From conception to mass production. Solar Energy Materials and Solar Cells 143, 190-197 (2015).

23. Masuko, K., et al. Achievement of More Than 25% Conversion Efficiency With Crystalline Silicon Heterojunction Solar Cell. Ieee J Photovolt 4, 1433-1435 (2014).

24. Schmidt, J., et al. Surface passivation of high-efficiency silicon solar cells by atomic-layer-deposited Al2O3. Progress in Photovoltaics 16, 461-466 (2008).

25. Wang, Z. J., et al. Advanced PERC and PERL production cells with 20.3% record efficiency for standard commercial p-type silicon wafers. Progress in Photovoltaics 20, 260-268 (2012).

26. Dingemans, G., et al. Influence of annealing and Al2O3 properties on the hydrogen-induced passivation of the Si/SiO2 interface. Journal of Applied Physics 111, 093713 (2012).

27. Simoen, E., et al. Impact of Forming Gas Annealing and Firing on the Al2O3/p-Si Interface State Spectrum. Electrochem Solid St 14, H362-H364 (2011).

28. Bullock, J., et al. Superacid Passivation of Crystalline Silicon Surfaces. ACS applied materials & interfaces 8, 24205-24211 (2016).

29. Chen, J., et al. Vacuum-Free, Room-Temperature Organic Passivation of Silicon: Toward Very Low Recombination of Micro-/Nanotextured Surface Structures. ACS applied materials & interfaces 10, 44890-44896 (2018).

30. Chen, J. H., et al. Electrochemical grafting passivation of silicon via electron transfer at polymer/silicon hybrid interface. Electrochim Acta 247, 826-834 (2017).

31. Ji, W., et al. Dip Coating Passivation of Crystalline Silicon by Lewis Acids. ACS nano 13, 3723-3729 (2019).

32. Avasthi, S., et al. Role of Majority and Minority Carrier Barriers Silicon/Organic Hybrid Heterojunction Solar Cells. Adv Mater 23, 5762 (2011).

33. Kang, S. B., et al. Self-assembled, highly crystalline porous ferroelectric poly(vinylidene fluoride-co-trifluoroethylene) interlayer for Si/organic hybrid solar cells. Nano Energy 41, 243-250 (2017).

34. Khang, D. Y. Recent progress in Si-PEDOT:PSS inorganic organic hybrid solar cells. J Phys D Appl Phys 52, 503002 (2019).

35. He, J., et al. Silicon/Organic Hybrid Solar Cells with 16.2% Efficiency and Improved Stability by Formation of Conformal Heterojunction Coating and Moisture-Resistant Capping Layer. Adv Mater 29, 1606321 (2017).

36. He, J., et al. 16% efficient silicon/organic heterojunction solar cells using narrow band-gap conjugated polyelectrolytes based low resistance electron-selective contacts. Nano Energy 43, 117-123 (2018).

37. Yang, Z., et al. Tuning of the Contact Properties for High-Efficiency Si/PEDOT:PSS Heterojunction Solar Cells. Acs Energy Lett 2, 556-562 (2017).

38. Yoon, S.-S., et al. High Efficiency (>17%) Si-Organic Hybrid Solar Cells by Simultaneous Structural, Electrical, and Interfacial Engineering via Low-Temperature Processes. Advanced Energy Materials 8, 1702655 (2018).

39. Zhang, X., et al. Improved PEDOT:PSS/c-Si hybrid solar cell using inverted structure and effective passivation. Scientific reports 6, 35091 (2016).

40. Zielke, D., et al. Organic-silicon Solar Cells Exceeding 20% Efficiency. Energy Procedia 77, 331-339 (2015).

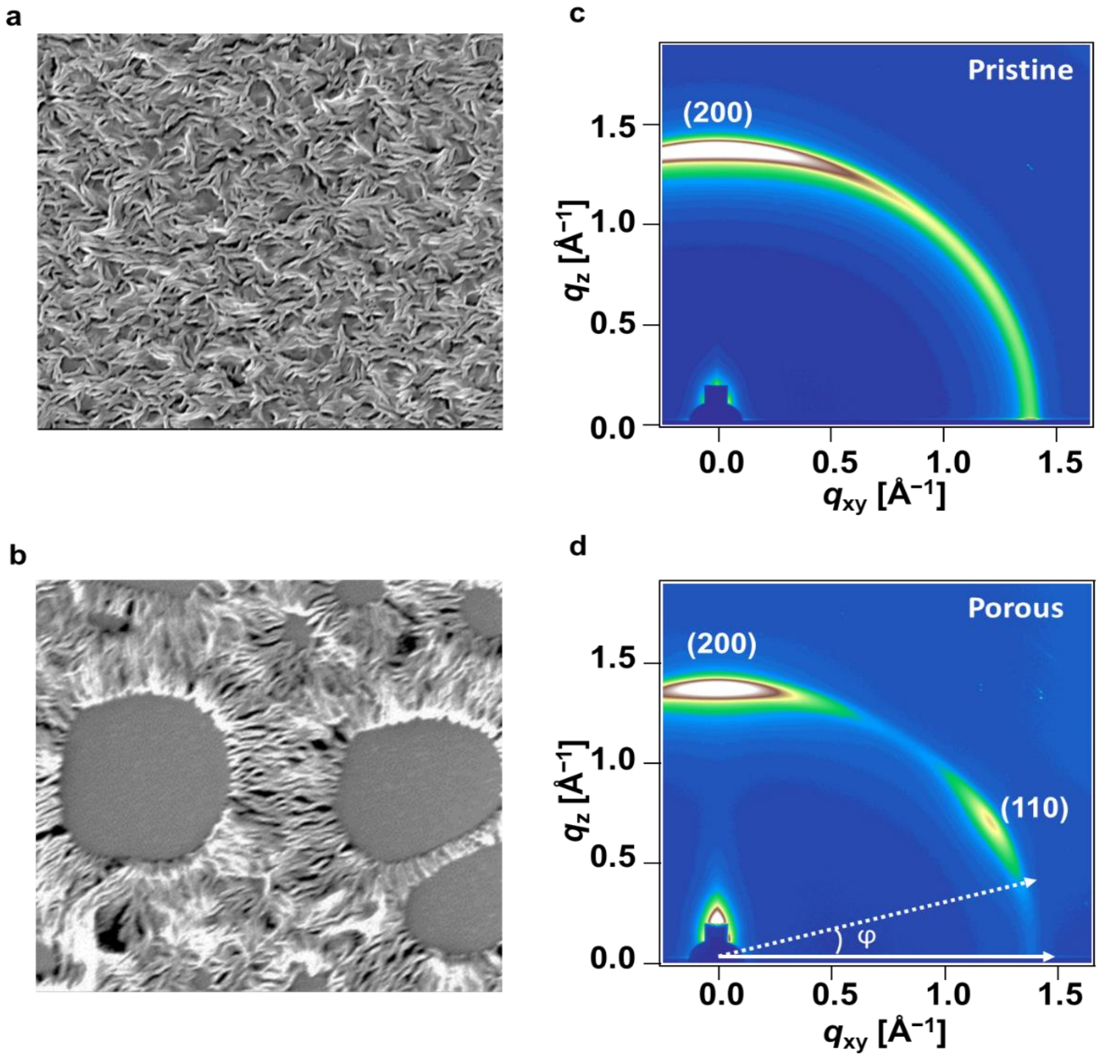

Figure 38. SEM images of (a) smooth and (b) porous PVDF-TrFE thin films on textured Si substrates thermally annealed at 135 °C for 4 hours. 2D GIXD patterns of (c) smooth and (d) porous PVDF-TrFE thin films. The crystalline nature of the PVDF-TrFE films exhibited 2D diffraction patterns where a reflection intensified at the meridian regions on the patterns corresponding to either (110) or (200).

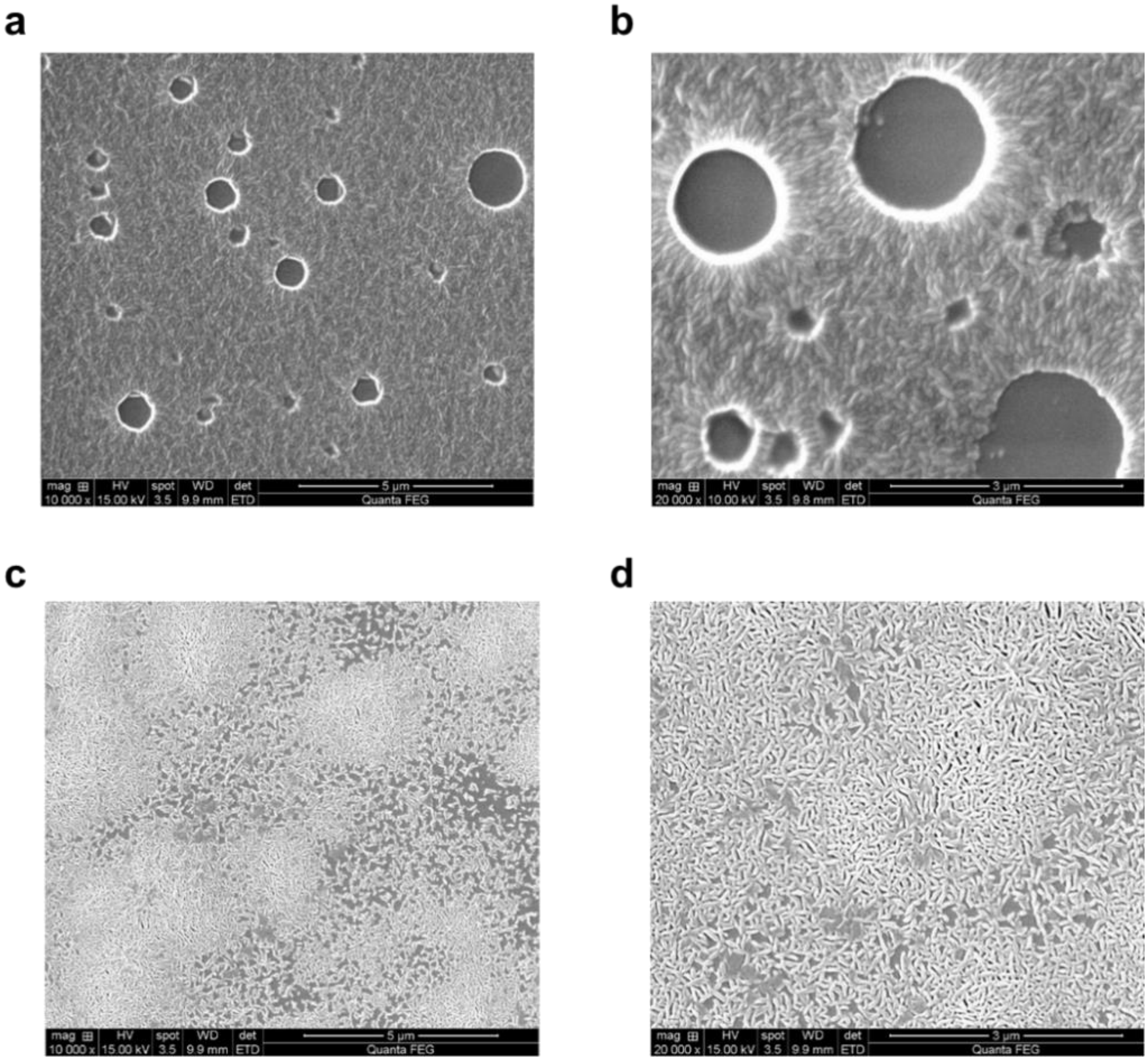

Figure 39. SEM images of diffrent porous p(VDF-TrFE) thin films prepared by solution of P(VDF-TrFE) in (a,b) DMF and (c,d) DMSO with addition of deionized water.

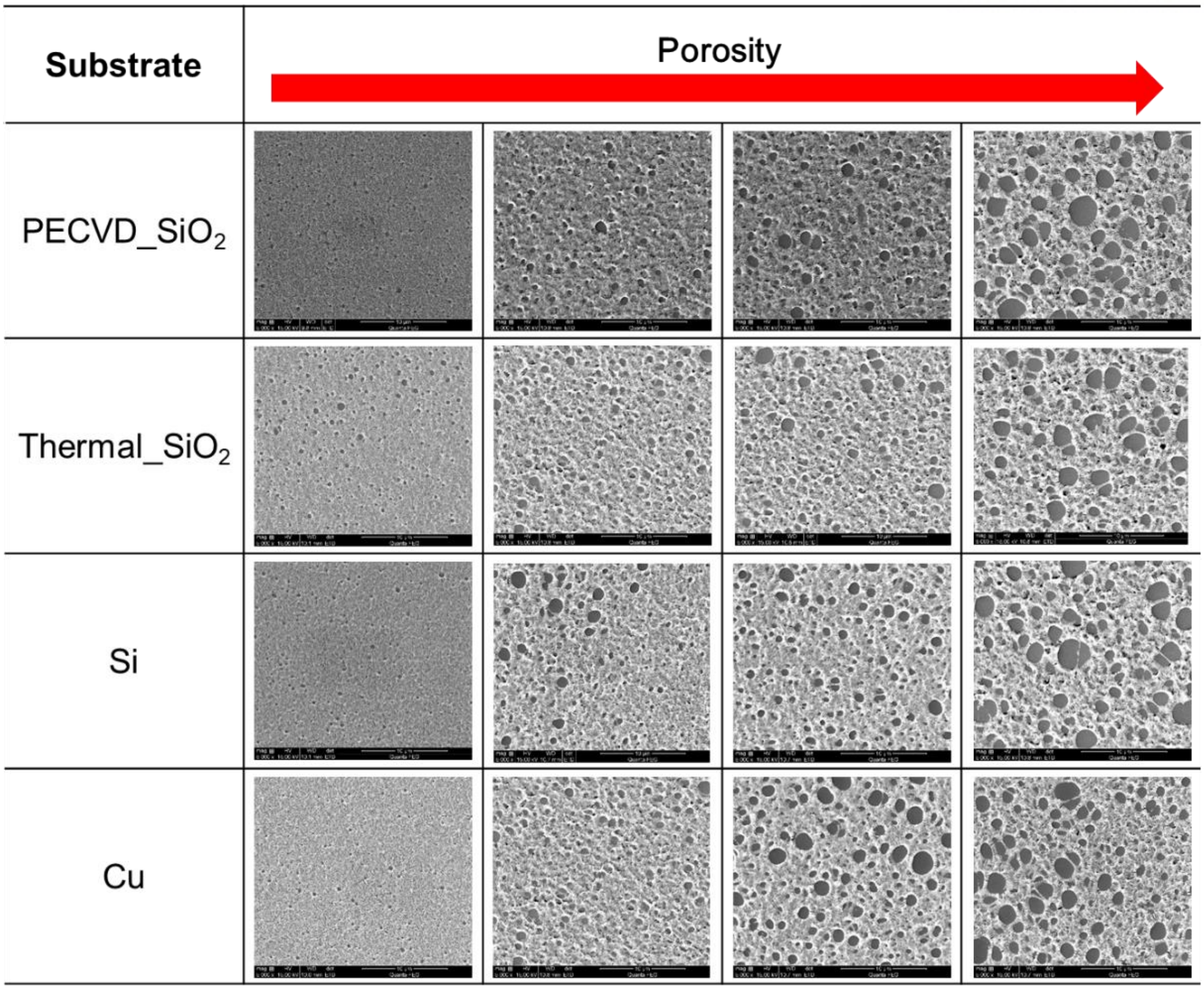

Figure 40. SEM images of diffrent porous P(VDF-TrFE) thin films prepared on the various substrate.

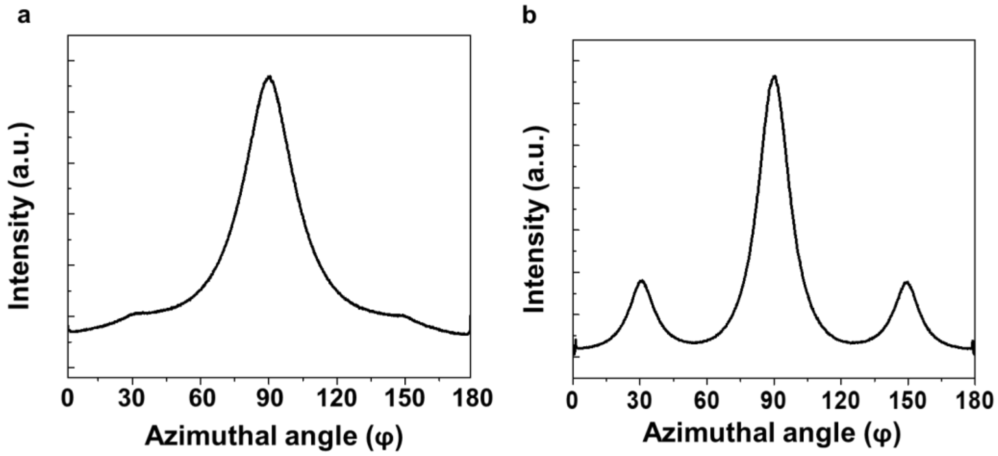

Figure 41. Equatorial azimuthal intensity profiles of (a) pristine and (b) porous and crystalline P(VDF-TrFE) thin films..

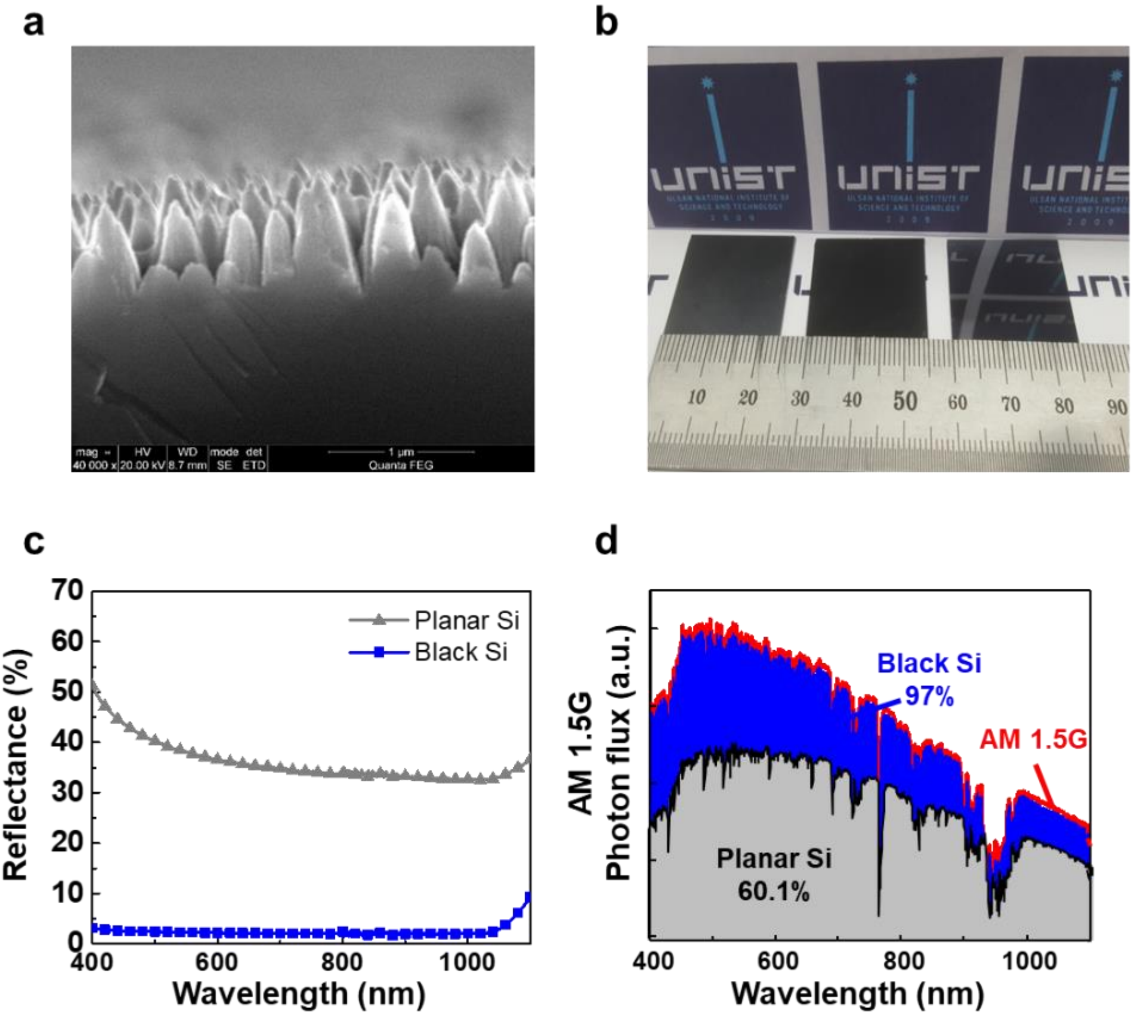

Figure 42. (a) SEM image of the Si nano structure arrays in black Si. (b) Optical images of black and planar Si. (c) Total reflectance spectra of planar Si (gray sold line) and black Si (blue solid line) (d) Spectral distribution of absorbed photons of planar Si (gray), black Si (blue), and AM 1.5G spectrum (red).

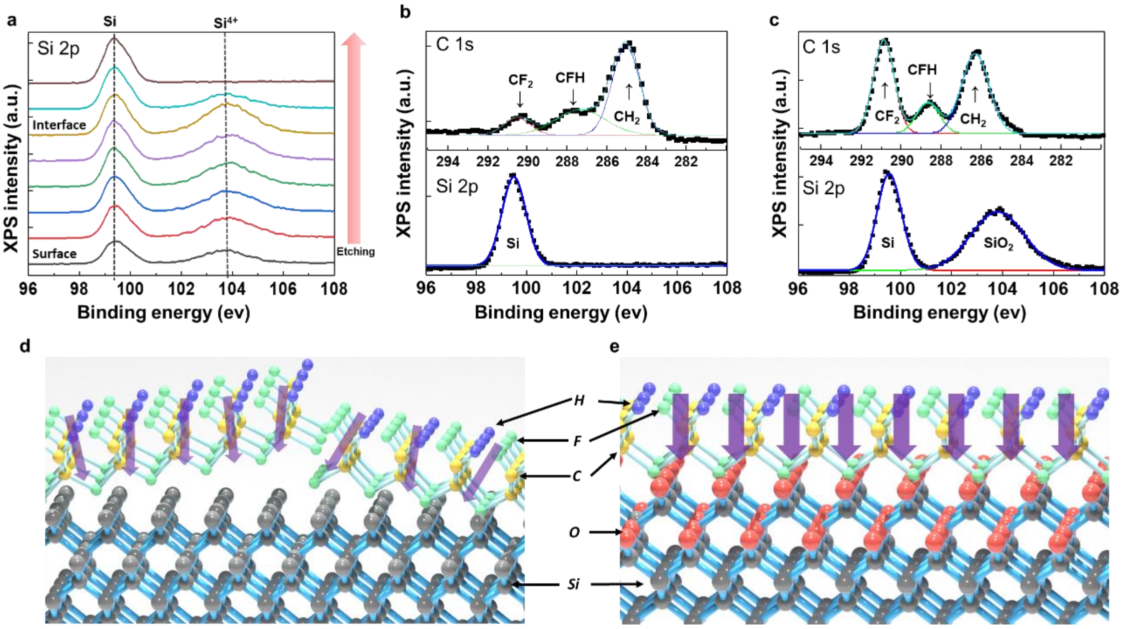

Figure 43. (a) Changes of Si 2p XPS spectra of crystalline P(VDF-TrFE)/Si during etching. The Si 2p and C 1s XPS spectra at the interface of (b) continuous P(VDF-TrFE)/Si and (c) Crystalline P(VDF-TrFE) /Si. Schematic representation of the interfaces of (d) continuous P(VDF-TrFE)/Si and (e) crystalline P(VDF-TrFE)/Si. the violet arrows indicate the magnitude and direction of polarization (Each colored ball represented each atom; black: Silicon, red: Oxygen, Yellow: carbon, green: fluorine and blue: Hydrogen).

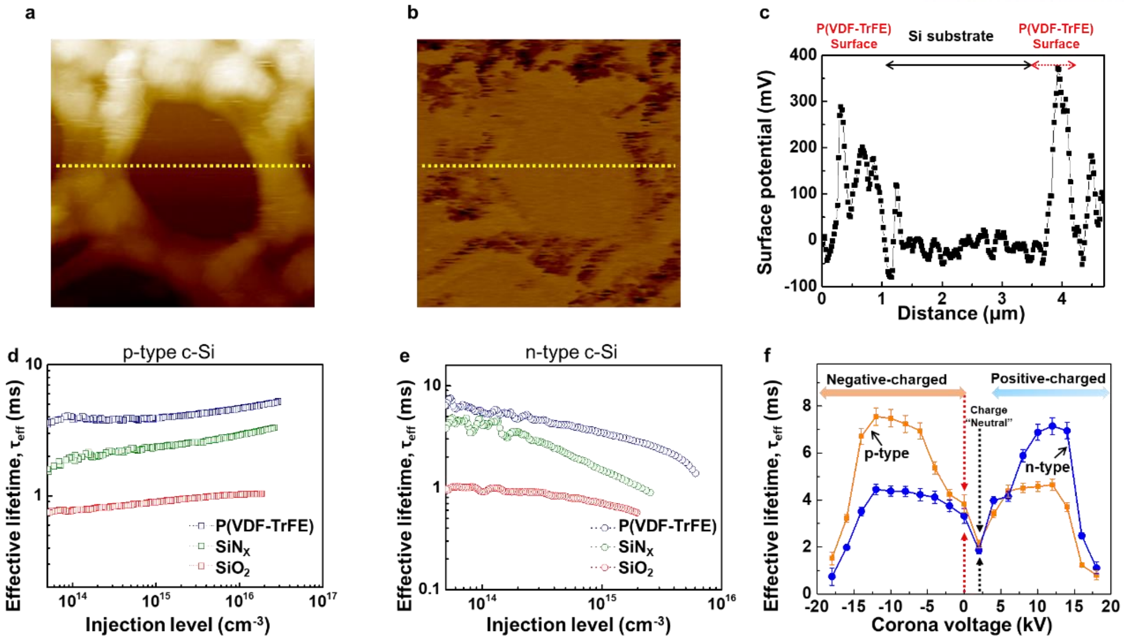

Figure 44. (a) Topography and (b) surface potential distribution of the porous P(VDF-TrFE) coated Si substrate. (c) line scan of (b). The effective lifetime as function of injection level were measured on (d) p-type (Doping concentration of 7.8 $\times 10^{14}$ cm^{-3}) and (e) n-type (Doping concentration of 8.5 $\times 10^{15}$ cm^{-3}) c-Si wafers passivated by the P(VDF-TrFE). SiN_x and SiO_2 (f) The ambipolar property of P(VDF-TrFE) thin films; Dependence of the effective lifetime of n- and p-type Si wafer (@ injection level of 1 x 10^{15} cm^{-3}) on corona voltages

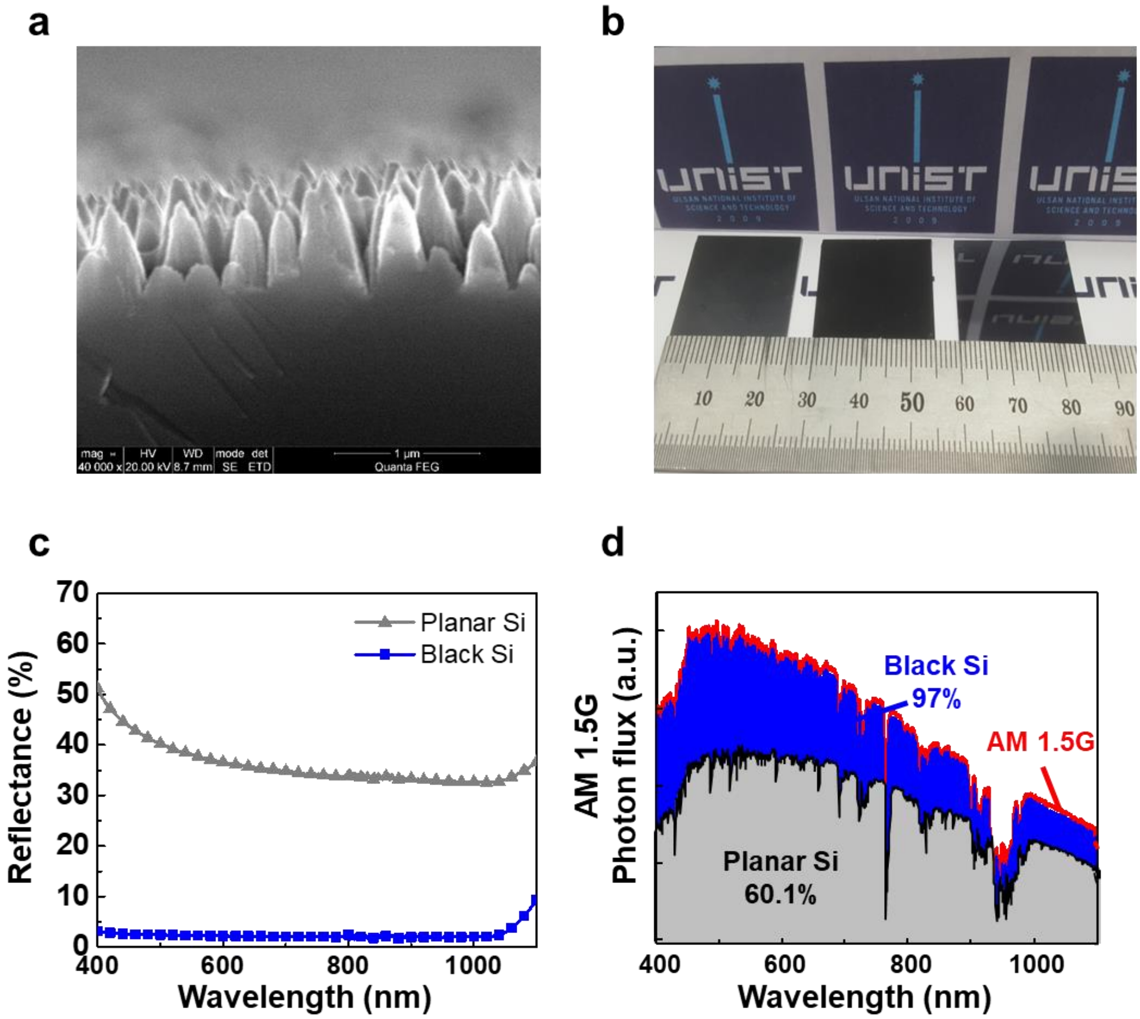

Figure 45. (a) SEM image of the Si nano structure arrays in black Si. (b) Optical images of black and planar Si. (c) Total reflectance spectra of planar Si (gray sold line) and black Si (blue solid line) (d) Spectral distribution of absorbed photons of planar Si (gray), black Si (blue), and AM 1.5G spectrum (red).

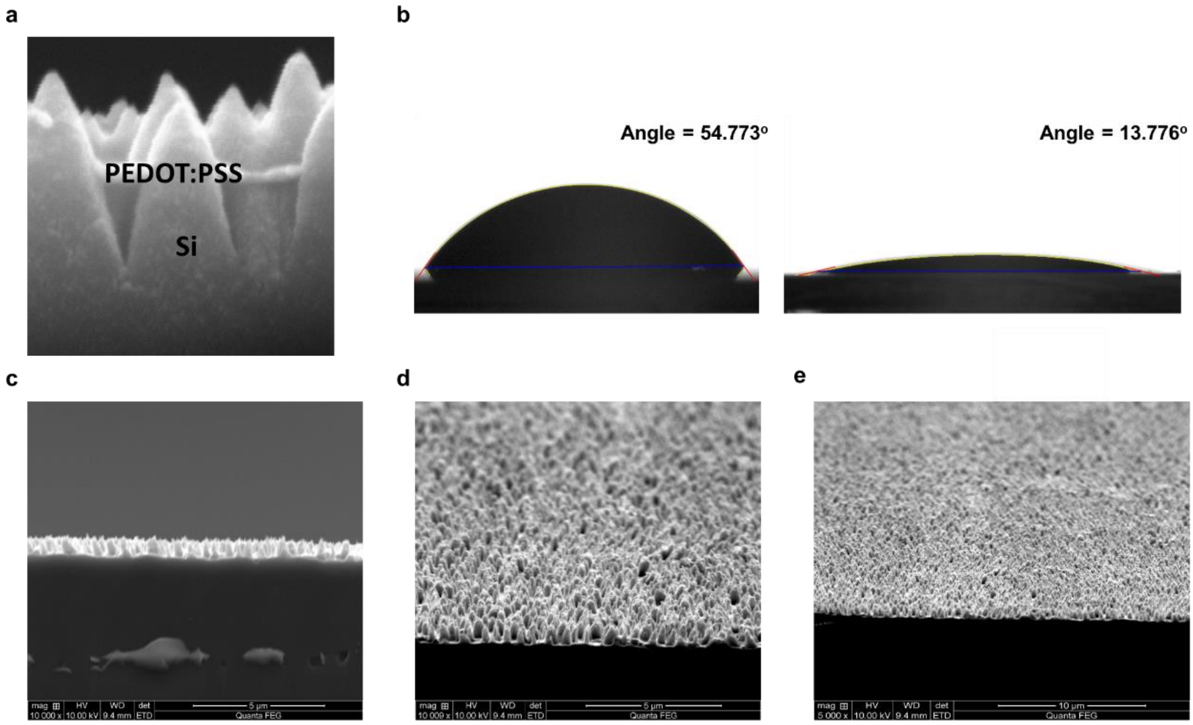

Figure 46. (a) PEDOT:PSS coated on black Si without Al_2O_3, The PEDOT:PSS is partially coated on the Si. (b) The contact angle measurement of the black Si and (b) Al_2O_3 coated on black Si by using IPA-diluted PEDOT:PSS, exhibiting the angle of 54.773^o and 13.776^o, respectively. SEM micrograph of conformally coated PEDOT:PSS on Al_2O_3/black Si: (c) cross section (d) high and (e) low magnitude.

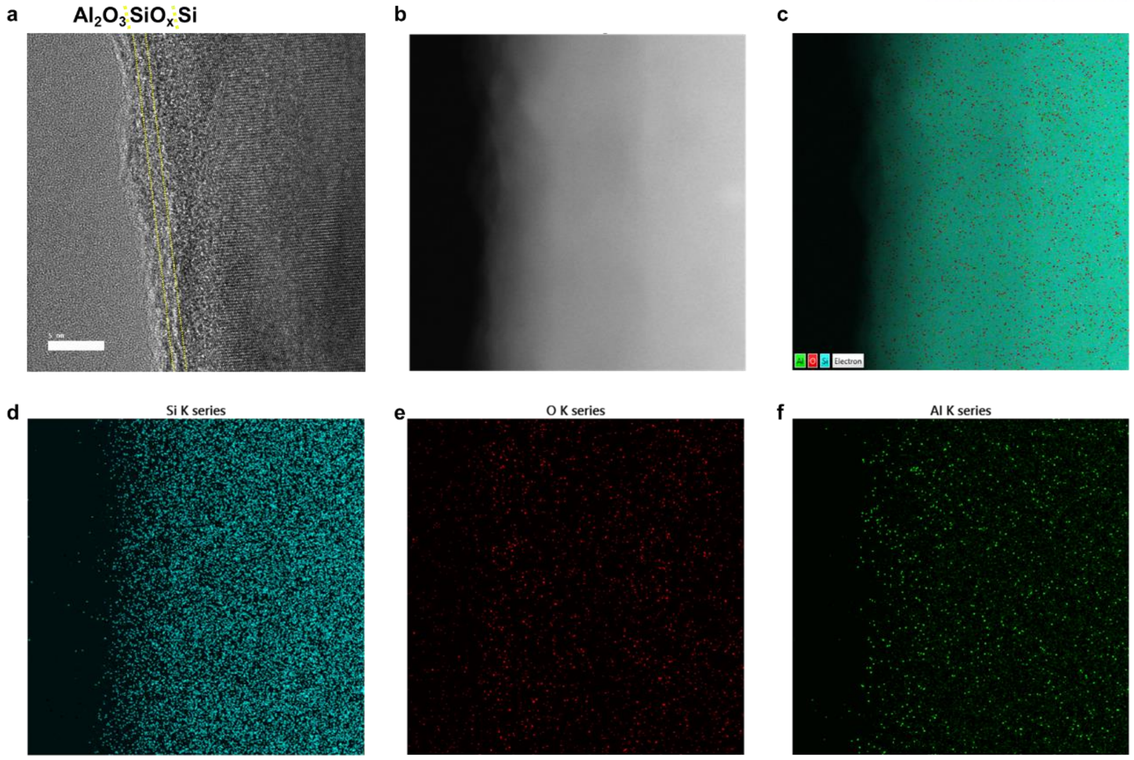

Figure 47. (a) High resolution TEM image and (b) electron image. (c) EDS layered image and element mapping (d-f) images of Al_2O_3 coated Si nanowire.

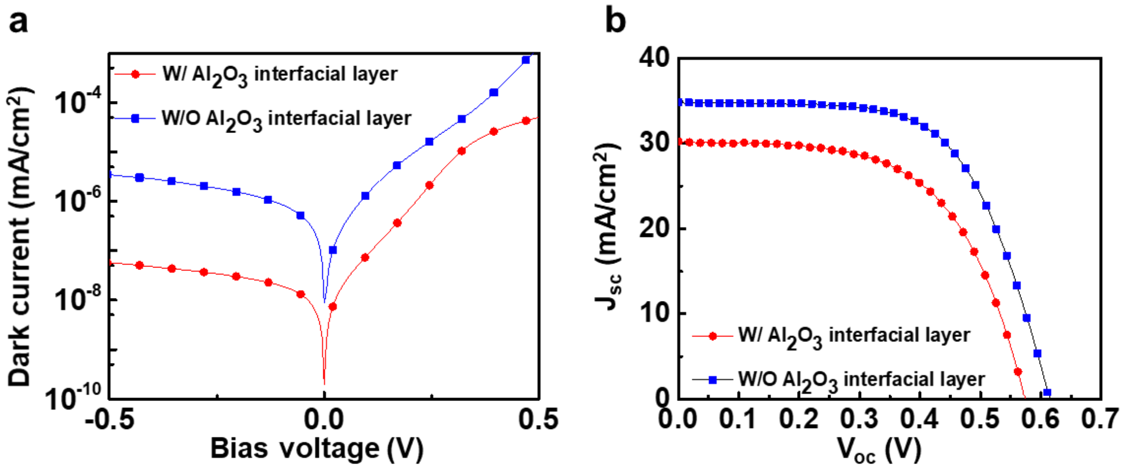

Figure 48. J-V characteristics of the PEDOT:PSS / black Si devices (a) under dark and (b) 1 sun illumination with and without a Al_2O_3 interfacial layer.

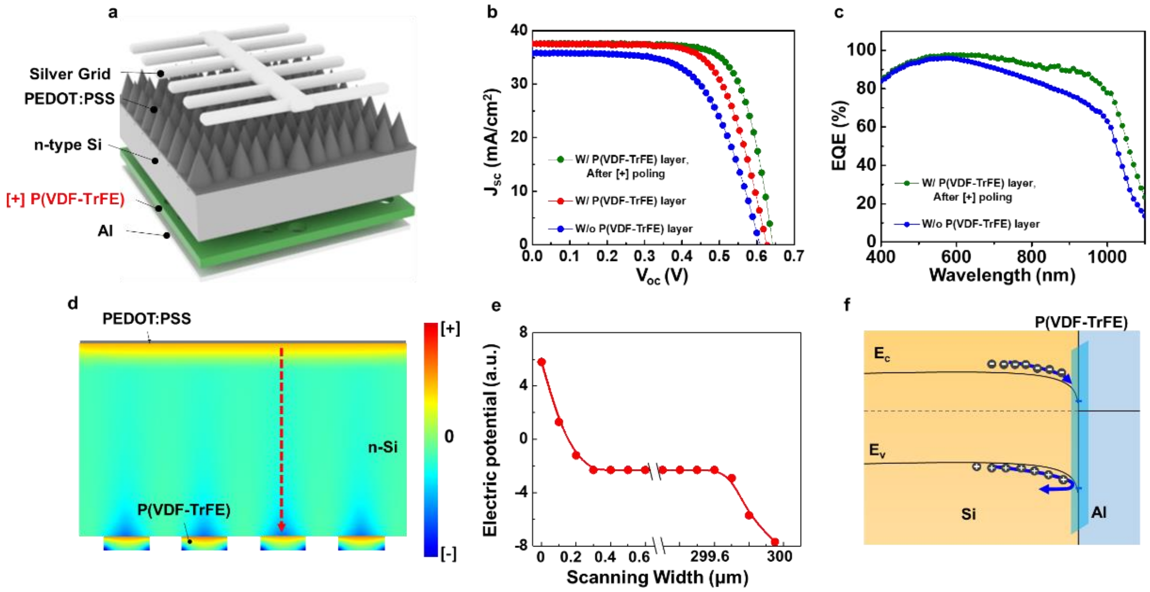

Figure 49. (a) Schematic illustration of a PSC with P(VDF-TrFE). (b) Light J−V curves of devices without a porous P(VDF-TrFE) layer (green), with porous P(VDF-TrFE) layer (red) and after [+] poling (green). (c) Measured EQE spectra of the solar cell with and without porous P(VDF-TrFE). (d) FDTD electric potential simulation for device (not to scale) and (e) line scans along red arrow. (f) Schematic of the energy band diagram of a contact with P(VDF-TrFE) thin film.

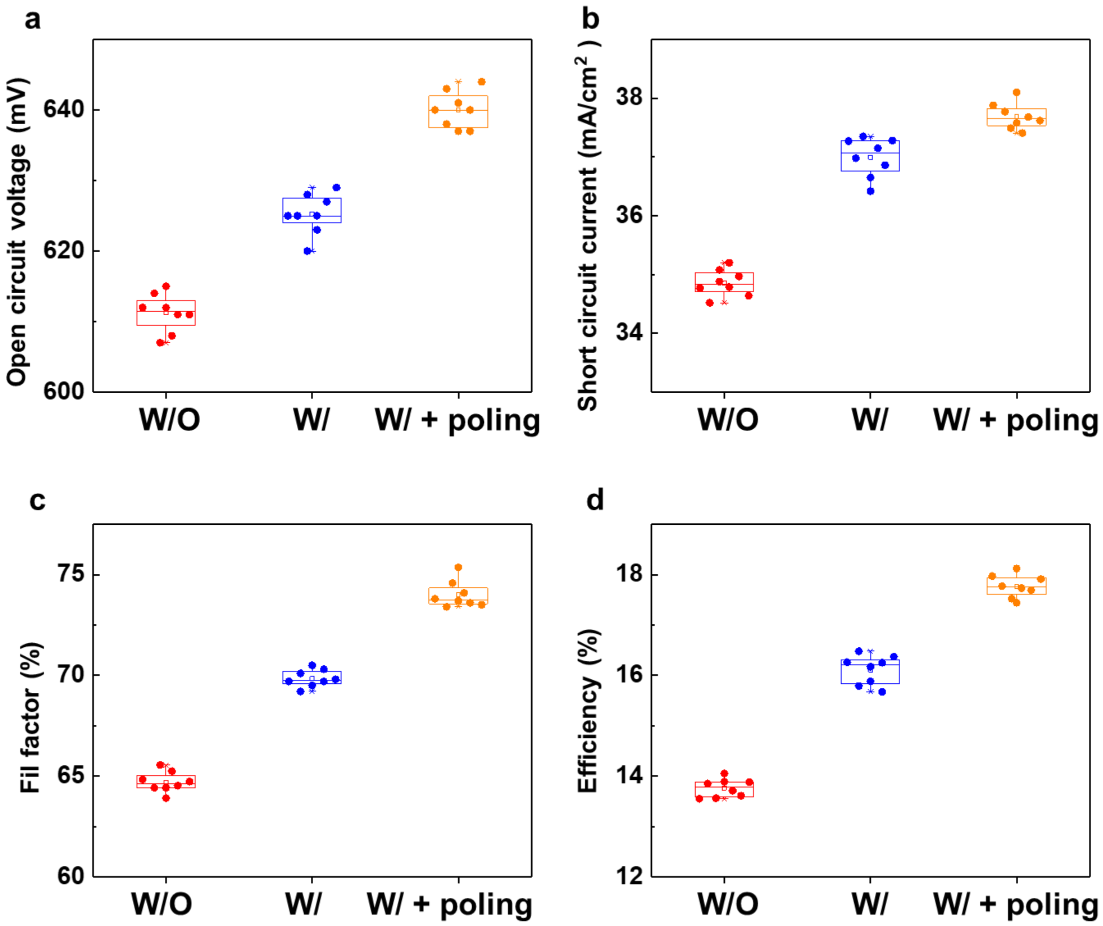

Figure 50. Statistical Distribution of the Photovoltaic Parameters for PSC without P(VDF-TrFE), with P(VDF-TrFE), and with P(VDF-TrFE) after poling. (a–d) Dependence of (a) Voc, (b) Jsc, (C) FF, and (D) efficiency

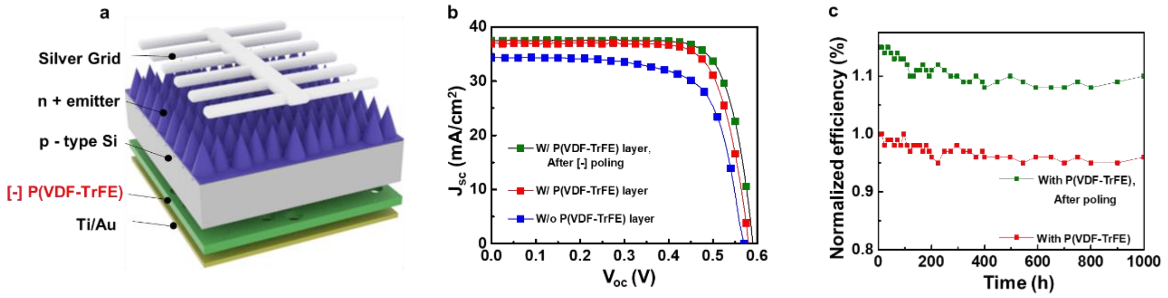

Figure 51. (a) Schematic illustration of HSC with P(VDF-TrFE). (b) Light J−V curves of devices without a porous P(VDF-TrFE) layer (green), with porous P(VDF-TrFE) layer (red) and after [-] poling (green). (c) Thermal and humidly stability of the HSP solar cells. The relative change in efficiencies (with P(VDF-TrFE), with P(VDF-TrFE) after poling) are plotted as function of damp heat test time.

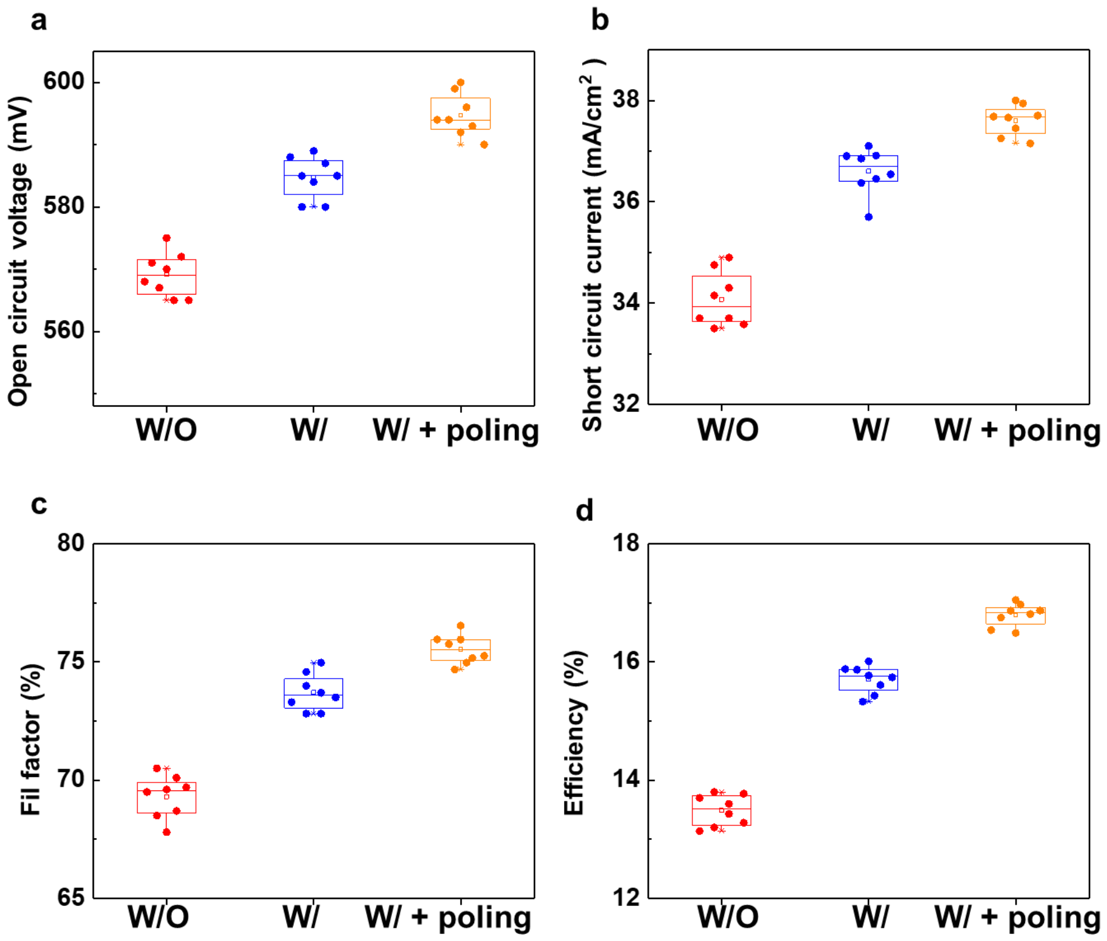

Figure 52. Statistical Distribution of the Photovoltaic Parameters for HSC without P(VDF-TrFE), with P(VDF-TrFE), and with P(VDF-TrFE) after poling. (a–d) Dependence of (a) Voc, (b) Jsc, (C) FF, and (D) efficiency

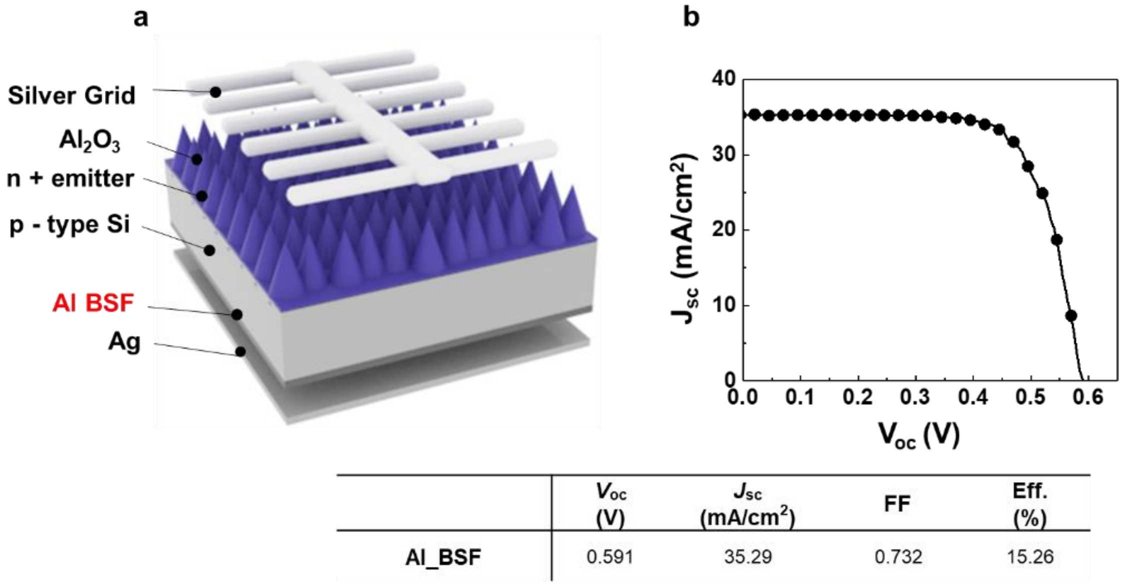

	V_{oc} (V)	J_{sc} (mA/cm^2)	FF	Eff. (%)
Al_BSF	0.591	35.29	0.732	15.26

Figure 53. (a) the schematic of HSC with Al _BSF. (b) Light J-V characteristics of the device.

Table 12. J-V characteristics of planar n-PSP solar cells with and without **Al_2O_3** layer.

Al_2O_3	V_{oc} (V)	J_{sc} (mA/cm^2)	FF	Eff. (%)
W / O	0.574	31.12	0.595	10.62
W	0.612	35.76	0.627	13.72

Table 13. Previous reports on high performance PEDOT:PSS / Si solar cells (V_{oc} > 600 mV)

Rear-surface	V_{oc} (mV)	J_{sc} (mA/cm^2)	FF	Eff. (%)	ref
PTB7-NBr	638	32.8	76.5	16.00	36
a-Si:H	634	35.4	72.2	16.21	37
Siloxane	610	38.41	74.0	17.34	38
a-Si:H	634	36.5	70.0	16.20	35
P(VDF-TrFE)	641	37.58	75.2	**18.11**	**This work**

Table 14. J-V characteristics of PSC solar cells with and without P(VDF-TrFE) layer. (Values in the brackets are average photovoltaic performance from the 6 devices.)

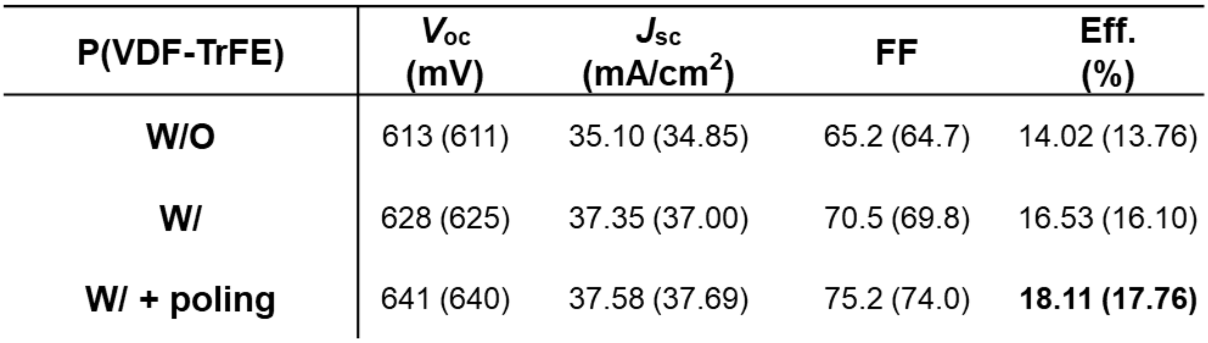

P(VDF-TrFE)	V_{oc} (mV)	J_{sc} (mA/cm^2)	FF	Eff. (%)
W/O	613 (611)	35.10 (34.85)	65.2 (64.7)	14.02 (13.76)
W/	628 (625)	37.35 (37.00)	70.5 (69.8)	16.53 (16.10)
W/ + poling	641 (640)	37.58 (37.69)	75.2 (74.0)	**18.11 (17.76)**

Table 15. J-V characteristics of HSC solar cells with and without P(VDF-TrFE) layer. (Values in the brackets are average photovoltaic performance from the 6 devices.)

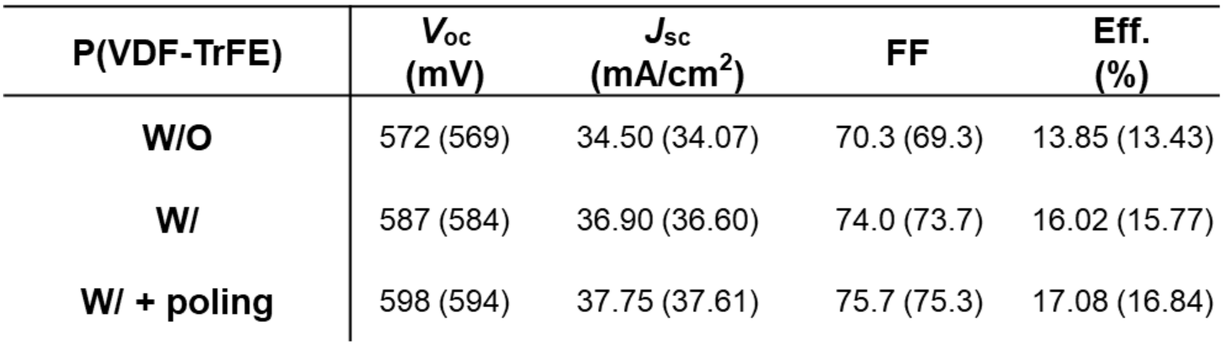

P(VDF-TrFE)	V_{oc} (mV)	J_{sc} (mA/cm^2)	FF	Eff. (%)
W/O	572 (569)	34.50 (34.07)	70.3 (69.3)	13.85 (13.43)
W/	587 (584)	36.90 (36.60)	74.0 (73.7)	16.02 (15.77)
W/ + poling	598 (594)	37.75 (37.61)	75.7 (75.3)	17.08 (16.84)

Sung Bum Kang

Ph.D. candidate | Department of Materials Science and Engineering

Ulsan National Institute of Science and Technology (UNIST), Ulsan 44919, Korea

Room # 410, 102-dong, UNIST-gil 50, Ulsan, Korea
sbkang@unist.ac.kr, phone: +82 10 3668 9707

RESEARCH STATEMENT

By training I am a material / chemical scientist and engineer working at the nano/microfabrication, interfaces and their manipulation based on experimental and theoretical method. Broadly stated, my work is directed towards developing organic/inorganic hybrid heterojunctions and functionalized nanostructures for photovoltaic devices, piezo/tribo energy harvester and sensor.

Education

Sep 2014 – Feb 2020	Ulsan National Institute of Science and Technology (UNIST), Korea M.S. combined Ph.D Course in Materials Science and Engineering Advisor: Professor Kyoung Jin Choi
Mar 2011 – Aug 2014	Ulsan National Institute of Science and Technology (UNIST), Korea B.S. in Energy Engineering, B.S in Materials Science & Engineering

Awards / Honors / Memberships

2018 **Best oral presentation award**

The Korea System of Materials (KSM)

2017 **Best poster presentation award**

The Korea Institute of Electrical and Electronic materials engineers (KIEEME)

2015 **Best oral presentation award**

The Korea Institute of Electrical and Electronic materials engineers (KIEEME)

2013 **Best undergraduate research award**

Ulsan National Institute of Science and Technology (UNIST)

Technical Skills (Self-operating)

Scanning Electron Microscope

Printing techniques (Electrospinning, dispenser, FDM, SLA)

Nano and microfabrication (Photolithography)

Dry etching (Deep RIE, Metal, Dielectric RIE)

Wet etching (Metal assisted chemical etching)

Powder X-Ray Diffractometter

UV-VIS spectroscopy

Fourier-transform Infrared Spectroscopy

Langmuir-Blodgett Trough

E-beam, sputter, PLD

PECVD, APCVD

FDTD simulation (COMSOL Multiphysics

[AC/DC, Semiconductor, Piezoelectric modules])

Peer reviewed publication

First-authored papers

1. J. Kim†, **S. B. Kang† (equal contribution)**, H. Yu†, J. Kim., J. Ryu, J. Lee, C. Yi., K. J. Choi, C. Kim "Augmented Absorption Channels Induced by Wave-Chaos in Freestanding Nanowire Arrays" Under review in *Advanced Materials* (IF = 25.80)

2. **S. B. Kang**, J. Kim, M. H. Jeong, A. Sanger, C. U. Kim, C. Kim and K.J. Choi "Stretchable and colorless free-standing microwire arrays for transparent solar cells with flexibility" *Light: science and applications*, 8, 121 (2019) (Nature Publishing Group, IF = 14.098)

3. **S. B. Kang**, M. H. Jeong, I. Y. Choi, S.-D. Sohn, S. H. Kim, H.-J. Shin, W. I. Park, J. C. Shin, M. H. Song, K. J. Choi, "Self-Assembled, Highly Crystalline Porous Ferroelectric Poly (Vinylidene Fluoride-co-Trifluoroethylene) interlayer for Si/Organic Hybrid Solar Cells," *Nano Energy* 41, 243-250 (2017) (IF = 15.548)

4. A. Sanger†, **S. B. Kang† (equal contribution),** M. H. Jeong, M. J. Im, I. Y. Choi, C. U. Kim, H.M. Lee, K. J. Choi "Morphology-controlled aluminum-doped zinc oxide nanofibers for highly sensitive NO_2 sensor with full recovery at room temperature" *Advanced Science*, 1800816 (2018) (IF = 15.804)

5. **S. B. Kang**[†]**,** K.C Kwon[†], K.S Choi, R. Lee, A. Sanger, S.Y Kim, H.W. Jang, K.J. Choi, "Transfer of ultrathin molybdenum disulfide and transparent nanomesh electrode onto silicon for efficient heterojunction solar cells" *Nano Energy*, 50, 649-658 (2018) (IF = 15.548)

6. **S. B. Kang**, S. H. Won, M. J. Im, C. U. Kim, W. I. Park, J. M. Baik, K. J. Choi, "Enhanced piezoresponse of highly aligned electrospun poly (vinylidene fluoride) nanofibers," *Nanotechnology* 28, 395402 (2017) (IF = 3.399)

7. A. Sanger[†]**, S. B. Kang**[†] **(equal contribution)** M. H. Jeong, C. U. Kim, and K. J. Choi "All-transparent NO_2 gas sensor based on free-standing Al doped ZnO nanofibers" *ACS applied electronic materials*, 17, 1261-1268 (2019) (IF = pending)

Submitted or To be Submitted

8. **S. B. Kang**, M. H. Jeong, W. J. Park, S. Kang, A. Sanger, C. Yang and K.J. Choi "An ambipolar Poly(Vinylidene Fluoride-co-Trifluoroethylene) passivated back surface field layer for high efficient organic / Si hybrid solar cells" Submitted to *Energy & Environmental Science*

9. A. Sanger[†]**, S. B. Kang**[†] **(equal contribution),** C. U. Kim, M. H. Jeong, J. Baik, and K. J. Choi "Heterogeneous reduced graphene oxide - zinc oxide nanorods as highly sensitive sensing platform" submitted to *Advanced Functional Materials*

10. **S. B. Kang**[†], W. J. Park[†], M. H. Jeong, and K.J. Choi "Highly transparent Si solar cells with surface modification" In preparation

Co-authored papers

1. M. H. Jeong, **S. B. Kang**, J. S. Son, S. Baek, J. Kim and K.J. Choi "Optimizing temperature gradient in wearable solar thermoelectric generators", *Journal of power source, under review* (IF = 7.467)

2. V. V. Sharma, K. N. Kim, G. H. Han, E. Gwak, J. Woo, **S. B. Kang**, K.J.Choi, J. Kim, and J.M. Baik "Multiscale Pores with Vertical Porosity Gradient for Simultaneous Pressure and Bending Detection with Enhanced Linear Sensitivity" *Advanced Material Technologies, accepted* (IF = 5.456)

3. M. H. Jeong, A. Sanger, **S. B. Kang,** Y. S. Jung, I. Oh, J.W. Yoo, G.H. Kim, K. J. Choi "Increasing thermoelectric power factor of solvent-treated PEDOT : PSS thin films on

PDMS by stretching" *Journal of Materials chemistry A*, 6, 15621-15629 (2018) (IF = 10.733)

4. M. G. Lee, C. W. Moon, H. Park, W. Sohn, **S. B. Kang**, S. Lee, K. J. Choi, H. W. Jang, "Dominance of Plasmonic Resonant Energy Transfer over Direct Electron Transfer in Substantially Enhanced Water Oxidation Activity of BiVO4 by Shape-Controlled Au Nanoparticles," *Small* 13, 1701644 (2017) (IF = 10.856)

5. J. Hwang, D. Patil, **S. B. Kang**, K. J. Choi, J. C. Shin, "Polyacrylic Acid / Polypyrrole / Silver Nanowires Nanocomposite Electrode for Electrochemical Supercapacitor," *Journal of Nanoscience and Nanotechnology* 17, 8138-8143 (2017) (IF = 1.093)

6. Y. S. Jung, D. H. Jeong, **S. B. Kang**, F. Kim, M. H. Jeong, K.-S. Lee, J. M. Baik, J.-S. Kim, K. J. Choi, "Wearable solar thermoelectric generator driven by unprecedentedly high temperature difference," *Nano Energy* 40, 663-672 (2017) (IF = 15.548)

7. M. J. Park, C. U. Kim, **S. B. Kang**, S. H. Won, J. S. Kwak, C.-M. Kim, K. J. Choi, " 3D Hierarchical Indium Tin Oxide Nanotrees for Enhancement of Light Extraction in GaN-Based Light Emitting Diodes," *Advanced Optical Materials* 5, 1600684 (2017) (IF = 7.125)

8. J. Kwon, M. J. Im, C. U. Kim, S. H. Won, **S. B. Kang**, S. H. Kang, I. T. Choi, H. K. Kim, I. H. Kim, J. H. Park, K. J. Choi, "Two-terminal DSSC/silicon tandem solar cells exceeding 18% efficiency," *Energy & Environmental Science* 9, 3657-3665 (2016) (IF = 33.250)

Patents (Domestic) [Registered:13, Pending:7]

Registered

1. K.J Choi, **S.B. Kang** "Electrospinning apparatus" (KR 10-1676332)
2. K.J Choi, M. J. Park, S.H Won **S.B. Kang** "Photovoltaic devices with nanostructure embedded antireflection film" (KR 10-1672648)
3. K.J Choi, M. J. Park, **S.B. Kang** "Nozzle design for 3D printer" (KR 10-1752061)
4. K.J Choi, M. J. Park, **S.B. Kang** "Manufacturing Method of Polymer Solar Cell Embedded with Silicon Nanowire" (KR 10-1703443)
5. K.J Choi, M. J. Park, **S.B. Kang**, "Solar Cells Using Self-Assembled Nanostructured Oxide and Its Manufacturing Method" (KR 10-1783125)
6. S.I Seok, K.J Choi, J.H Noh, B.W. Park, S.H Lee, **S. B. Kang** "A thermoelectric module including a perovskite thermoelectric material, a thermoelectric element including the thermoelectric element, and a thermoelectric element" (KR 10-1838794)
7. K.J Choi, **S.B. Kang**, M. J. Park "Manufacturing method of micro structure for water

treatment membrane through Si templet formed by photolithography" (KR 10-1846644)

8. K.J Choi, **S.B. Kang,** M.J. Im "Porous ferroelectric organic thin film formation method" (KR 10-1864494)

9. K.J Choi, **S.B. Kang,** M.J. Im "Manufacture of Transparent Electrode by Heat and UV Treatment" (KR 10-1955104)

10. K.J Choi, **S.B. Kang,** " Applied (-) voltages to manufacture large-area transparent electrodes" (KR 10-1973859)

11. K.J Choi, **S.B. Kang,** Y.S Jung, K.S Lee "Improvement of wearable thermoelectric device through self-heating film based on light absorber" (KR 10-1976930)

12. K.J Choi, **S.B. Kang,** "Photovoltaic device using porous organic ferroelectric thin film" (KR 10-1998467)

13. K.J Choi, **S.B. Kang,** M.J Im "Silicon Micro Wire / Composite Manufacturing Method for Colorless Transparent Flexible Solar Cells" (KR 10-2025471)

Pending

14. K.J Choi, **S.B. Kang,** Y.S Jung "Nozzle design for 3D printer" (KR 10-2016-0124061)

15. K.J Choi, **S.B. Kang,** A. Sanger, "Room temperature operable gas sensor using hollow nanofibers and its fabrication methods" (KR 10-2018-0101267)

16. K.J Choi, **S.B. Kang** A. Sanger, "Fabrication of free-standing nanofibers and its application for transparent gas sensor" (KR 10-2018-0101266)

17. K.J Choi, **S.B. Kang** "Chalcogenide compound- based solar absorber and manufacturing method there of it" (KR 10-2019-0075197)

18. K.J Choi, **S.B. Kang** "Organic ferroelectric thin film for silicon device passivation" (KR 10-2019-0113128)

19. K.J Choi, **S.B. Kang**, W.J. Park "Silicon-Based Transparent Solar Cell Containing Pores and Method of Manufacturing Same" (KR 10-2019-0113931)

20. K.J Choi, **S.B. Kang** A. Sanger, "Gas sensor comprising reduced oxidized graphene layer and method of making same" (KR 10-2019-0150378)

Patents (International)

1. K.J Choi, **S.B. Kang**, "Silicon Micro Wire / Composite Manufacturing Method for Colorless Transparent Flexible Solar Cells" (CN201810437900.0)

2. K.J Choi, **S.B. Kang,** "Manufacture of Transparent Electrode by Heat and UV Treatment" (CN201810369624.9)

Conference

International

1. **S. B. Kang** and M.H Song, K. J Choi, MRS spring meeting, 2015, SF, USA (Poster)
2. **S. B. Kang** and K. J Choi, MRS spring meeting 2016, AZ, USA (Poster)
3. **S. B. Kang** and K. J Choi, Nano Korea 2016, Kintex, Korea (Oral)
4. **S. B. Kang** and K. J Choi, PVSEC 2016, Singapore (Oral)
5. **S. B. Kang** and K. J Choi, MRS spring meeting, 2017 spring, AZ, USA (Poster)
6. **S. B. Kang** and K. J Choi, MRS spring meeting, 2018 spring, AZ, USA (Oral)
7. **S.B Kang** and K. J Choi, 5th International Conference on Electronic Materials and Nanotechnology for Green Environment, 2018, Korea (Oral)
8. **S. B. Kang** and K. J Choi, MRS spring meeting, 2019 spring, AZ, USA (Poster)
9. **S. B. Kang** and K. J Choi, MRS Fall meeting, 2019 fall, MA, USA (Oral)

Domestic

1. **S. B. Kang** and, K. J Choi, Korea society of optoelectonics, 2014, Korea (poster)
2. **S. B. Kang** and K. J Choi, The Korea Institute of Electrical and Electronic materials engineers annual summer conference, 2015, Korea (Oral)
3. **S. B. Kang** and K. J Choi, The Korea vacumm society, 2015, Korea (poster)
4. **S. B. Kang** and K. J Choi, The Korea Institute of Electrical and Electronic materials engineers annual summer conference, 2016, Korea (Oral)
5. **S.B. Kang** and K. J Choi, The Korea Institute of Electrical and Electronic materials engineers annual summer conference, 2017, Korea (Oral)
6. J.B Kim**, S.B Kang** and K. J Choi, The Korea Institute of Electrical and Electronic materials engineers annual summer conference, 2017, Korea (Poster)
7. **S.B Kang** and K. J Choi, The Korea system of materials, 2018, Korea (Oral)